Damage Evolution of High Chromium Steels Utilised for High Temperature Components

Schädigungsentwicklung chromhaltiger Stähle mit Einsatz in Hochtemperaturkomponenten
Master-Thesis von Muhammad Mohsin Khan aus Badin
Tag der Einreichung:

1. Gutachten: Prof. Dr.-Ing. Matthias Oechsner
2. Gutachten: Prof. Dr. rer. nat. Robert Stark

TECHNISCHE
UNIVERSITÄT
DARMSTADT

Institute for Materials Technology (IfW)
Institute of Materials Science

Damage Evolution of High Chromium Steels Utilised for High Temperature Components
Schädigungsentwicklung chromhaltiger Stähle mit Einsatz in Hochtemperaturkomponenten

Vorgelegte Master-Thesis von Muhammad Mohsin Khan aus Badin

1. Gutachten: Prof. Dr.-Ing. Matthias Oechsner
2. Gutachten: Prof. Dr. rer. nat. Robert Stark

Tag der Einreichung:

Bitte zitieren Sie dieses Dokument als:
URN: urn:nbn:de:tuda-tuprints-73790
URL: http://tuprints.ulb.tu-darmstadt.de/7379

Erklärung zur Master-Thesis

Hiermit versichere ich, die vorliegende Master-Thesis ohne Hilfe Dritter nur mit den angegebenen Quellen und Hilfsmitteln angefertigt zu haben. Alle Stellen, die aus Quellen entnommen wurden, sind als solche kenntlich gemacht. Diese Arbeit hat in gleicher oder ähnlicher Form noch keiner Prüfungsbehörde vorgelegen.

Darmstadt, den August 1, 2018

(Muhammad Mohsin Khan)

Abstract

Several cumulative methods were developed to define and evaluate fatigue and creep damage with dependence on state variables. A phenomenological damage definition is selected under the scope of continuum damage mechanics, which fulfills various requirements of independency of critical damage on state variables.

In this thesis, experimental data of strain-controlled LCF experiments performed with and without hold-time on high-chromium steels were received. A method to determine the true and critical damage is shown, where the critical damage is independent of the temperature and the strain range. Also, damage threshold based on accumulated plastic strain is determined showing explicit dependence on strain range. Moreover, the material parameter of the damage evolution equation is calculated by minimizing the equation using function minimizing algorithms, where it is approximately same for experiments without and with hold-time at the same temperature. Multiaxial fatigue damage model (Sermage et al., 2001) is employed to compute damage showing reasonable results with an error as high as 9.17%. Furthermore, lifetime prediction is performed using constants from experiments without hold-time for experiments with hold-time showing acceptable results with an error as high as 16.66%. Also, the error for prediction of experiment with a service-type cycle is 15.9%.

Acknowledgement

First of all, I would like to thank Felix Kölzow for supervising my thesis and being there always when I needed him. Due to his excellent insights and help throughout the thesis, I was able to cope-up with the work efficiently.

Secondly, I would also like to express my gratitude to Prof. Dr.-Ing. Matthias Oechsner for approving and allowing me to pursue my thesis in the Institute of Materials Technology (MPA/IfW). Also, due to this institute, I was able to receive such valuable data to be utilised in the research. Besides, thanks to Prof. Dr. rer. nat. Robert Stark for refreeing my thesis.

Thirdly, special thanks to Dirk Jobski and Sascha Lamm for collaborating with me on CT results and providing me with the Gray-analysis results for my samples. Besides, thanks to Miro Lander for arranging the appointments for VGSTUDIO MAX analysis and visualisation software and also for helping.

Also, many thanks to Gohar Ali Siddiqui for his time for proofreading my thesis. I would also like to convey my thanks to all my friends who supported me throughout the thesis period. Special mentions to Syed Muhammad Ali, Taha Tariq and Muhammad Sajjad Akbar for their help.

Finally, I would like to thank my parents and my siblings for their continuous support right from the beginning till today. Without my parents' all kinds of support, it would not have been possible for me to be where I am today.

Table of Contents

List of Figures

List of Tables

List of Symbols

α	Internal parameter of change in material, Associated variable of kinematic hardening
$\tilde{\alpha}$	Effective associated variable of kinematic hardening
A	Kinematic hardening variable
γ	Accumulative hardening paramter
$\mathbb{C}_o$	Elastic modulus tensor of the undamaged material
$\mathbb{C}(\mathscr{D})$	Elastic modulus tensor of the damaged material
C_{ijkl}	Coordinate of elastic modulus tensor
δ_{ij}	Kronecker delta, $\delta_{ij} = 1$, when i = j and $\delta_{ij} = 0$, when i $\neq$ j
D	Scalar damage variable
$\mathbf{D}$	Second-order damage tensor
$\mathbb{D}$	Fourth-order damage tensor
$\mathscr{D}$	Even-order damage tensor
D_{ij}	Coordinate of second-order damage tensor
D_{ijkl}	Coordinate of fourth-order damage tensor
D_{comp}	Computed damage
D_{crit}	Critical damage
D_C	Creep damage variable
D_F	Fatigue damage variable
ε	Strain
$\tilde{\varepsilon}$	Effective strain
ε_{kl}	Coordinate of strain tensor
ε^e	Elastic strain
ε^p	Plastic strain
$\Delta\varepsilon$	Strain range
E	Young's modulus
$\tilde{E}$	Effective young's modulus
$\delta\mathrm{F}$	Tensile load
G	Shear modulus
$\tilde{G}$	Effective shear modulus
H	Hardness
$\tilde{H}$	Effective hardness
I	Intensity of electrical resistance
$\tilde{I}$	Effective intensity of electrical resistance
I_{ijkl}	Coordinate of fourth-order identity tensor
$\mathbb{M}(\mathscr{D})$	Damage effect tensor
$\vec{n}$	Unit normal vector
$\tilde{\vec{n}}$	Modified unit normal vector
n_i	Coordinate of the unit normal vector
$\tilde{n}_i$	Coordinate of transformed unit normal vector
ν	Poisson's ratio
$\tilde{\nu}$	Effective poisson's ratio
$N_{A5\%}$	Number of cycles to crack initiation at 5% load-drop
$N_{A10\%}$	Number of cycles to crack initiation at 10% load-drop
N_R	Number of cycles to failure

N_{FI}	Number of cycles to fatigue crack initiation
N_{CI}	Number of cycles to creep void nucleation
ρ	Density
$\tilde{\rho}$	Effective density
p	Accumulated plastic strain
p_D	Damage threshold
q	Heat supplied to the system
r	Associated variabe of isotropic hardening
$\tilde{r}$	Effective assoaciated variable of isotropic hardening
R	Isotropic hardening variable, Resistivity
$\tilde{R}$	Effective isotropic hardening variable, Effective resistivity
R_v	Stress triaxiality function
σ	Cauchy stress
σ_{EQ}	Equivalent stress
σ_H	Hydrostatic stress
σ_s	Plastic yield stress
σ_U	Ultimate stress
σ_V	Viscouse stress
σ_Y	Yield stress
$\tilde{\sigma}$	Effective stress
$\tilde{\sigma}_{ij}$	Coordinate of effective stress
s	Entropy
$\delta \mathrm{S}$	Area of a volume element
$\delta \tilde{\mathrm{S}}$	Effective area
$\delta \mathrm{S}_D$	Reduced area of a volume element due to voids
$\mathbb{S}_o$	Compliance tensor of the undamaged material
$\mathbb{S}(\mathscr{D})$	Compliance tensor of the damaged material
Φ	Dissipation per unit volume
t	Time
t_{HZ}	Hold-time in tension
t_{HD}	Hold-time in compression
T	Temperature
T_m	Melting temperature
v	Wave speed
$\tilde{v}$	Wave speed inside damaged material
$\vec{v}$	Reference vector
v_i	Coordinate of the reference vector
V	Potential difference
$\tilde{V}$	Effective potential difference
W^E	Elastic strain energy per unit volume
W_s	Stored energy
Ψ	Damage variable, Helmholtz free energy
Y	Damage strain energy release rate

1 Introduction

Engineering materials employed in service are exposed to adverse conditions through mechanical loading, chemical action, hot and cold temperature working processes or sometimes a combination of these. During such operations, the working state of the engineering components gets worse by the induction of microscopic defects such as cracks and voids in the material. These microcracks and microvoids coalesce with the progressive process at which the components are being serviced, contributing to the degradation of mechanical properties or damage. With increasing damage, several mechanical properties of the components are deteriorated such as strength, toughness, rigidity, and the life of the component. The research on the behavior of engineering materials due to microscopic flaws is of particular interest to mechanists and as well as material scientists.

High-temperature processes are a norm for the aerospace, steam turbine, and power generation industries. Several types of high chromium steels are utilized as the component material in these industries. These processes are being conducted at severe conditions of cyclic loading and varying temperatures, producing mechanical and thermal stresses, which induces creep damage as well as fatigue damage (also called creep-fatigue interaction) in the components. For the improvement of process efficiency, the working temperatures and pressures must be increased resulting in the components being required to bear more acute conditions, which poses enhanced damage and an early lifetime end. The creep damage has a detrimental effect on fatigue, which enhances it. Therefore, the creep-fatigue interaction mechanism of failure is of primary importance for high-temperature components [1, 2]. The damage process is unavoidable during the service, and therefore, the requirement of damage evolution laws for the quantitative and qualitative evaluation is necessary. Besides, lifetime prediction assessment for the components is also indispensable to avoid massive losses in the form of premature failures. Accurate damage evolution concerning the number of cycles and the critical damage value at crack initiation is of fundamental importance in proposing the lifetime of a component.

In the past, various damage accumulation models have been proposed by the researchers since early 1970s for the accumulation of creep damage. Some of these include time-fraction model, ductility exhaustion model, modified ductility exhaustion model, strain-energy ductility exhaustion model, etc [3–6]. For fatigue damage, Miner's rule [7] is the renowned cumulative fatigue damage model which is the reciprocal of the fatigue life. Several researchers have used these models for the damage assessment and the life-prediction of steels and alloys utilized as high-temperature components. Although these models are widely used, they largely depend on the experimental parameters such as temperature, strain range, stress and the time to failure. Even though the strain-energy exhaustion model shows relatively less dependence on these parameters than the other models, there exists a healthy amount of deviation from the statistical results. For instance, Takahashi et al. [6] studied the data of several materials with tensile-hold creep-fatigue tests, with strain control having a fixed hold time at maximum strain for each cycle and evaluated the results by using different damage accumulation models. Fig. 1 depicts the accumulated total damage versus the strain range, where explicit dependence of the total damage on the strain range can be observed.

The main motivation behind this thesis is to find and implement a damage model (damage variable) which has a physical meaning and is able to predict lifetime of the components. The critical damage should be independent of the state variables, such as, stress, strain, and temperature. Furthermore, it should be able to suggest the same threshold value for different stress triaxialities. It is sought to achieve this objective by using CDM approach.

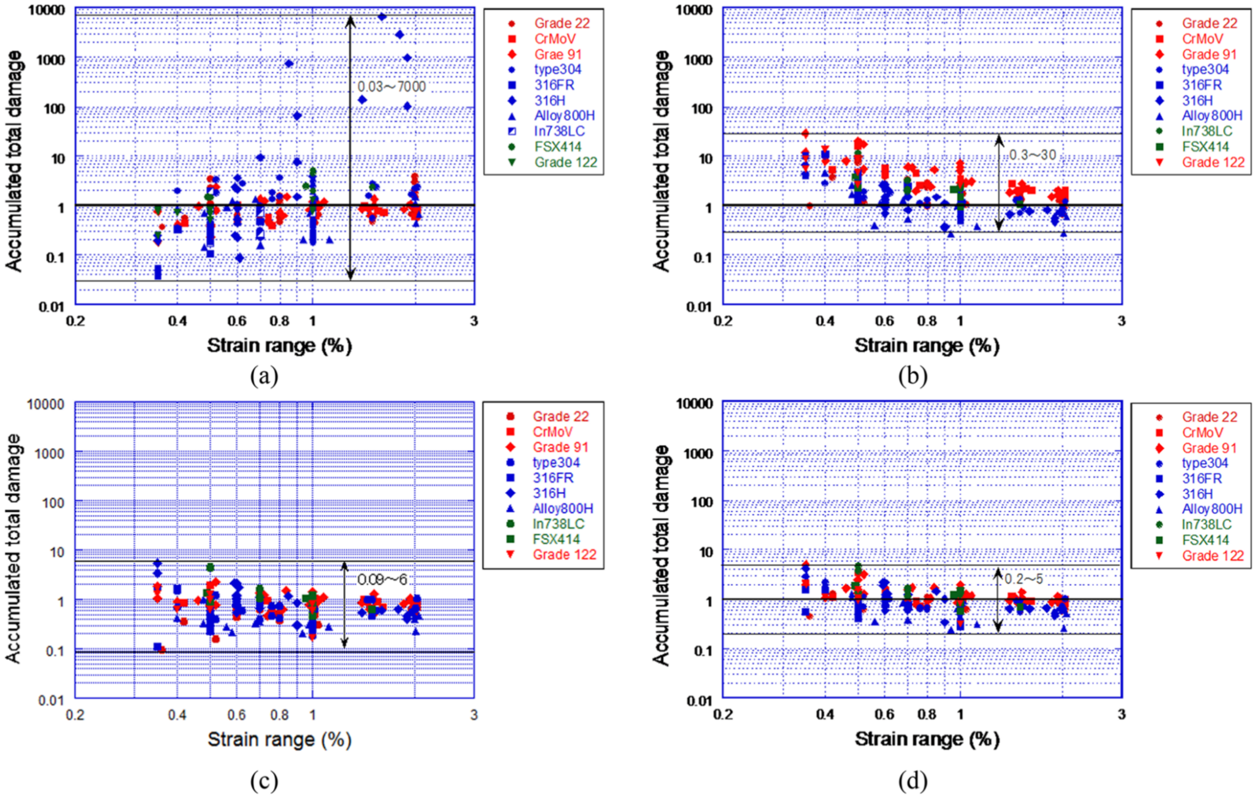

(a)

(b)

(c)

(d)

Figure 1: Dependency of total damage on strain range. - by utilizing (a) Time fraction model, (b) Ductility exhaustion model, (c) Modified ductility exhaustion model, and (d) Energy-based model [6].

CDM or Damage Mechanics, is nowadays widely used to investigate and analyze damage. It is based on continuum mechanics and is a phenomenological theory for damage assessment and failure processes of a material. This theory was developed in the early 1980s by several researchers [8–12] in an attempt to have a physical and phenomenological definition of damage, that does not depend on the state variables (parameters). Constitutive and damage evolution equations have been presented till date by the researchers under the umbrella of CDM, which are beneficial for damage assessment and lifetime predictions. Furthermore, this theory also offers the idea of critical damage value or damage threshold at which a visible crack initiates. Moreover, the damage variable is independent of the state variables, through which damage can be proved as material property.

In this thesis, experimental data of strain-controlled Low-Cycle Fatigue (LCF) experiments, with and without tension and compression-hold times at maximum strain levels performed on high chromium steels at the Institute of Materials Technology (MPA / IfW), Department of Mechanical Engineering, Darmstadt University of Technology, were received. Moreover, damage evolution and assessment has been carried out using the multiaxial fatigue damage evolution and constitutive equations as proposed by Sermage et al. [13]. Also, critical damage value for micro-crack initiation has been determined. Furthermore, material parameter of the damage evolution equation has been minimized by using the Nelder-Mead [14] and the BFGS algorithm [15] and lifetime prediction analysis has been performed. In addition, computed tomography (CT) is also performed after LCF-experiment to measure the volume of the defects.

2 Theoretical Background

2.1 Selection of Damage Definition

Damage is a phenomenon long studied under various assumptions and notions. Cumulative damage models [2–7] have been used to date, but their drawback lies in the fact that they rely on the cumulation of either time to rupture or fracture strain, thereby showing direct dependence for damage.

In this thesis, it is sought to utilize a damage definition that has the following properties:

1. The damage is a material property.
2. The critical damage must be strain independent.
3. The critical damage must be temperature independent.
4. The damage model must define a threshold value which is independent of the stress-triaxiality.
5. The damage must be quantifiable, where it can be calculated directly from the experiment.

Above listed criteria suggests that the definition should be phenomenological in approach. A comprehensive survey of fatigue damage models [16] lists most of the famous techniques to measure damage. CDM looks promising enough to fulfill the above criteria. Thus, it is discussed and utilized further in the report to evaluate the damage.

2.2 Damage Definition

Damage is a continuous physical phenomenon that is accompanied by deterioration or impairment of a component or its usefulness. In CDM, it is studied as the difference between the virgin and the damaged material and its mechanisms are studied through damage variables (mechanical variables). According to Murakami [8], Krajcinovic [9], and Lemaitre [12], the damage is the progressive process of creation and growth of the microvoids or microcracks in the microscopic, mesoscopic and macroscopic scale and the failure through the deterioration of mechanical properties. At the microscopic scale, the damage process can be understood as the creation and growth of microcracks and microvoids due to the breakage of bonds. At the mesoscopic scale, it is primarily the initiation of a visible crack due to the coalescence of the microvoids. At the macroscopic scale, it can be seen as the development of the initiated macrocrack. CDM is utilized for the damage assessment at the microscopic and mesoscopic level and therefore, relies mainly on continuum mechanics.

2.3 Mechanisms of Damage

Damage in its definition is quite general. Although, macroscopically, damage can be understood as the simple failure of an engineering material due to microstructural defects. It has different mechanisms when the damaged materials are investigated at the microscopic scale. In principle, it is the atomic debonding which can be initiated due to the following different mechanisms as shown in Fig. 2.

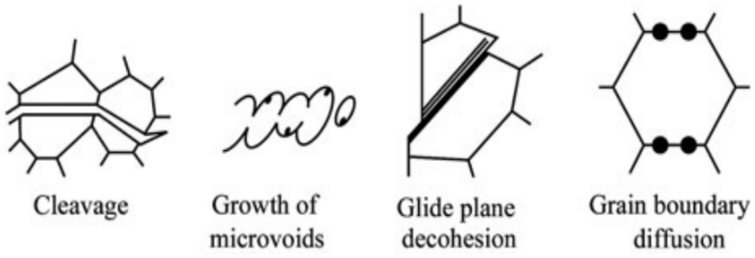

Figure 2: Mechanisms of damage at the microscopic scale [1].

2.3.1 Cleavage

Cleavage is a mechanism of damage that occurs due to the tensile decohesion of atoms on the crystallographic planes that are inherent to the crystal. This phenomenon primarily occurs in poly-crystalline materials such as inorganic materials of body-centered cubic (BCC) metals. The characteristic of cleavage is that it occurs by direct separation of the lattice planes due to the breaking of atomic bonds. Cleavage is accompanied by elastic deformation and no or little plastic deformation. The fracture associated with this type of damage is called Cleavage fracture. It desirably takes place at the lattice planes where the atomic binding or cohesive energy is the weakest and induces at the point where the stress concentration is high due to defects in the material. For instance, it could occur at the grain boundaries due to the stress concentration because of the dislocation pile-up.

2.3.2 Growth of Microvoids

During the deformation of a ductile material, for instance, tensile loading of a ductile material as shown in Fig. 3, large plastic deformation is observed. Due to the deformation, separation of the inclusion-matrix interface occurs, contributing to the creation of microvoids. As the deformation progresses, these microvoids coalesce and grow. Dislocation pile-up against the inclusions is the leading cause that this decohesion between inclusion-matrix interface occur. The fracture associated with this type of damage is called Dimple fracture because dimples or dents are formed on the surface due to microvoid growth and coalescence when observed through a microscope.

2.3.3 Glide Plane Decohesion

Glide plane decohesion is the fracture of poly-crystalline materials along specific slip planes due to the creation of new surfaces, which happens due to the significant plastic deformation. This type of damage mechanism usually occurs during fatigue and is responsible for fatigue failure. Materials that are highly pure and have very less number of defects such as inclusions are deformed to a great extent because there are fewer means of void formation and dislocation glide is carried out in slip planes. Due to extensive deformations, the cross-sectional area of the material lowers to nearly zero. Therefore, such type of fracture is called point-type or chisel-edge fracture [1].

2.3.4 Grain Boundary Diffusion

In poly-crystalline metals, the role of temperature is evident on the microstructural properties of the material. It is usually seen at temperatures higher than 1/3 of the melting point T_m of the

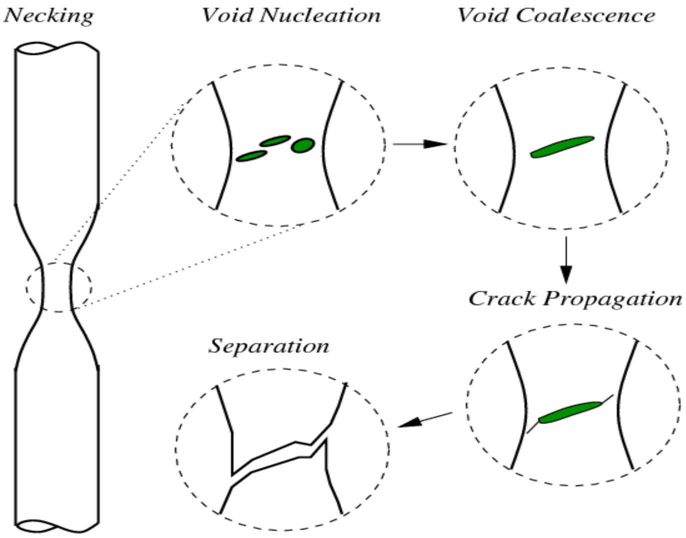

Figure 3: Schematic representation of the creation and growth of microvoids during the deformation of a ductile material [17].

material. When such metals are subjected to static loads for a long time at high temperature, the diffusion of defects such as vacancies gives rise to the formation of voids on grain boundaries. This grain boundary diffusion is much faster than the bulk diffusion because the defect concentration is small in bulk in comparison to the grain boundary. The growth of these cavities on grain boundaries causes microscopic decohesion.

2.4 Damage Types

In the previous section (Sec. 2.3), we have familiarized ourselves with the mechanisms of damage that occur at the microscale, which is essentially the tensile or shear decohesion or in simple words the separation of atomic bonds. Although the microscopic phenomenon is the same, the damage can have different characteristics at the mesoscale depending upon the type of material, type of load and the temperature. The damage may be categorized as follows [1, 18]:

2.4.1 Brittle Damage

Brittle damage is a type of damage in which no apparent plastic deformation takes place. Growth and coalescence of microvoids are accomplished not only at the micro scale but also at the mesoscale, and a crack is initiated, which means that the debonding forces are less than the slip-strength but are higher than the cohesive or binding strength of the material. Brittle damage usually occurs in ceramics, concretes, rocks, and composites. Fig. 4 shows an SEM fractograph of brittle cleavage fracture in tempered martensitic chrome alloy steel.

2.4.2 Ductile Damage

On the contrary, if the development and coalescence of microvoids occur due to significant plastic deformation then the type of damage is called ductile. In poly-crystalline metals, ductile damage results due to the fracture of inclusions or due to the separation of the inclusion-matrix interface, which form cavities/voids. These voids then grow and coalesce and form a dimples or dents which is often observable on the fracture surface. Ductile metals, especially those

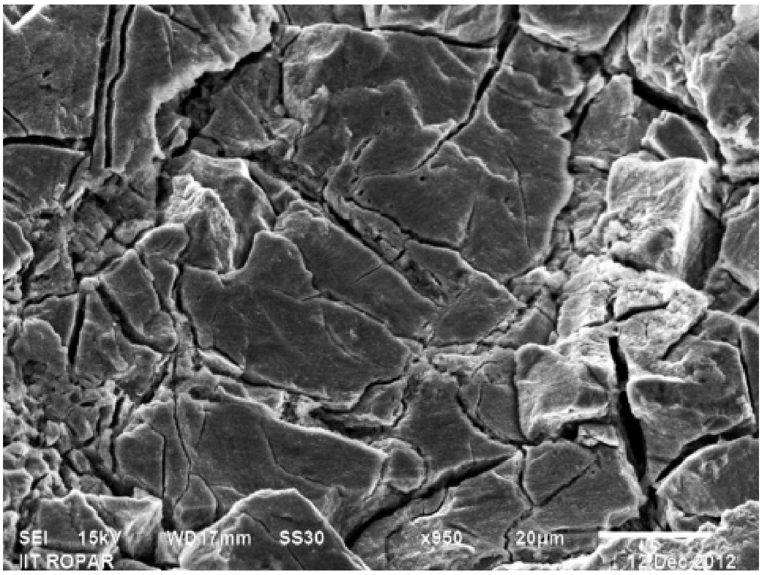

Figure 4: SEM fractograph of tempered martensitic steel showing brittle cleavage fracture [19].

having high purity, show substantial deformation with an elongation to failure of atleast 5% or a reduction in area to failure of atleast 20% under suitable conditions [20]. Fig. 5 shows an SEM fractograph of a ductile fracture surface in transformation toughened Nichrome alloy.

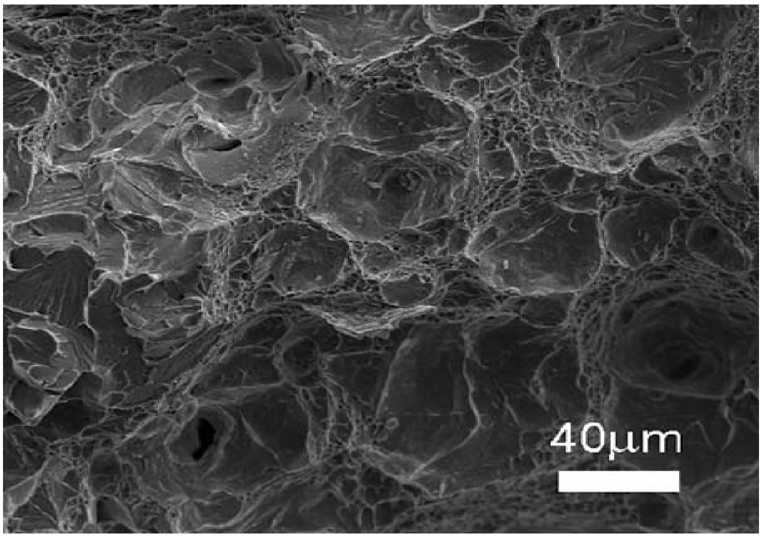

Figure 5: SEM fractograph of a ductile fracture surface in transformation toughened Nichrome alloy [21].

2.4.3 Creep Damage

When poly-crystalline metals are subjected to high temperatures (more than 1/3 of their absolute melting temperature T_m) at static load for a long time, plastic deformation involves viscosity. Due to the diffusion of vacancies on grain boundary, intergranular decohesion takes place. These vacancies create and grow on grain boundaries due to the application of constant stress for an extended span of time and eventually lead to macroscopic crack formation. It usually occurs at stresses well below the yield strength. This type of damage is known as Creep damage. Due to time-dependency, this type of damage is called visco-plastic damage. Fig. 6 shows grain boundary cavitation due to creep damage in copper.

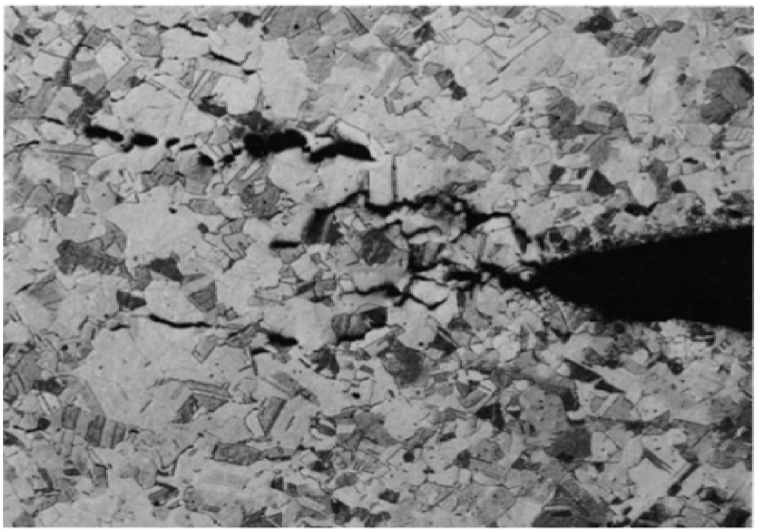

Figure 6: Creep damage in copper at 250°C [1].

2.4.4 Low Cycle Fatigue Damage

Fatigue damage causes when the material is subjected to cyclic loading, the irreversible plastic damage accumulates over time generating microvoids. These voids grow to form cracks and give rise to rupture of the material. Microscopically, this form of damage is localized than creep and ductile damage.

In metals, fatigue damage is caused by the deformation along the slip planes inducing glide plane decohesion which leads to initiation of cracks. When the applied load or stress is very high, it induces transgranular slip in material, causing it to fracture in a relatively small number of cycles. If the number of cycles to fatigue failure N_R is less than 10000 ($< 10^4$), then it is usually called low cycle fatigue (LCF). Fig. 7 shows an example of low cycle fatigue of Inconel 718.
In the same category, if the number of cycles to fatigue failure N_R is less than 100 ($< 10^2$), then the type of damage is called very low cycle fatigue. For such type of damage, the stresses are very high in order to initiate the damage at very less number of cycles. Normal damage evolution and fatigue life prediction rules for usual LCF are not applicable for very low cycle fatigue and predicted values of damage are often high [22].

2.4.5 High Cycle Fatigue Damage

If the cyclic stresses are extremely low in magnitude, the transgranular slip occurs in fewer numbers of planes on the material surface due to which plastic deformation is small at the mesoscale. Furthermore, the accumulated damage per cycles is small so that cycles to fracture rises. The number of cycles to failure N_R may be very large ($> 10^5$). This type of damage is called high cycle fatigue.

It was assumed that fatigue failure would never occur in iron and steels for loads up to a particular value at which the material can bear an unlimited number of cycles and the corresponding

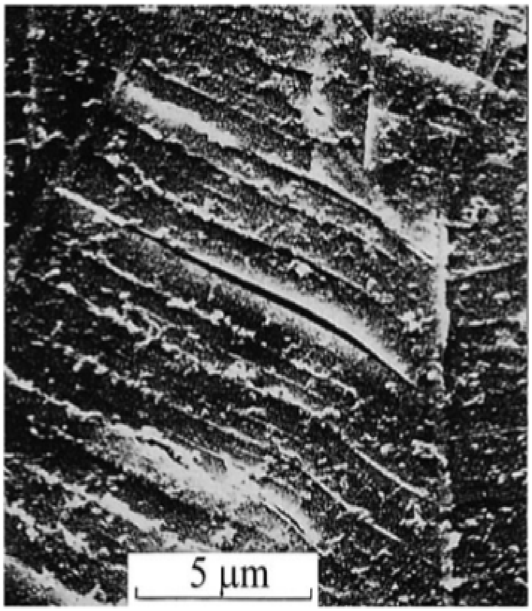

Figure 7: Low cycle fatigue due to glide plane decohesion in Inconel 718 [1].

magnitude of the load has been defined as fatigue limit. However, in recent times, it has been showed that even for loads less than the fatigue limit, fatigue crack could initiate in the materials if the number of cycles to failure N_R exceeds 10^8 through 10^{10}. Such type of damage is called very high cycle fatigue or ultrahigh cycle fatigue.

2.4.6 Creep-Fatigue Damage

When cyclic loading with dwell times at high temperature is applied to poly-crystalline metals, creep as well as fatigue damage develops in the material simultaneously. Creep damage, as discussed, accumulates at the intergranular sites through grain boundary diffusion whereas fatigue damage accumulates at the surface through transgranular slip. Due to different mechanisms at the mesoscale, both types of damage develop separately without interacting with each other in early cycles. However, at later stages of the lifetime, there builds an influence of both types of damage on each other, resulting in accelerated overall damage. This type of damage is called creep-fatigue interaction or creep-fatigue damage. As fatigue damage is much more localized than the creep damage, the effect of fatigue on creep is less compared to the effect of creep on fatigue. Creep-fatigue damage is an essential damage mechanism that is frequently encountered in high-temperature components and hampers their performance. Fig. 8 shows a schematic illustration of different modes of damage in creep-fatigue interaction.
Here N_R, N_{FI} and N_{CI} denote the number of cycles to creep-fatigue failure, number of cycles to fatigue crack initiation and number of cycles to creep void nucleation, respectively. As shown, interaction occurs when creep voids are nucleated earlier than fatigue crack initiation. Though the interaction is negligible at the beginning, it increases with time.

2.5 Mechanical Representation of Damage

To describe the damage variable, few concepts are needed to be understood. In the view of CDM, the damage variables are first defined and then damage evolution is discussed by the use of these damage variables.

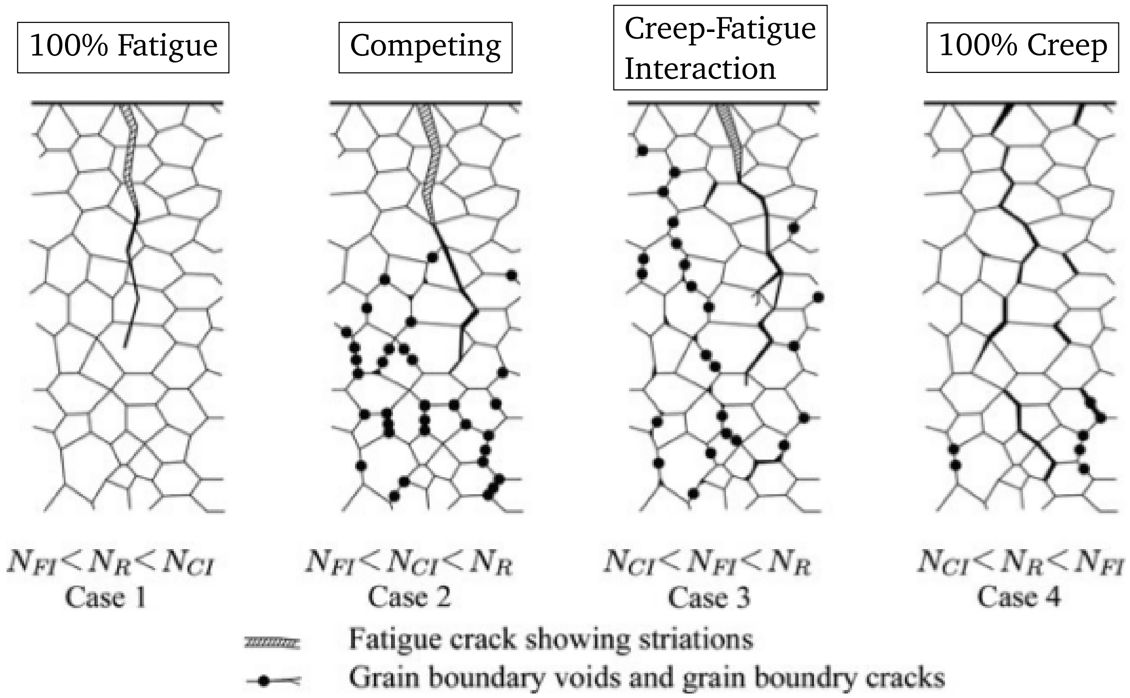

Figure 8: Schematic representation of different modes of damage in creep-fatigue interaction [1].

2.5.1 Representative Volume Element

In Continuum Mechanics, the Representative Volume Element (RVE) is a concept used to illustrate the effect of different microscopic discontinuities on the smallest volume of an element that represents the value of the whole element. Therefore, mechanical effects of the microstructure must be homogenized and represented as a continuous macroscopic field in the material. In case of periodic elements, the unit cell can be chosen merely as the RVE, but for non-periodic elements, the situation is not straightforward.

For its representation, the smallest volume V is assumed at the mesoscale around the material at point $P(x)$ in body B. According to the assumption, the microstructural defects in volume V can be statistically homogeneous, and the mechanical state of the material can be explained by the statistical average of the mechanical variables in V. If the considered volume V satisfies this condition then the volume V is called an RVE [23].

The material can be idealized as a continuum employing the statistical average of the mechanical state if an RVE of proper size can be taken at each point of the system. When an RVE is a statistical illustration of the material, then the mechanical state of the continuum is unique. For such RVE, following conditions need to be fulfilled [1]:

1. For statistical homogenization of the RVE, its size must be large enough to encapsulate a sufficient number of microstructural defects.
2. For representing a non-uniform macroscopic mechanical field utilizing a continuum, the size of the RVE must be significantly small to avoid the variation of the macroscopic variable in it, which will be minimal.

The order of the magnitude of an RVE can be different for different materials, i.e., it depends on the microstructure of the material. The typical sizes are as follows [1, 24]:

Metal and ceramic	$(0.1\,mm)^3$
Polymer and composites	$(1\,mm)^3$
Timber	$(10\,mm)^3$
Concrete	$(100\,mm)^3$

The size of an RVE also depends on the type of phenomenon under consideration. For instance, creep and ductile damage are far more localized than the brittle and fatigue damage so the RVE for brittle and fatigue damage must be larger than that of the creep and ductile damage.

2.5.2 Damage Variables

Damage mechanics is employed for the modeling and quantification of the damage. Generally, a damage model is utilized for this purpose which can illustrate different damage processes, damage growth, and the crack initiation.

The definition of a damage variable is not straightforward as there exist a variety of mechanisms which induce damage. Also, the shape and size of every micro-cavity are different which lead towards the difficulty in describing the geometry of every cavity. Therefore, researchers have attempted to propose an abstract damage variable which can be considered as scalar or tensor and can represent the phenomenological description for every micro-cavity. According to the thermodynamics, the damage variable must show the irreversible processes of microstructural changes within the material. Therefore, the damage variable is an internal variable [25] and must be capable of representing the damage growth. Furthermore, the damage variable should, in general, have a tensorial nature since the crack initiation and growth depends on the direction of the stress or strain in the RVE. The choice of a damage variable is not simple, as there are many aspects of evaluating damage which will be discussed in further sections. The fundamental consideration of the damage variable is the density of defects (cracks and voids) on a plane intersecting the RVE (Fig. 9). Many researchers have used the following variables for the modeling of damage within the thermodynamics of irreversible process as mentioned in Table 2.

Table 2: Set of variables utilized in CDM to model damage [25].

Observable Variables	Internal Variables	Associated Variables
Elastic strain tensor ε^e	Accumulative hardening parameter γ	Stress tensor σ
Temperature T	Damage variable D	Entropy s
		Isotropic hardening variable R
		Damage strain energy release rate Y

2.5.2.1 Scalar Damage Variable

Suppose a small volume of a damaged solid at the mesoscale around a material point in the body as shown in Fig. 9. Let δS be the area of the volume element intersecting the plane of the RVE identified by its normal $\vec{n}$ and δS_D be the active area of the intersection of microvoids or microcracks which reside in δS.

Therefore, the damage variable is:

$$D = \frac{\delta S_D}{\delta S}\,. \tag{1}$$

From the definition, it follows that the value of D is bounded by 0 and 1 $(0 \leq D \leq 1)$. 0 refers to an undamaged material whereas 1 refers to an entirely damaged material. In reality, failure can occur even at $D < 1$. The damage variable is considered scalar if the damage is isotropic, for instance, in the case of random or isotropic distribution of microvoids. However, in the case of anisotropic damage due to the oriented distribution of microvoids, the scalar damage variable can still be utilized if the density of microvoids is minimal. It is used for one-dimensional problems and also for easy evaluation of three-dimensional problems. Moreover, its mathematical procedure is simple than the tensorial damage variable.

2.5.2.2 Plural Damage Variables

In some situations, the use of a single damage variable is not sufficient to characterize the value of damage even if the distribution of microvoids is isotropic. For instance, there is a requirement of two damage variables when modeling the change in elastic properties due to the increasing damage even in isotropic materials [26]. Also, plural damage variables are needed, for example, in some models of creep-fatigue interaction where creep damage variable D_C and fatigue damage variable D_F are used separately. Furthermore, there can be more than one damage phenomenon present in the damage evolution which can be represented by two individual damage variables. For example, the delamination of fibers and the cracking of matrix in a conventional composite. In this case, up to three variables are used.

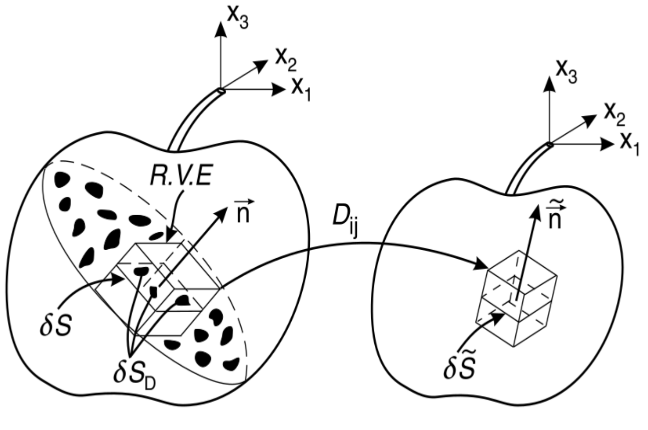

Figure 9: Schematic illustration of RVE [24].

2.5.2.3 Tensorial Damage Variable

Damage state is anisotropic when the microvoid distribution is oriented. Damage state is specified by the decrease in load carrying effective area due to void growth. Therefore, it is possible to formulate a tensorial damage variable. The density of microvoids in a plane with normal $\vec{n}$ acts through an operator which transforms the surface into smaller continuous area $\delta\tilde{S} = \delta S - \delta S_D$ and into another normal $\tilde{\vec{n}}$.

$$(\delta_{ij} - D_{ij})n_j \delta S = \tilde{n}_i \delta\tilde{S}\,, \tag{2}$$

where D_{ij} is a component of second order tensor while δ_{ij} is the Kronecker delta.

The damage variable of largest generality is the fourth order tensor as mentioned in literature [1]. As mentioned previously, consider an RVE having a damage area δS, a vector normal to it $\vec{n}$ and a reference vector $\vec{v}$ such that the tensor $v_i n_j \delta S$ is the geometrical reference configuration. CDM describes the effective continuous configuration through a modified area $\delta\tilde{S}$ and a modified normal $\tilde{\vec{n}}$ as illustrated in Fig. 10.

The damage $\mathbb{D}$ is a fourth order tensor which converts the second order tensor $v_i n_j \delta \mathrm{S}$ into an effective configuration of $v_i \tilde{n}_j \delta\tilde{S}$. Therefore:

$$(I_{ijkl} - D_{ijkl})v_k n_l \delta S = v_i \tilde{n}_j \delta\tilde{S}\,, \tag{3}$$

with the following symmetries $D_{ijkl} = D_{ijlk} = D_{jikl} = D_{klij}$.

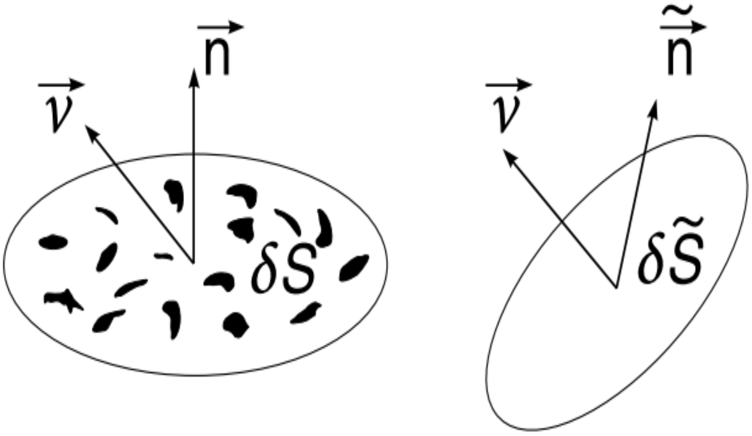

Figure 10: CDM approach for reference and effective configurations [25].

2.5.3 Effective Stress Concept

As shown in Fig. 9, the development of microvoids progresses due to the damage. The mechanical effect of the area δS is reduced by δS_D, since δS_D is the total void area in $\delta \mathrm{S}$.

$$\delta\tilde{S} = \delta S - \delta S_D \tag{4}$$

Now suppose the deformation of a cylindrical bar shown in Fig. 11. The bar in Fig. 11b is in damaged state D with an applied tensile load δF having a cross-sectional area δS. In this case, the actual load-carrying cross-sectional area or the effective area is $\delta\tilde{S}$ [11]. Therefore, using Eqs. (1) and (4), the effective area $\delta\tilde{S}$ is given by:

$$\delta\tilde{S} = (1 - D)\delta S \,. \tag{5}$$

The stress σ being generated in the result of the tensile load δF increased due to the reduction in the cross-sectional area. Using Eq. (5), the magnified stress $\tilde{\sigma}$ is given by:

$$\tilde{\sigma} = \frac{\delta F}{\delta\tilde{S}} = \frac{\sigma}{1 - D} \,. \tag{6}$$

Since all stress components act on the same effective area when multiaxial isotropic damage is considered, the effective stress second order tensor can be given by:

$$\tilde{\sigma}_{ij} = \frac{\delta F}{\delta\tilde{S}} = \frac{\sigma_{ij}}{1 - D} \,. \tag{7}$$

For the case of anisotropic damage, the representation of the effective stress tensor is complicated. The effective stress tensor is deduced from the general representation of the fourth order damage tensor as described in section 2.5.2.3. The effective stress tensor is defined by the projection of the stress tensor σ_{ij} on the referenve vector $\vec{v}$ as shown in Fig. 10.

$$\tilde{\sigma}_{ij}(I_{ijkl} - D_{ijkl})v_k n_l \delta S = \sigma_{kl} v_k n_l \delta S \tag{8}$$

The stress $\tilde{\sigma}$ is named as the effective stress [27, 28] since it is the increased magnitude of stress due to the area reduction that occurs due to the damage. However, this definition of the effective stress applies to the material in tensile loading [18]. In compression, some defects might close, but the overall damage remains same. If all of the defects close, then the effective stress $\tilde{\sigma}$ is equal to the normal stress σ.

With the help of Eqs. (5) and (6), it is notable that the damaged cylindrical bar of Fig. 11b with cross-sectional area δS and tensile force δF is mechanically equivalent to the undamaged cylindrical bar of Fig. 11c having a cross-sectional area $\delta\tilde{S}$ and the same tensile force δF. Consequently, the state of Fig. 11c is termed as fictitious undamaged bar [1, 25].

2.5.4 Basic Hypotheses in Damage Mechanics

For the derivation of constitutive and evolution equations of damage, the concept of effective stress and hypotheses of mechanical equivalence between the damaged and fictitious undamaged material are utilized, because they allow modeling of the damage state.

2.5.4.1 Hypothesis of Strain Equivalence

The hypothesis of strain equivalence was proposed by Lemaitre and Chaboche [1, 25] showing the mechanical equivalence between the damaged and fictitious undamaged materials. The hypothesis suggests that the inelastic constitutive equation of a damaged material with applied stress is equivalent to that of a fictitious undamaged material under the effective stress.

Suppose a damaged and a fictitious undamaged configuration as shown in Fig. 12 which includes the concept of effective stress. The effect of the applied stress σ on the configuration

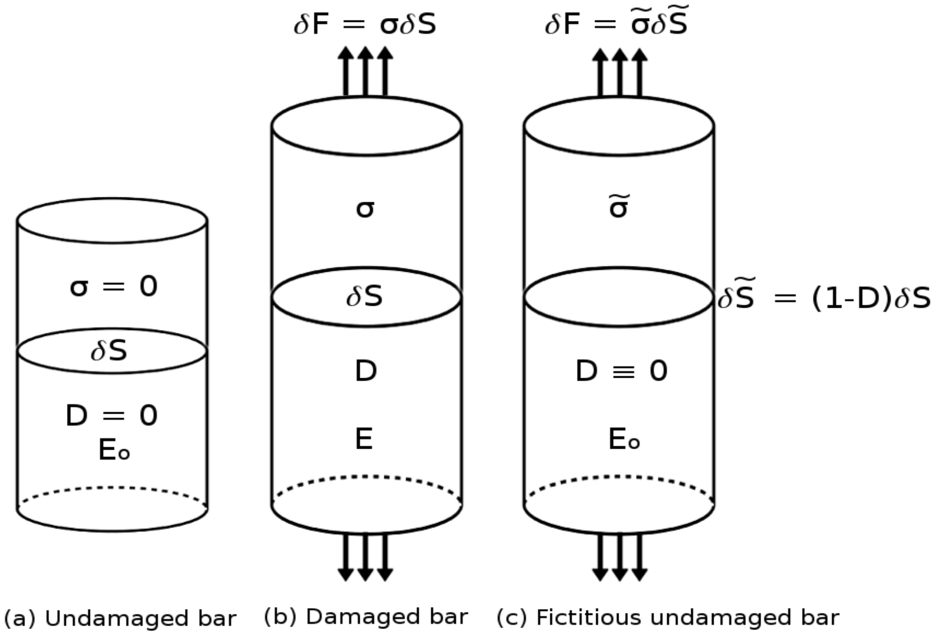

Figure 11: Illustration of damage of a bar under a tensile load.

in Fig. 12a is equivalent to the effect of the effective stress $\tilde{\sigma}$ on the configuration in Fig. 12b. Hence, the deformation of the damaged configuration should be equal to the fictitious undamaged configuration.

Various effective stress tensors have been provided in the literature [1] by researchers. A general form of an effective stress tensor can be given by:

$$\tilde{\sigma} = \mathbb{M}(\mathscr{D}) : \sigma \,, \tag{9}$$

where $\mathbb{M}(\mathscr{D})$ is a fourth-order tensor function and is called the damage effect tensor. It transforms the stress tensor σ into a corresponding effective stress tensor $\tilde{\sigma}$. The tensor $\mathscr{D}$ specifies an even-order damage tensor respectively among the zero, second and fourth order tensors D, $\mathbf{D}$, and $\mathbb{D}$.

Now suppose an inelastic undamaged material whose constitutive equation can be given as:

$$\varepsilon = F_o(\sigma, \alpha) \,, \tag{10}$$

where α denotes an internal parameter which expresses the changes in the material other than damage. Thus, according to the hypothesis mentioned earlier, the constitutive equation for a fictitious undamaged material with the damage variable $\mathscr{D}$ can be given by replacing the stress tensor σ by the effective stress tensor $\tilde{\sigma}$ in Eq. (10) [1]. Therefore:

$$\varepsilon = F(\sigma, \mathscr{D}, \alpha) = F_o(\tilde{\sigma}, \alpha) \,. \tag{11}$$

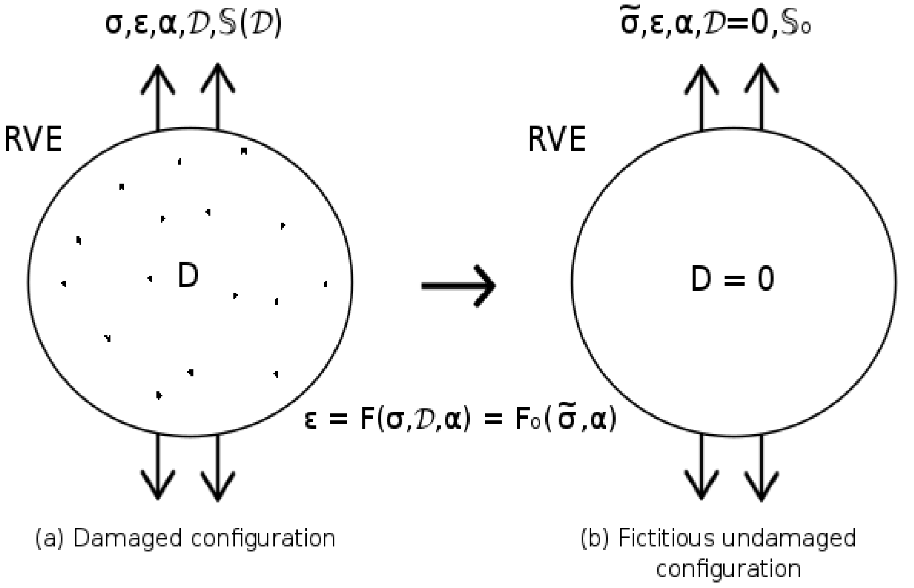

Figure 12: Configurations depicting hypothesis of strain equivalence.

When elastic deformation occurs then the constitutive equations for undamaged and damaged materials can be expressed as:

$$\varepsilon = \mathbb{S}_o : \sigma \tag{12a}$$
$$\varepsilon = \mathbb{S}(\mathscr{D}) : \sigma \,, \tag{12b}$$

where $\mathbb{S}_o$ and $\mathbb{S}(\mathscr{D})$ denotes the fourth-order compliance tensor of the respective materials. According to the hypothesis of strain equivalence, the elastic constitutive equation (Eq. (12b)) of the damaged material and relative compliance tensor $\mathbb{S}(\mathscr{D})$ can be given as:

$$\varepsilon = \mathbb{S}_o : \tilde{\sigma} = [\mathbb{S}_o : \mathbb{M}(\mathscr{D})] : \sigma = \mathbb{S}(\mathscr{D}) : \sigma \tag{13a}$$
$$\mathbb{S}(\mathscr{D}) = \mathbb{S}_o : \mathbb{M}(\mathscr{D}) \,. \tag{13b}$$

Also, the damage effect tensor is related to the compliance tensor as given below:

$$\mathbb{M}(\mathscr{D}) = \mathbb{S}_o^{-1} : \mathbb{S}(\mathscr{D}) \,. \tag{14}$$

Even though the hypothesis of strain equivalence is easily understandable and implementable, the compliance tensor $\mathbb{S}$ has disadvantage of its asymmetry [1]. However, the damage variable $\mathscr{D}$ is a state and is calculable through different methods. Therefore, a new compliance tensor $\mathbb{S}^*(D)$ can be defined by taking a new damage variable $\mathscr{D}^*$.

$$\mathbb{S}^*(D) = \frac{1}{2}[\mathbb{S}_o : \mathbb{M}(\mathscr{D}^*) + \mathbb{M}^T(\mathscr{D}^*) : \mathbb{S}_o] \tag{15}$$

Now $\mathbb{S}(\mathscr{D}^*)$ is symmetric and the new damage variable $\mathscr{D}^*$ is related to the damage variable $\mathscr{D}$ by means of the following relation:

$$\begin{aligned}\mathbb{M}(\mathscr{D}^*) &= \mathbb{S}_o^{-1} : \mathbb{S}^*(\mathscr{D}) \\ &= \frac{1}{2}[\mathbb{S}_o^{-1} : \mathbb{M}(\mathscr{D}^*) + \mathbb{M}^T(\mathscr{D}^*) : \mathbb{S}_o].\end{aligned} \tag{16}$$

The physical interpretation of the hypothesis of strain equivalence is depicted in Fig. 13. The stress-strain relation for the damaged material can be defined as:

$$\begin{aligned}\sigma &= \tilde{\mathbb{C}} : \varepsilon \qquad \text{or} \\ \sigma_{ij} &= \tilde{\mathbb{C}}_{ijkl}\varepsilon_{kl}.\end{aligned} \tag{17}$$

And that for the fictitious undamaged material can be defined as:

$$\begin{aligned}\tilde{\sigma} &= \mathbb{C} : \varepsilon \qquad \text{or} \\ \tilde{\sigma}_{ij} &= \mathbb{C}_{ijkl}\varepsilon_{kl},\end{aligned} \tag{18}$$

where $\tilde{\mathbb{C}}$ is the even-order tensor for the damaged material.

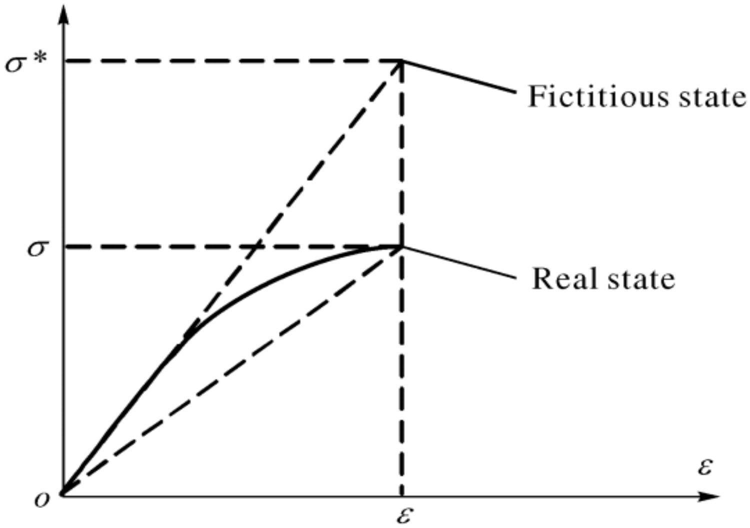

Figure 13: Schematic illustration of the hypothesis of strain equivalence [25].

According to the hypothesis, for an isotropic undamaged material, the effective stress $\tilde{\sigma}$ in Eq. (18) can be replaced according to the Eq. (6).

$$\frac{\sigma}{1-D} = \mathbb{C}\varepsilon \tag{19}$$

Considering Eq. (17) for an isotropic damage case and comparing it with Eq. (19), following expression can be obtained:

$$\tilde{\mathbb{C}} = (1-D)\mathbb{C}\,. \tag{20}$$

Eq. (20) gives the relationship formula between the damaged and the undamaged material. Thus, the following material properties variate with damage according to the relations given below:

$$\tilde{E} = (1-D)E \tag{21a}$$
$$\tilde{\nu} = \nu \tag{21b}$$
$$\tilde{G} = (1-D)G, \tag{21c}$$

where $\tilde{E}$, $\tilde{\nu}$, and $\tilde{G}$ are effective Young's modulus, effective Poisson's, and effective shear modulus of the elastic isotropic damaged material.

According to the Eqs. (21a), (21b), and (21c), it is clear that the properties of the damaged material are affected by the constant factor $\Psi = (1-D)$ except for the Poisson's ratio, which remains unaffected.

2.5.4.2 Hypothesis of Stress Equivalence

The hypothesis of stress equivalence (Sec. 2.5.4.1) has a contrary meaning to the hypothesis of strain equivalence in a similar way. The hypothesis proposes that stress corresponding to a damaged state under the actual strain is equivalent to the stress corresponding to its fictitious undamaged state under the effective strain [25].

The physical interpretation of the hypothesis of stress equivalence is illustrated in Fig. 14.

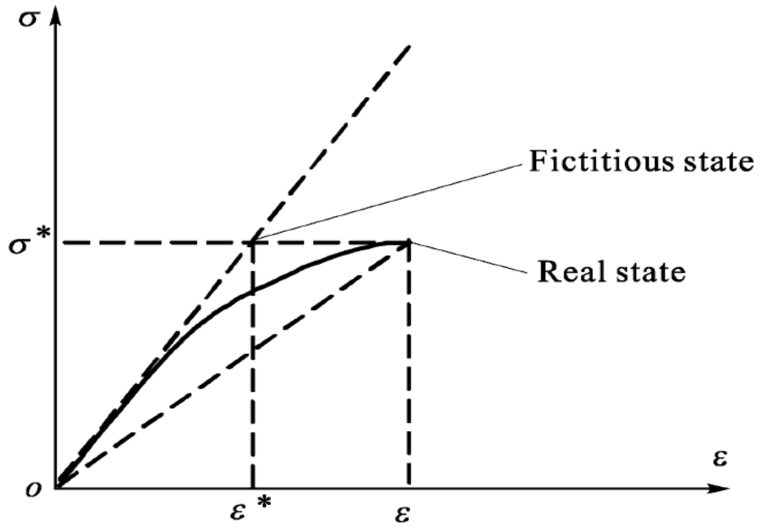

Figure 14: Schematic illustration of the hypothesis of stress equivalence [25].

The stress-strain relation for the damaged material can be defined as Eq. (17).

$$\sigma = \tilde{\mathbb{C}} : \varepsilon \qquad \text{or} \\ \sigma_{ij} = \tilde{\mathbb{C}}_{ijkl}\varepsilon_{kl} \tag{22}$$

For the fictitious undamaged state, according to the hypothesis, the stress-strain relation can be defined as:

$$\begin{aligned} \tilde{\sigma} &= \mathbb{C} : \varepsilon \qquad \text{or} \\ \tilde{\sigma}_{ij} &= \mathbb{C}_{ijkl}\varepsilon_{kl}\,. \end{aligned} \tag{23}$$

Considering that the constant factor Ψ or the damage variable D are defined by effective elastic modulus as:

$$\Psi = \frac{\tilde{E}}{E} \qquad \text{or} \tag{24a}$$

$$D = 1 - \frac{\tilde{E}}{E}\,. \tag{24b}$$

In case of one-dimensional damage, the stress-strain relation is $\sigma = \tilde{E}\varepsilon$ while the stress-strain relation for the fictitious undamaged state can be given by $\sigma = E\tilde{\varepsilon}$. Therefore, according to the hypothesis of stress equivalence:

$$\tilde{\varepsilon} = \frac{\tilde{E}}{E}\varepsilon = \Psi\varepsilon = (1-D)\varepsilon\,. \tag{25}$$

Thus, it can be understood that according to the hypothesis of stress equivalence, the stress-relation of damaged material and fictitious undamaged materials are equivalent when the real strain ε is replaced by the effective strain $\tilde{\varepsilon}$.

2.5.4.3 Hypothesis of Complementary Strain Energy Equivalence

The hypotheses of stress and strain equivalence are rational regarding their ease of application to isotropic damage state. The deformation due to the real stress to a damaged material is equivalent to the deformation due to the effective stress to an undamaged material. However, in the anisotropic case, the implementation is not simple due to the asymmetric effective stress tensor.

The cope up with this, Cordebois and Sidoroff [29] proposed a hypothesis considering energy equivalence between the damaged and the fictitious undamaged material. This hypothesis provides the symmetry requirement of elastic tensors of the materials. The hypothesis states that the complementary strain energy function of the damaged material is equivalent to that of the undamaged material if the effective stress replaces the stress in the latter.

Consider a damaged and an undamaged configuration of an elastic-plastic material as shown in Fig. 15, where the internal state variable α represents the change in the material due to plastic deformation. The complementary strain energy functions of the damaged and undamaged configurations can be represented as follows [1]:

$$V_o(\sigma,\alpha) = \frac{1}{2}\sigma : \mathbb{S}_o : \sigma - \phi(\alpha) \tag{26a}$$
$$V(\sigma,\mathscr{D},\alpha) = \frac{1}{2}\sigma : \mathbb{S}(\mathscr{D}) : \sigma - \phi(\alpha)\,. \tag{26b}$$

Now, the elastic constitutive equations can be defined as:

$$\varepsilon = \frac{\partial V_o}{\partial \sigma} = \mathbb{S}_o : \sigma \tag{27a}$$
$$\varepsilon = \frac{\partial V}{\partial \sigma} = \mathbb{S}(\mathscr{D}) : \sigma\,. \tag{27b}$$

According to the hypothesis, the constitutive equation can be derived by replacing the real stress σ with the effective stress $\tilde{\sigma}$ in Eq. (26a). Thus:

$$V(\sigma,\mathscr{D},\alpha) = V_o(\tilde{\sigma},\alpha)\,. \tag{28}$$

Using the hypothesis, the equation for elastic strain (Eq. (27b)) leads to:

$$\begin{aligned}\varepsilon &= \frac{\partial V(\sigma,\mathscr{D},\alpha)}{\partial \sigma} = \mathbb{S}(\mathscr{D}) : \sigma \\ &= \frac{\partial V_o(\tilde{\sigma},\alpha)}{\partial \sigma} = \frac{\partial}{\partial \sigma}\left(\frac{1}{2}\tilde{\sigma} : \mathbb{S}_o : \tilde{\sigma}\right) \\ &= \frac{1}{2}\frac{\partial}{\partial \sigma}[(\mathbb{M}(\mathscr{D}) : \sigma) : \mathbb{S}_o : (\mathbb{M}(\mathscr{D}) : \sigma)] \\ &= [\mathbb{M}^T(\mathscr{D}) : \mathbb{S}_o : \mathbb{M}(\mathscr{D})] : \sigma\,.\end{aligned} \tag{29}$$

The result of Eq. (29) leads to the elastic compliance tensor of the damaged material, given as:

$$\mathbb{S}(\mathscr{D}) = \mathbb{M}^T(\mathscr{D}) : \mathbb{S}_o : \mathbb{M}(\mathscr{D})\,. \tag{30}$$

According to the Eq. (30), the tensors $\mathbb{S}(\mathscr{D})$ and $\mathbb{S}_o$ uniquely describe the damage effect tensor $\mathbb{M}(\mathscr{D})$. The symmetric form of $\mathbb{M}(\mathscr{D})$ can be defined as:

$$\mathbb{M}(\mathscr{D}) = \sqrt{\sqrt{\mathbb{S}_o^{-1}} : \mathbb{S}(\mathscr{D}) : \sqrt{\mathbb{S}_o^{-1}}}\,. \tag{31}$$

Moreover, using Eq. (9), a new effective strain tensor can be defined as:

$$\tilde{\varepsilon} = \mathbb{M}^{-T}(\mathscr{D}) : \varepsilon\,. \tag{32}$$

According to Cordebois and Sidoroff [29], the elastic constitutive equation (Eq. (26b)) can then be written as:

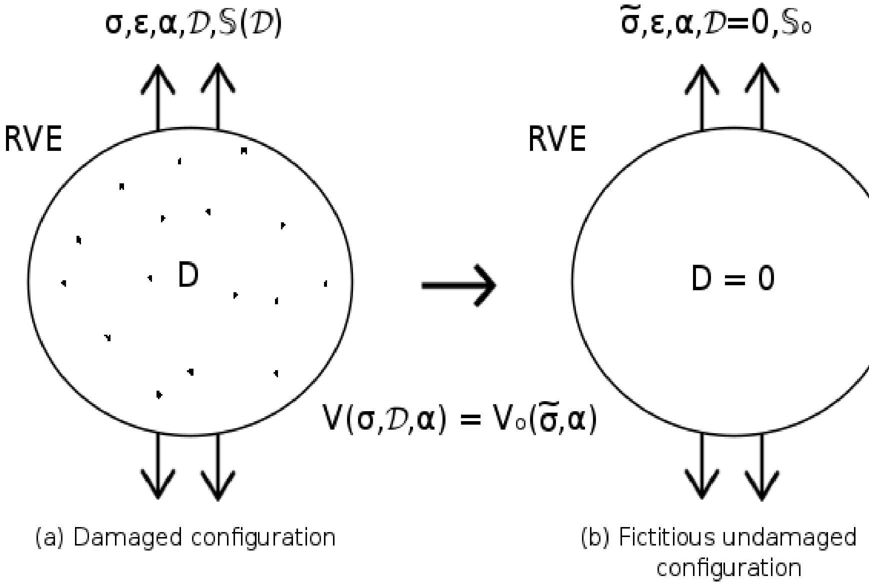

Figure 15: Configurations depicting hypothesis of complementary strain energy equivalence.

$$\begin{aligned} V &= \frac{1}{2}\sigma : \varepsilon - \phi(\alpha) = \frac{1}{2}\tilde{\sigma} : \tilde{\varepsilon} - \phi(\alpha) \\ \tilde{\varepsilon} &= \mathbb{S}_o : \tilde{\sigma} \,. \end{aligned} \tag{33}$$

The physical interpretation of the hypothesis of complementary strain energy equivalence is shown in Fig. 16.

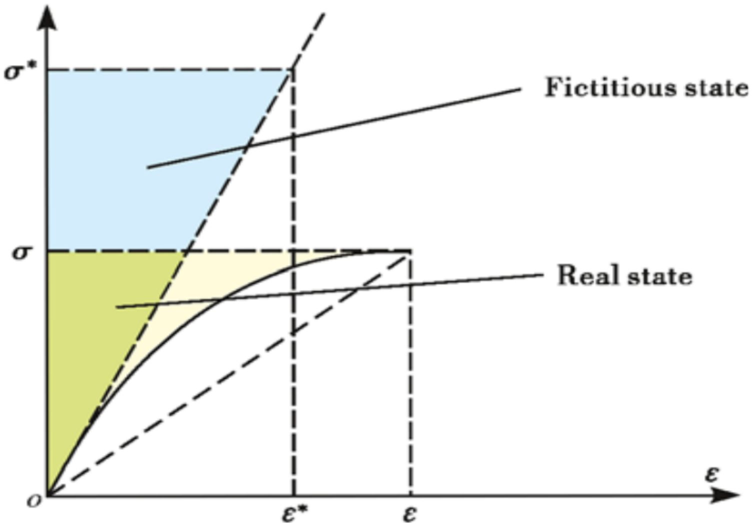

Figure 16: Schematic illustration of the hypothesis of complementary strain energy equivalence [25].

As defined in Eq. (20), the relationship formula between the damaged and undamaged material under the hypothesis of complementary strain energy equivalence is given as [25]:

$$\tilde{D} = (1 - D)^2 \mathscr{D}\,. \tag{34}$$

Therefore, the following material properties change with damage according to the relations given below:

$$\tilde{E} = (1 - D)^2 E \tag{35a}$$

$$\tilde{\nu} = \nu \tag{35b}$$

$$\tilde{G} = (1 - D)^2 G\,. \tag{35c}$$

Hence, according to the hypothesis, it can be comprehended that the constitutive equations of damaged and fictitious undamaged materials are equivalent when both the real stress σ and strain ε are replaced by the effective stress $\tilde{\sigma}$ and strain $\tilde{\varepsilon}$ respectively.

2.5.4.4 Hypothesis of Elastic Strain Energy Equivalence

Similar to the hypothesis of complementary strain energy equivalence (Sec. 2.5.4.3), the hypothesis of elastic energy equivalence utilizes the effective strain rather than the effective stress in the strain energy function [29]. It states that the strain energy function of the damaged material can be represented as the strain energy function of the undamaged material by replacing the strain with the effective strain.

The strain energy functions for the damaged and undamaged materials can be expressed as:

$$W_o(\varepsilon, \alpha) = \frac{1}{2} \varepsilon : \mathbb{C}_o : \varepsilon + \phi(\alpha) \tag{36a}$$

$$W(\varepsilon, \mathscr{D}, \alpha) = \frac{1}{2} \varepsilon : \mathbb{C}(\mathscr{D}) : \varepsilon + \phi(\alpha), \tag{36b}$$

where $\mathbb{C}_o$ and $\mathbb{C}(\mathscr{D})$ are the elastic modulus tensors. Therefore, the elastic constitutive equations of the damaged and undamaged materials can be defined as:

$$\sigma = \frac{\partial W_o}{\partial \varepsilon} = \mathbb{C}_o : \varepsilon \tag{37a}$$

$$\sigma = \frac{\partial W}{\partial \varepsilon} = \mathbb{C}(\mathscr{D}) : \varepsilon\,. \tag{37b}$$

According to the hypothesis, the constitutive equation can be derived by replacing the real strain ε with the effective strain $\tilde{\varepsilon}$ in Eq. (36a). Therefore:

$$W(\varepsilon, \mathscr{D}, \alpha) = W_o(\tilde{\varepsilon}, \alpha)\,. \tag{38}$$

In case of one-dimensional damage,the hypothesis of elastic strain energy equivalence:

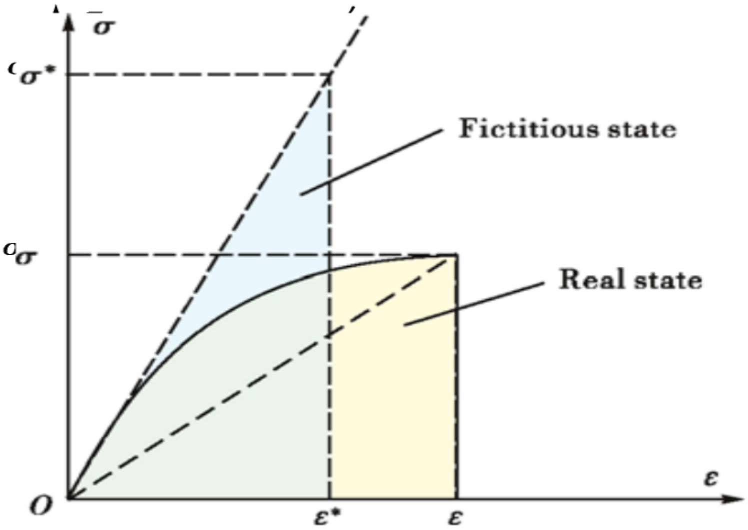

Figure 17: Schematic illustration of the hypothesis of elastic strain energy equivalence [25].

$$\tilde{\varepsilon} = \left(\frac{\tilde{E}}{E}\right)^{1/2} \varepsilon = \Psi^{1/2} \varepsilon = (1-D)^{1/2} \varepsilon \,. \tag{39}$$

Similar to the hypothesis of complementary strain energy equivalence, the relationship formula between the damaged and undamaged material is identical to Eq. (34). Hence, the corresponding material properties of the damaged material are also the same as mentioned in Eq. (35). The physical interpretation of the hypothesis of elastic energy equivalence is depicted in Fig. 17.

2.5.4.5 Hypothesis of Total Energy Equivalence

The hypotheses of energy equivalence (Sec. 2.5.4.3 and Sec. 2.5.4.4) are reasonable to utilize as they have the feature of defining the equivalence between the damaged and the fictitious undamaged material through the state of energy, which shows each effect of stress and strain. Furthermore, they also ensure the symmetry of the elastic modulus and compliance tensors. However, they are relevant for the case of elastic state [1].

Saanouni et al. [30] overcame this constraint by reviewing the problem under the domain of irreversible thermodynamics with internal variables and postulated the hypothesis of total energy equivalence for thermo-inelastic deformation accompanied by isotropic damage by extending the energy equivalence hypothesis proposed by Cordebois and Sidoroff.

Consider an RVE for the damaged configuration of Fig 18a by assuming that the following set of state variables can define the inelastic damage state:

$$(\sigma, \varepsilon^e), \quad (R, r), \quad (A, \alpha), \quad (T, -s), \quad (Y, D)\,, \tag{40}$$

where σ, R, A, T, and Y denote the stress tensor, isotropic hardening variable, kinematic hardening variable, temperature, and the strain energy release rate due to damage respectively, with the damage variable D. Other symbols such as ε^e, r, and α are the elastic strain, the associated variables of R and A, and the entropy of the configuration respectively.

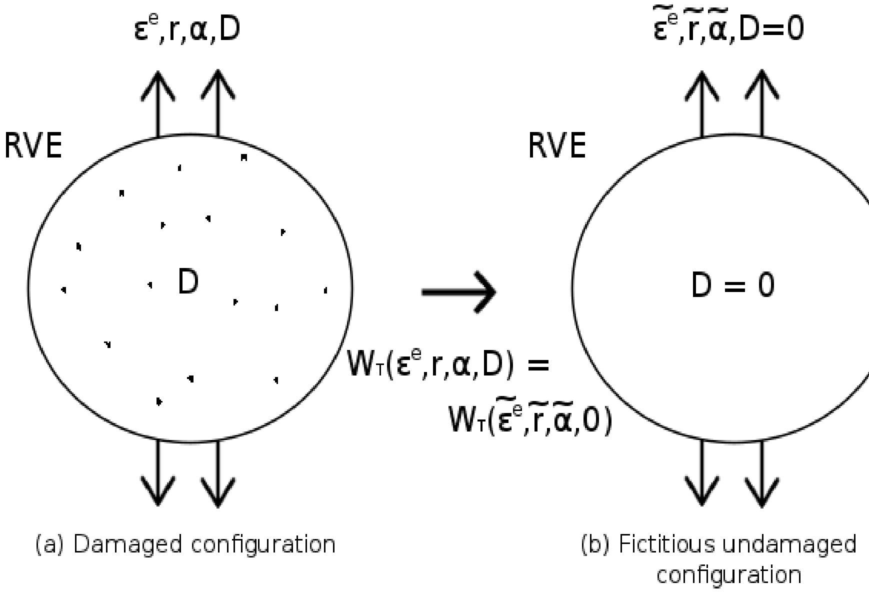

Figure 18: Configurations depicting hypothesis of total energy equivalence.

Consider another RVE for the fictitious undamaged configuration of Fig. 18b having similar total strain energy W^T. Concerning Eq. (40), the following set of effective variables can be expressed as:

$$(\tilde{\sigma}, \tilde{\varepsilon}^e), \quad (\tilde{R}, \tilde{r}), \quad (\tilde{A}, \tilde{\alpha}), \quad (T, -s), \quad (Y = 0, D = 0). \tag{41}$$

The total strain energy W_T in both the configuration can be defined as the sum of the reversible elastic energy W_E and that of the irreversible isotropic hardening W_I and the kinematic hardening W_K.

$$W_T(\varepsilon^e, r, \alpha, D) = W_T(\tilde{\varepsilon}^e, \tilde{r}, \tilde{\alpha}, D = 0) = W_E + W_I + W_K \tag{42}$$

As both the configurations are mechanically equivalent, the following relations must fulfill:

$$W_E(\varepsilon^e, D) = W_E(\tilde{\varepsilon}^e, 0) = \frac{1}{2}\sigma : \varepsilon^e = \frac{1}{2}\tilde{\sigma} : \tilde{\varepsilon}^e \tag{43a}$$

$$W_I(r, D) = W_I(\tilde{r}, 0) = \frac{1}{2}Rr = \frac{1}{2}\tilde{R}\tilde{r} \tag{43b}$$

$$W_K(\alpha, D) = W_K(\tilde{\alpha}, 0) = \frac{1}{2}A : \alpha = \frac{1}{2}\tilde{A} : \tilde{\alpha}. \tag{43c}$$

When the effective variables $\tilde{\sigma}$, $\tilde{\varepsilon}$, $\tilde{R}$, $\tilde{r}$, $\tilde{A}$, and $\tilde{\alpha}$ are defined as below, the relations (Eq. (43)) are always fulfilled.

$$\tilde{\sigma} = \frac{\sigma}{g(D)}, \quad \tilde{\varepsilon}^e = g(D)\varepsilon^e \tag{44a}$$

$$\tilde{R} = \frac{R}{h_1(D)}, \quad \tilde{r} = h_1(D)r \tag{44b}$$

$$\tilde{A} = \frac{a}{h_2(D)}, \quad \tilde{\alpha} = h_2(D)\alpha\,, \tag{44c}$$

where the scalar functions $g(D)$, $h_1(D)$, and $h_2(D)$ are the positive decreasing function of the damage variable D. According to the Saanouni et al. [30], these functions satisfy the following condition:

$$g(D) = h_1(D) = h_2(D) = (1 - D)^{1/2}\,, \tag{45}$$

and proposed the hypothesis that the mechanical behavior of the material in the damaged configuration is derived from the state- and the dissipation-potential functions of the equivalent material in the fictitious undamaged configuration by replacing the state variables with the effective state variables.

2.6 Damage Measurement

Except for the direct measurement, the damage is calculated by its coupling to the internal material properties, for instance, elasticity. Following are few of the damage measurement techniques, where the strain equivalence hypothesis is assumed.

2.6.1 Variation of Effective Area

Kachanov [27] studied the brittle creep damage of metal through uni-axial experiments and observed that creep damage occurs due to the microvoids that were developed during the process. He modeled the state of damage by a scalar damage variable Ψ $(0 \leq \Psi \leq 1)$, where 0 signifies the undamaged state and 1 signifies the complete damage state, i.e., the specimen is broken. Moreover, he proposed a damage evolution equation:

$$\dot{\Psi} = -A\Big(\frac{\sigma}{\Psi}\Big)^m. \tag{46}$$

where $(\dot{\ })$ represents the time-derivative, whereas A and m are the material parameters.
Afterwards Rabotnov [28] modified Kachanov's theory and presented a new scalar damage variable D = 1 - Ψ $(0 \leq D \leq 1)$ and by proposing that the creep rate $\dot{\varepsilon}$ is affected by damage, which can be expressed as:

$$\dot{D} = A\Big(\frac{\sigma}{1 - D}\Big)^m \tag{47a}$$

$$\dot{\varepsilon} = B\Big(\frac{\sigma}{1 - D}\Big)^n, \tag{47b}$$

where A, B, m, and n are material parameters. Eq. (47) is referred to as the Kachanov-Rabotnov theory which is the fundamental theory for many continuum damage models. The damage variables D and Ψ are understood as the reduction in the load-carrying effective area due to microvoid nucleation.

As described previously (Sec. 2.5.3), the effective area is given by Eq. (5). Therefore, the damage variables D and Ψ can be expressed as:

$$\Psi = \frac{\delta\tilde{S}}{\delta S} \tag{48a}$$

$$D = 1 - \Psi = \frac{\delta S - \delta\tilde{S}}{\delta S} = \frac{\delta S_D}{\delta S} . \tag{48b}$$

Even though the Kachanov-Rabotnov model is quite simple in approach, the actual damage process is much more complicated, and thus the model has limited validity [1]. A precise description of damage phenomenon is discussed in the damage models that have been proposed subsequently [1, 12, 13, 18, 24, 25, 31].

2.6.2 Variation of Young's Modulus

Since there is a reduction of stiffness of the RVE in the material due to the nucleation of microvoids and microcracks, the damage can be modeled as the variation of Young's modulus [18].

Suppose a damaged bar and a fictitious undamaged bar as shown in Fig. 11. According to the hypothesis of strain equivalence (Sec. 2.5.4.1) and the effective stress concept (Sec. 2.5.3), the strain ε in the bar (b) under the stress σ is equal to the strain ε in the bar (c) under the effective stress $\tilde{\sigma}$. Therefore:

$$\sigma = \tilde{E}\varepsilon\,,\ \tilde{\sigma} = E\varepsilon \quad \text{or} \tag{49a}$$

$$\varepsilon = \frac{\sigma}{\tilde{E}} = \frac{\tilde{\sigma}}{E}\,, \tag{49b}$$

where E and $\tilde{E}$ are the Young's moduli of the material in undamaged and damaged state respectively. A new definition of the effective stress can be expressed as:

$$\tilde{\sigma} = \frac{E}{\tilde{E}}\sigma\,. \tag{50}$$

Considering the effective stress definition as defined in Eq. (6) and the one described above in Eq. (50), the damage variable depending on the variation of Young's modulus can be express as:

$$\tilde{E} = (1-D)E \tag{51a}$$

$$D = 1 - \frac{\tilde{E}}{E}\,. \tag{51b}$$

The application of this method is achieved by measuring the elastic modulus from the hysteresis loop data. It is usually done by setting up an experiment (Fig. 19) that measures the strain utilizing strain extensometer during unloading. The damage can also be determined as a function of the accumulated plastic strain $p = \int_0^t \dot{p}\,dt$ for an LCF experiment. As shown in Fig. 19, Young's modulus decreases per successive cycles and the damage continues to increase. At about 30% of the accumulated plastic strain p, the is an extraordinary increase in the damage that continues to increase up to fracture. This behavior is also seen in our experiments, which is discussed later in Sec. 4.

This technique can be used to determine any type of damage, but it needs much care for the measurement of strain because the damage is not uniformly distributed in the volume on which the strain is measured which is the main limitation of the procedure.

Other non-linearity precautions must also be undertaken. For instance, for ductile or LCF damage in metals, there is a slight decrease in Young's modulus during the first few cycles. Reversible movements of dislocations cause microplasticity which is the cause of this non-linearity [18].

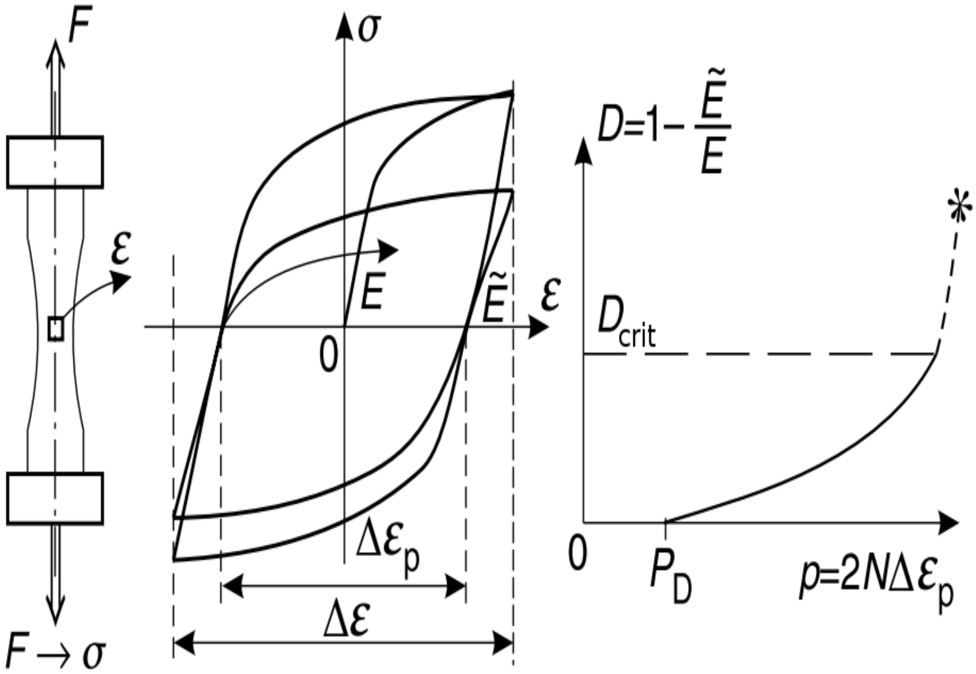

Figure 19: Damage measurement utilizing variation of Young's modulus [18].

2.6.3 Variation of Young's Modulus by Ultrasonic Waves Propagation

The damage state can also be characterized by the evaluation of variation of Young's modulus by measuring the propagation of ultrasonic waves. The speed of a wave is related to a solid material through its density ρ and elastic properties [18]. Suppose the longitudinal waves in an isotropic, linear, and elastic cylindrical bar with Poisson's ratio ν and Young's modulus E, the wave speed is given by:

$$v^2 = \frac{E}{\rho}\frac{(1-\nu)}{(1+\nu)(1-2\nu)}. \tag{52}$$

When the material is damaged, Young's modulus decreases with increasing damage, but density remains the same if the damage consists mainly of microcracks and the Poisson's ratio also remains the same if the microcracks are distributed randomly. The wave speed then becomes:

$$\tilde{v}^2 = \frac{\tilde{E}}{\rho} \frac{(1-\nu)}{(1+\nu)(1-2\nu)}. \tag{53}$$

The damage then can be calculated as:

$$D = 1 - \frac{\tilde{v}^2}{v^2}. \tag{54}$$

This method is a time of flight experiment, i.e., the time of propagation of the waves is measured for the damage evaluation. The limitation of this method is that it requires the distance covered by the waves to be large, but due to the localization of the damage, the distance covered is small. Therefore, for metals, this method may not be accurate enough, but for concretes (Fig. 20), it works accurately with a frequency of 0.1 KHz to 1 MHz. Another limitation is the size, for metals, because the size of ultrasonic transducers is large in comparison to the specimens [18].

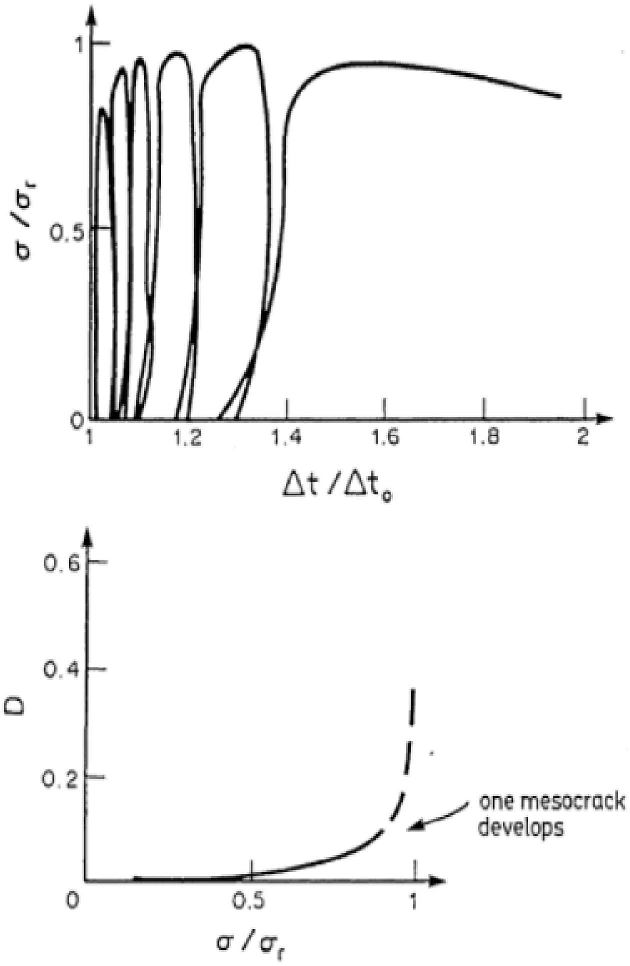

Figure 20: Evolution of brittle damage in a concrete through ultrasonic waves propagation [18].

The following ranges of frequency can be used:

• Metals	1.0 - 50 MHz
• Polymers	1.0 - 5 MHz
• Woods	1.0 - 5 MHz
• Concrete	1.0 - 1 MHz

2.6.4 Variation of Density by Void Volume Fraction

In ductile metals, the damage can be caused by the nucleation and coalescence of microvoids. These defects can be formed due to the plastic deformation, e.g., by the fracture of inclusions, by grain boundary sliding or by the decohesion of the interface between the matrix and the inclusions. Thus, the damage state can be characterized by the void volume fraction f of the material [32].

Consider an RVE of a material at point P(x) as shown in Fig. 21. Suppose dV, dV_o and dV_D be the volume of RVE, the volume of the matrix, and the volume of the microvoids respectively. The void volume fraction f can be expressed by:

$$f = \frac{dV - \mathrm{d}V_o}{\mathrm{d}V} = \frac{\mathrm{d}V_D}{\mathrm{d}V} \,. \tag{55}$$

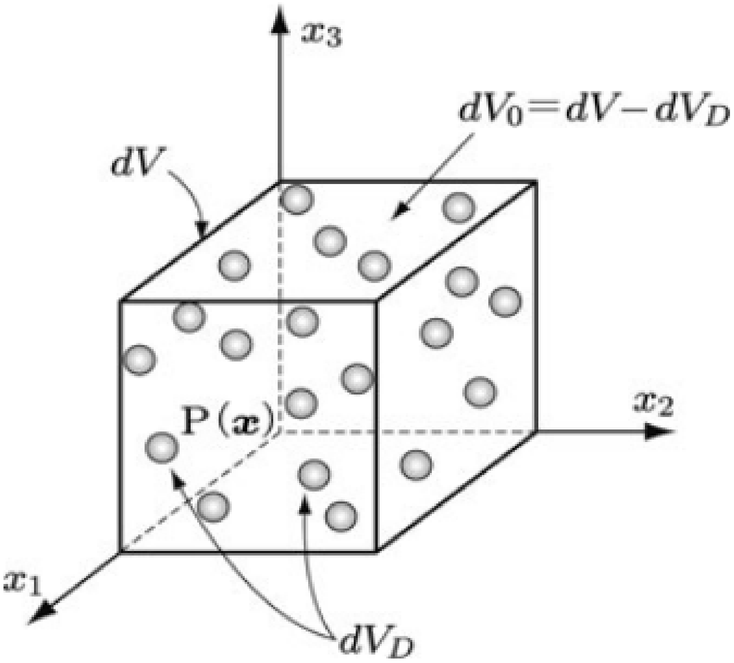

Figure 21: An RVE of a material with microvoids [1].

The direct measurement of the void volume fraction is a complicated task. On the other hand, it is simple to measure the density because it decreases as the microvoids continue to nucleate and coalesce [1]. Therefore, if the density of the damaged and the undamaged material is $\tilde{\rho}$ and ρ respectively, then void volume fraction can be written as:

$$\begin{aligned} f &= \frac{\rho - \tilde{\rho}}{\rho} = 1 - \frac{\tilde{\rho}}{\rho} \quad \text{or} \\ D &= f = 1 - \frac{\tilde{\rho}}{\rho} \,. \end{aligned} \tag{56}$$

In this work, it is attempted to measure the volume of the defects by first performing Computed Tomography (CT) and then calculating the volume of defects via VGSTUDIO MAX[1] visualization software.

The main limitation of this method is that it can only be used for the efficient evaluation of ductile damage. Also, the voids considered in the method are roughly spherical. Therefore, its application is limited to ductile damage in metals.

2.6.5 Variation of Microhardness

Microhardness is related to the damage state through the softening effect based on the plasticity-yield criterion (uniaxial state of stress) through the kinetic coupling. It is observed that hardness of the damaged material decreases with increasing damage. The hardness is defined as the resistant to plastic deformation induces by mechanical indentation or abrasion. The process of inserting a diamond indenter in the material where the load F and the projected area S are measured and express the hardness as:

$$H = \frac{F}{S} \,. \tag{57}$$

When the isotropic damage is supposed with the same effect on tension and compression, the plasticity-yield criterion can be expressed by the effective stress σ, the yield stress σ_Y and the isotropic hardening stress R as [1]:

$$\left| \frac{\sigma}{1 - D} \right| - R - \sigma_Y = 0 \,. \tag{58}$$

From this relation (Eq. (58)), the plastic yield stress in the material can be written as:

$$\sigma_s = (\sigma_Y + R)(1 - D) \,. \tag{59}$$

Extensive experimentation and theoretical analysis provide a linear relationship between the hardness and the plastic yield stress as following [18, 25]:

$$H = k \sigma_s \,, \tag{60}$$

---

[1] `https://www.volumegraphics.com/en/products/vgstudio-max.html`

where k is the proportionality coefficient.
When the microhardness test is performed on the virgin part of a material where there is no hardening effect, the hardness is expressed as:

$$H = k\sigma_Y\,. \tag{61}$$

When the microhardness is performed on the damaged part of the same material where there is quasi-saturated hardening ($R + \sigma_Y \approx \sigma_u$) [24], the hardness is expressed as:

$$H = k\sigma_Y\,, \tag{62}$$

where σ_u is the ultimate stress. From Eqs. (61) and (62), the damage state can be determined as:

$$D = 1 - \frac{\tilde{H}}{H}\frac{\sigma_Y}{\sigma_u}\,. \tag{63}$$

This method to determine damage is as effective as the elasticity method, but the only limitation is that the internal stresses in this method are not considered which are often distributed in zones subjected to a high amount of plastic strains and may increase or decrease the damage [18].

2.6.6 Variation in Electrical Resistance

The damage can also be evaluated as the variation in the electrical resistance of the material also known as potential drop method. As the effective stress is defined, the effective intensity of the electrical resistance can also be defined as:

$$\tilde{I} = \frac{I}{1-D}\,, \tag{64}$$

where $\tilde{I}$ is the intensity which exists in the damaged volume element.
Considering Ohm's law, the potential difference V is related to the resistivity R for an undamaged material of length L and area S as:

$$V = R\frac{L}{S}I\,. \tag{65}$$

Also, for the damaged material of the same length L and area S, the relation becomes:

$$\tilde{V} = \tilde{R}\frac{L}{S}\tilde{I}\,, \tag{66}$$

where $\tilde{R}$ is the effective resistivity of damaged material due to the change of volume.
For the same intensity I of the current for both undamaged and damaged materials, the damage may be evaluated as:

$$
\begin{aligned}
\frac{V}{\tilde{V}} &= \frac{R}{\tilde{R}}\frac{L/S.I}{L/S.I/1-D} \\
D &= 1 - \frac{V}{\tilde{V}}\frac{\tilde{R}}{R} .
\end{aligned}
\tag{67}
$$

For small values of D, the $\tilde{R}/R$ value is close to 1 due to the change of volume [18]. Therefore, damage is defined as:

$$
D \simeq 1 - \frac{V}{\tilde{V}} . \tag{68}
$$

2.7 Damage Evolution and Constitutive Equations of Material with Isotropic Damage

In this section, a brief concept of continuum in thermodynamics is presented to derive the constitutive and damage evolution equations.

2.7.1 Concept of Continuum in Thermodynamics

A thermodynamic system consists of variables which characterize its state. Among these variables, the variables which specify the current state are called state variables. The state of the system is said to be in thermodynamic equilibrium, if there is no change in the state variables with respect to time, while the system is non-equilibrium if the state variables change with respect to time due to the action of some forces. The change brought about by these forces is called a thermodynamic process. If the change in the state of the system is reversed by reversing the action of the forces, the process is called reversible, whereas if the change is not reversed, then the process is called irreversible.

The internal states of a continuum, for example, strain and temperature may differ from one location to another and change with time, when it experiences the process of deformation [1]. Therefore, it is deducible that the thermodynamic state of a continuum is non-uniform, is in a non-equilibrium state, and the process is irreversible. However, this non-equilibrium process cannot be explained by classical thermodynamics. To solve this issue, the principle employed to discuss the above problem in continuum thermodynamics is the principle of local state [33]. The principle of local state states that in a small element of a material at a given point in a body, a thermodynamic state of the element at any given time is specified by a set of state variables. Even if the element is in a non-equilibrium state, the state variables at any time are specified by the same thermodynamic relations as for the equilibrium condition. Thus, this hypothesis postulates that a material element in a continuum in an equilibrium state shows a similar thermodynamic response to the one in the non-equilibrium state.

By using the first and the second law of thermodynamics and the employment of Gauss' divergence theorem along with Reynold's transport theorem [1], gives the following relation:

$$
\sigma : \dot{\varepsilon} - \rho(\dot{\Psi} + \dot{T}s) - q \, . \, \frac{\operatorname{grad} T}{T} \geq 0 , \tag{69}
$$

where q is the heat supplied to the system and $\Psi = e - Ts$ is the Helmholtz free energy. Eq. (69) is called the Clausius-Duhem inequality which must be satisfied for every process [34]. Besides, this relation is the base for the thermodynamic constitutive theory for a continuum and puts vital restrictions on the constitutive equations.

2.7.2 1D Inelastic Constitutive Equations

In materials having a random distribution of the microcracks or the isotropic distribution of the microvoids, the damage induced can be evaluated as isotropic damage. Also, the damage in the material even having a specific distribution of the defects can be considered isotropic, if their size and density are minimal. In this case, the damage can be represented by the scalar damage variable D.

Consider the uniaxial (tensile) loading of a strain hardening elastic-plastic material as shown in Fig. 22. The damage D in the material starts when the plastic strain ε^p reaches to a threshold plastic strain ε^p_D and then with increasing ε^p, the damage D increases. When fracture plastic strain ε^p_R is attained, the damage D attains to a critical damage D_{crit} value and material starts to fracture. The damage then can be calculated by using Eq. (51b).

The curve of Fig. 22 from the yield stress point up to the ultimate tensile stress in the strain hardening region represents strain hardening. The subsequent yield stress, which is required to induce succeeding plastic strain, increases with the plastic strain ε^p. The increment in this subsequent yield stress is the strain hardening. Therefore, it is plausible to express the subsequent yield stress as the sum of the actual yield stress σ_Y, isotropic hardening variable R, and the kinematic hardening variable A. Thus:

$$\sigma = \sigma_Y + R + A. \tag{70}$$

By using a yield function f, Eq. (70) can be written as:

$$f = |\, \sigma - A \,| - R - \sigma_Y = 0, \tag{71}$$

which characterizes the evolution of plastic strain ε^p in the material as $\dot{\varepsilon}^p \neq 0$, for $f = 0$ and $\dot{f} = 0$ and $\dot{\varepsilon}^p = 0$, for $f < 0$ and $\dot{f} < 0$.
For a damaged material, by using the hypothesis of strain energy equivalence, the yield function becomes:

$$f = |\, \tilde{\sigma} - A \,| - R - \sigma_Y = 0. \tag{72}$$

The Eqs. (71) and (72) are called the 1D elastic-plastic constitutive equations and are the base for the 3D constitutive equations.
The increment of stress accompanies deformation typically, but the viscoplastic deformation could result from constant stress. For instance, in metallic materials at temperatures above 1/3 of the melting temperature, time-dependent deformation at constant stress can be observed. This phenomenon of time-dependent irreversible deformation under constant stress is called viscous deformation [1] and the time-dependent plastic deformation under constant stress is called viscoplastic deformation.

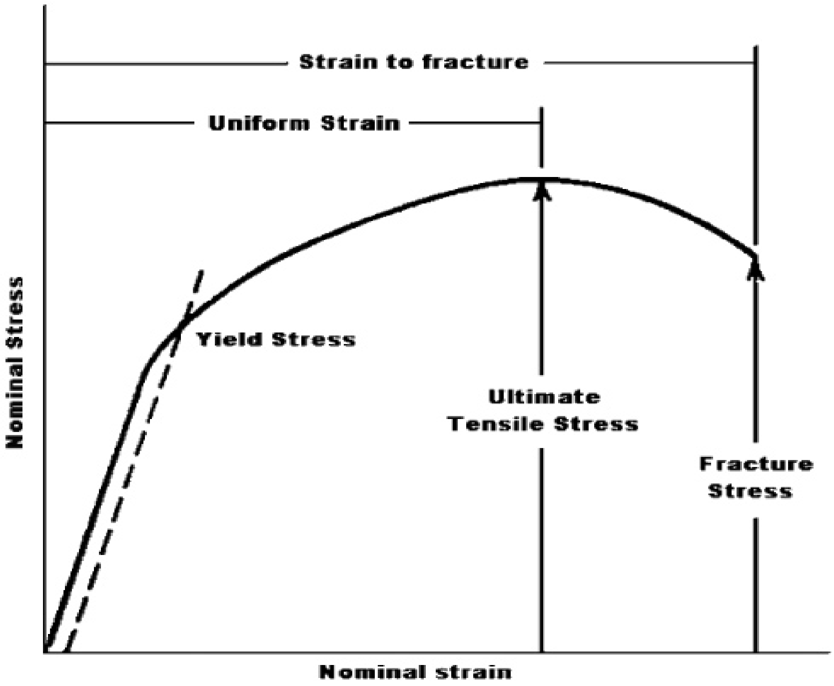

Figure 22: Typical stress-strain behavior under tensile loading [35].

Now consider viscoplastic deformation of a metallic material. It is clear that the viscoplastic deformation starts when the applied stress reaches a threshold (i.e., subsequent yield stress). Thus, the difference between the applied stress and the threshold can be express as:

$$\sigma_V = \sigma - (\sigma_Y + R + A), \tag{73}$$

where σ_V is the viscous stress. The yield function for the viscoplastic deformation can be expressed as:

$$f = |\,\sigma - A\,| - R - \sigma_Y = \sigma_V\,. \tag{74}$$

For the damaged material, it can be expressed by replacing the stress σ by the effective stress $\tilde{\sigma}$:

$$\tilde{f} = |\,\tilde{\sigma} - A\,| - R - \sigma_Y = \sigma_V\,. \tag{75}$$

By employing the Norton law, creep rate or viscous strain rate $\dot{\varepsilon^v}$ can be defined as:

$$\dot{\varepsilon}^v = \left(\frac{\sigma_V}{K_V}\right)^n \tag{76a}$$

$$\dot{\varepsilon}^v = ln\left(1 - \frac{\sigma_V}{K_\infty}\right)^{-N}, \tag{76b}$$

where n, K_V and N, K_∞ are material constants. Also, the viscoplastic constitutive equations of the damaged material in uniaxial state of stress can be expressed as:

$$\dot{\varepsilon}^{vp} = \Big(\frac{\tilde{f}}{K_V}\Big)^n \tag{77a}$$

$$\dot{\varepsilon}^{vp} = ln\Big(1 - \frac{\tilde{f}}{K_\infty}\Big)^{-N}, \tag{77b}$$

where Eqs. (76b) and (77b) are the alternative logarithmic laws.

2.7.3 3D Inelastic Constitutive Equations

In this section, by using thermodynamic constitutive theory and the 1D inelastic constitutive equations, 3D inelastic constitutive equations will be derived. Considering a small deformation, the total strain ε is divided into the elastic ε^e and the plastic ε^p part:

$$\varepsilon = \varepsilon^e + \varepsilon^p\,. \tag{78}$$

According to the principle of local state, a non-equilibrium process in a continuum can be described by the process of change in its state variables. In the case of strain hardening in 3D deformation, the thermodynamic state is described by the strain ε and the temperature T. The scalar damage variable D can be utilized assuming the isotropy of damage. Along with strain and temperature, strain hardening is accompanied by the associated variables of isotropic hardening r and kinematic hardening α. Thus, the Helmholtz free energy can be expressed as:

$$\Psi = \Psi(\varepsilon^e, T, r, \alpha, D)\,. \tag{79}$$

Substituting Eqs. (78) and (79) in Clasius-Duhem inequality (Eq. (69)) gives:

$$\Big(\sigma - \rho\frac{\partial\Psi}{\partial\varepsilon^e}\Big) : \dot{\varepsilon}^e - \rho\Big(s + \frac{\partial\Psi}{\partial T}\Big)\dot{T} + \sigma : \dot{\varepsilon}^p - \rho\frac{\partial\Psi}{\partial r}\dot{r} - \rho\frac{\partial\Psi}{\partial\alpha}\dot{\alpha} - \rho\frac{\partial\Psi}{\partial D}\dot{D} - \frac{\mathrm{grad}T}{T}.q \geq 0\,, \tag{80}$$

which must be satisfied for every thermodynamic process [1]. Now, considering first event of elastic deformation in a uniform temperature field. As the internal state remains unchanged, thus:

$$\mathrm{grad}T = 0,\ \dot{\varepsilon}^p = 0,\ r = 0,\ \alpha = 0,\ \text{and}\ D = 0. \tag{81}$$

Thus, the Eq. (80) gives:

$$\Big(\sigma - \rho\frac{\partial\Psi}{\partial\varepsilon^e}\Big) : \dot{\varepsilon}^e - \rho\Big(s + \frac{\partial\Psi}{\partial T}\Big)\dot{T} \geq 0\,. \tag{82}$$

For any choice of $\dot{\varepsilon}^e$ and T, this inequality should be satisfied. Implementing this requirement gives the following state equations:

$$\sigma = \rho\frac{\partial\Psi}{\partial\varepsilon^e}\,, \qquad s = -\frac{\partial\Psi}{\partial T}\,. \tag{83}$$

Using the above relation, Eq. (80) becomes:

$$\sigma : \dot{\varepsilon}^p - \rho \frac{\partial \Psi}{\partial r} \dot{r} - \rho \frac{\partial \Psi}{\partial \alpha} : \dot{\alpha} - \rho \frac{\partial \Psi}{\partial D} \dot{D} - \frac{\text{grad}T}{T} . q \geq 0 \, . \tag{84}$$

Now the associated variables with internal variables r, α, D and q can be defined as:

$$R \equiv \rho \frac{\partial \Psi}{\partial r}, \quad A \equiv \rho \frac{\partial \Psi}{\partial \alpha}, \quad Y \equiv -\rho \frac{\partial \Psi}{\partial D}, \quad g \equiv -\text{grad}T \, . \tag{85}$$

Considering Eqs. (84) and (85), the Clausis-Duhem inequality (Eq. (69)) can be rewritten as:

$$\Phi = \sigma : \dot{\varepsilon}^p - R\dot{r} - A : \dot{\alpha} + Y\dot{D} + (g/T).q \geq 0 \, . \tag{86}$$

Eq. (86) gives the dissipation Φ, where the internal and their associated variables are expressed as a product. It can be seen that the product contains a generalized force vector and a generalized flux vector. As a convention, the force causes the flux. Thus, the generalized force vector X and the generalized flux vector J in considered case will be:

$$X \equiv (\sigma, -R, -A, Y, g/T) \tag{87a}$$

$$J \equiv (\dot{\varepsilon}^p, \dot{r}, \dot{\alpha}, \dot{D}, q) \, . \tag{87b}$$

Then, a compact form of the Eq. (86) can be written as:

$$\Phi = X.J \geq 0 \, . \tag{88}$$

A potential distribution function in the case on considered internal and their associated variables can be defined as:

$$F(X) = F(\sigma, R, A, Y, g/T; \varepsilon^p, r, \alpha, D, T) \, . \tag{89}$$

According to Rice [36], the evolution equations of the flux vector J can be described as a function of the force vector F as follows:

$$J = \dot{\Lambda} \frac{\partial F}{\partial X} \, , \tag{90}$$

where $\dot{\Lambda}$ is an indeterminate multiplier.
Conclusively, the relations can be deduced from the Eq. (90) as follows:

$$\dot{\varepsilon}^p = \dot{\Lambda} \frac{\partial F}{\partial \sigma}, \quad \dot{r} = -\dot{\Lambda} \frac{\partial F}{\partial R}, \quad \dot{\alpha} = -\dot{\Lambda} \frac{\partial F}{\partial A}, \quad \dot{D} = \dot{\Lambda} \frac{\partial F}{\partial Y}, \quad q = \dot{\Lambda} \frac{\partial F}{\partial (g/T)} \, . \tag{91}$$

The dissipation potential function is distributed into potential due to plastic deformation, strain-hardening and damage. The dissipation potential due to damage is dependent on the strain energy release rate Y, the associated variable of isotropic hardening r, and on the damage D itself [1, 12]. Therefore, the damage dissipation potential can be written as:

$$F^D = F^D(Y, r, D). \tag{92}$$

Lemaitre [12] formulated the following damage dissipation potential and damage evolution equation by examining the ductile and brittle damage from micromechanics point of view:

$$F^D = \frac{S}{(s+1)(1-D)}\left(\frac{Y}{S}\right)^{s+1} \tag{93a}$$

$$\dot{D} = \dot{\Lambda}\frac{\partial F^D}{\partial Y} = \left(\frac{Y}{S}\right)^{s}\dot{p}H(p-p_D), \tag{93b}$$

where s and S are material constants, p_D is the threshold value for damage initiation, $\dot{\Lambda} = \dot{r} = \dot{p}(1-D)$ and H denotes the Heaviside function which means that the evolution equation is valid when $p > p_D$. Also, the initiation of a crack is assumed to occur when the damage variable D attains a critical value, i.e., $D = D_{crit}$.
Rest of the evolution and constitutive equations can be expressed as [1]:

$$\varepsilon^e_{ij} = \frac{1+\nu}{E}\frac{\sigma_{ij}}{1-D} - \frac{\nu}{E}\frac{\sigma_{kk}}{1-D}\delta_{ij}, \tag{94a}$$

$$\dot{\varepsilon}^p_{ij} = \frac{3}{2}\frac{\tilde{\sigma}^D_{ij} - A^D_{ij}}{(\tilde{\sigma} - A)_{EQ}}\frac{1}{1-D}\dot{\Lambda}, \tag{94b}$$

$$\dot{r} = \dot{\Lambda} = \dot{p}(1-D), \tag{94c}$$

$$\dot{\alpha}_{ij} = \varepsilon^p_{ij}(1-D) - \frac{3}{2A_\infty}A^D_{ij}\dot{\Lambda}, \tag{94d}$$

$$R = R_\infty(1 - \exp^{-br}), \tag{94e}$$

$$A^D_{ij} = \frac{2}{3}A_\infty c\alpha^D_{ij}, \tag{94f}$$

where $()^D$ denotes the deviatoric part, $()_{kk}$ is the trace of a matrix and b & c are constants.

2.7.4 Equations for Isotropic von Mises Plasticity

In service conditions, the components being often utilized must bear complex or multiaxial loadings. The concept of yielding or yield stress is simple to understand in the uniaxial case, but for multiaxial loadings, it is not straightforward. Thus, equivalent von Mises stress or equivalent stress is formulated to model the cumulative effect of multiaxial stresses for yielding. For a material under multiaxial loading, yielding occurs when stress value is above the equivalent stress. It is defined as [37]:

$$\sigma_{EQ} = \sqrt{\frac{3}{2}\sigma^D_{ij}\sigma^D_{ij}}, \tag{95}$$

where σ_{ij}^{D} is a component of the stress deviator tensor, also the called the deviatoric stress tensor [37]. It is a part of the stress tensor which tends to distort the material. It can be defined as:

$$\sigma_{ij}^{D} = \sigma_{ij} - \frac{1}{3}\sigma_{kk}\delta_{ij}, \tag{96}$$

where the second term on the right-hand side in Eq. (96) is called the hydrostatic stress, which causes the change in volume of the material, whereas σ_{kk} is the trace of the stress tensor. For uniaxial state of stress, the principal deviatoric stresses are written as [34]:

$$\sigma_{11}^{D} = \frac{2}{3}\sigma_{11}, \quad \sigma_{22}^{D} = -\frac{1}{3}\sigma_{11}, \quad \sigma_{33}^{D} = -\frac{1}{3}\sigma_{11}. \tag{97}$$

Therefore, using Eq. (95) and the values from Eq. (97), it is clear that for uniaxial loading condition, the equivalent stress is equal to the magnitude of the uniaxial stress, i.e., $\sigma_{EQ} = |\sigma_{11}|$.

The equivalent plastic strain in this approach is defined as [1]:

$$p(t) = \int_0^t \dot{p}(\tau)\,\mathrm{d}\tau. \tag{98}$$

Also, the equivalent plastic strain rate can be written as:

$$\dot{p} = \sqrt{\frac{2}{3}\dot{\varepsilon}_{ij}^{p}\dot{\varepsilon}_{ij}^{p}}. \tag{99}$$

For uniaxial state of stress assuming incompressibility, the components of the equivalent plastic strain rate can be expressed as:

$$\dot{\varepsilon}_{11}^{p} = \dot{\varepsilon}, \quad \dot{\varepsilon}_{22}^{p} = -\frac{1}{2}\dot{\varepsilon}, \quad \dot{\varepsilon}_{33}^{p} = -\frac{1}{2}\dot{\varepsilon}. \tag{100}$$

Thus, using Eq. (99) and the values from Eq. (100), it is plausible that the multi-dimensional strain reduces to one-dimensional plastic strain rate and thus is equal to the plastic strain rate, i.e., $\dot{p} = |\dot{\varepsilon}^{p}|$. The equations of this section are later used for the calculation of multi-axial fatigue damage.

2.7.5 Plastic Strain Threshold for Damage and Strain Energy Release Rate

The threshold value of plastic strain for damage p_D of Eq. (93b) is the value of plastic strain required to initiate the damage and is dependent on the type of loading. For uniaxial loading, its low or several percents but for multi-axial loading, it can be as high as several hundred percents [1]. There is no defined method of calculating the value of p_D, however, in the case of multi-axial fatigue damage, Sermage et al. [13] have determined it. The mathematical relation of p_D for fatigue damage initiation is expressed as:

$$p_D = \varepsilon_D^{p}\left(\frac{\sigma_U - \sigma_Y}{\sigma_{EQ}^{max} - \sigma_Y}\right)^{\zeta}, \tag{101}$$

where ζ is a material constant and ε_D^p is the threshold value of plastic strain in case of pure tension taken as a reference. Later, Eq. (101) will be modified to model not only fatigue but also creep damage.

In section 2.7.3, the generalized force vectors which are the cause of generalized flux vectors are discussed. It is quite clear that the variable Y also called strain energy release rate, is the force that causes damage as shown in Eq. (85). It is shown as the partial derivative of the Helmholtz free energy Ψ with respect to the damage D. The Helmholtz free energy of the damaged material is given as [1]:

$$\rho\Psi^E(\varepsilon^e, D) = \frac{1}{2} C_{ijkl}\varepsilon_{ij}^e \varepsilon_{kl}^e (1-D), \tag{102}$$

where $\rho\Psi^E(\varepsilon^e, D)$ denotes the elastic strain energy affected by damage. Therefore, the strain energy release rate then can be deduced by using Eq. (85) as follows:

$$Y = -\rho\frac{\partial \Psi^E}{\partial D} = \frac{1}{2} C_{ijkl}\varepsilon_{ij}^e \varepsilon_{kl}^e . \tag{103}$$

Understanding the physical significance of the strain energy release rate associated with damage, Chaboche [38] devised a relation for Y, which is expressed as:

$$Y = \frac{W^E}{(1-D)}, \tag{104}$$

where W^E is the elastic strain energy per unit volume. It is deducible from Eq. (104) that Y increases with increases in W^E and D. Assuming the case of constant stress, the Eq. (104) is modified into the following relation:

$$Y = \frac{1}{2}\left(\frac{\partial W^E}{\partial D}\right)_{\sigma=const.} . \tag{105}$$

Observing Eq. (105) implies that Y is the release rate of elastic strain energy due to the damage development, therefore it is also called strain energy density release rate. Consider a damage state A as shown in Fig. 23 on a stress-strain curve under tensile loading. To attain a state B, it is presumed that damage develops by dD under the condition of $\sigma = const.$ and the elastic strain rises by $d\varepsilon^e$. Thus, the triangle $\triangle ABC$ represents the release rate of strain energy $Y\mathrm{d}D$, which implies that Y is the strain energy release rate due to damage development.

As discussed earlier, the crack initiates when the damage value attains to a critical value. According to this notion, fracture criterion of the damaged material is fulfilled when Y achieves a critical value, i.e., $Y = Y_C$.

Eq. (104) defines Y for uniaxial case. For multiaxial state of stress, Y can be represented in an alternative form as [1]:

$$Y = \frac{\tilde{\sigma}_{EQ}^2}{2E}\left[\frac{2}{3}(1+\nu) + 3(1-2\nu)\left(\frac{\sigma_H}{\sigma_{EQ}}\right)^2\right], \tag{106}$$

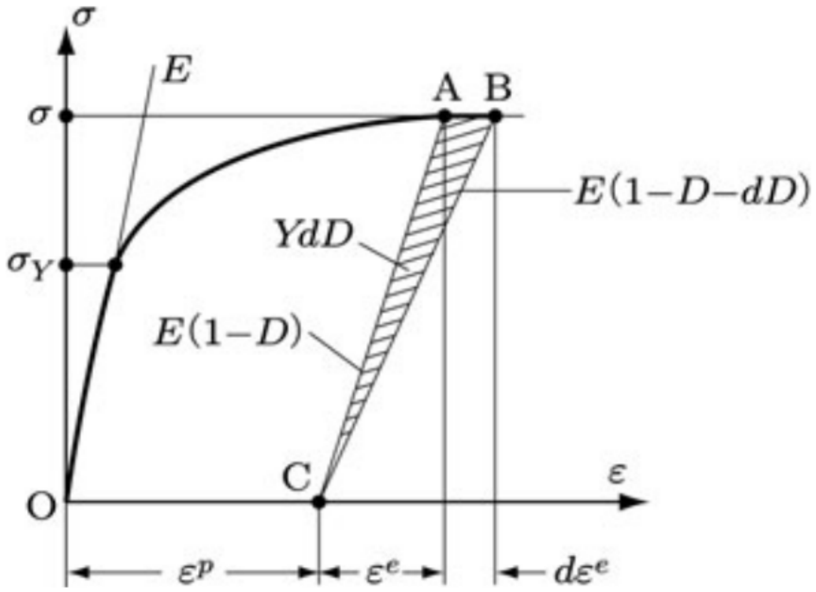

Figure 23: Illustration of strain energy release rate due to damage [1].

where σ_H/σ_{EQ} is the stress triaxiality ratio. It is an essential quantity which determines the mode of fracture. The higher the value of stress triaxility, the more brittle is the fracture [1]. The term inside the square brackets in Eq. (106) is expressed as:

$$R_\nu \equiv \frac{2}{3}(1+\nu)+3(1-2\nu)\left(\frac{\sigma_H}{\sigma_{EQ}}\right)^2, \tag{107}$$

and is called the stress triaxiality function.

2.8 Multiaxial Fatigue Damage Model

Sermage et al. [13] suggested that the elastic-plastic constitutive and evolution equations that were proposed by Lemaitre [12] under the assumption of the hypothesis of strain equivalence can also be employed to model the multiaxial fatigue damage. He also showed that uncoupled analysis can provide fairly good results. On the other hand, fully coupled analysis take much time and computation but the results are much better.

For the evolution of fatigue damage, the evolution equations as mentioned in Sec. 2.7.3 are utilized in this model.

$$\begin{aligned} \dot{D} &= \left(\frac{Y}{S}\right)^s \dot{p} \qquad if\, p > p_D\,, \\ \dot{D} &= 0 \qquad if\, p < p_D\,, \end{aligned} \tag{108}$$

where p_D is the threshold value of the accumulated plastic strain for damage. In the case of uniaxial test, $p_D = \varepsilon_D^p$. Moreover, damage initiates when damage value attains a critical value, i.e., $D = D_{crit}$.

The values calculated for p_D through Eq. (101) has notable difference than the measured values from the experiment. To get rid of this irregularity, the rate of the stored energy in the material is supposed as:

$$\dot{W}_s = (\sigma_{EQ} - \sigma_Y)\,\dot{p}\,. \tag{109}$$

The value $\mathrm{d}W_s/\mathrm{d}p$ becomes neglible as p increases. Thus, Eq. (109) can be improved as:

$$\dot{W}_s = (\sigma_{EQ} - \sigma_Y)\,\frac{\varepsilon_D^p}{\varepsilon_D^p + p_D}\,\dot{p}\,. \tag{110}$$

Integrating above equation from $p = 0$ to $p = p_D$ and assuming the maximum value of σ_{EQ} for the deformation. Therefore:

$$W_s = (\sigma_{EQ}^{max} - \sigma_Y)\,\varepsilon_D^p\, ln\left(\frac{\varepsilon_D^p + p_D}{\varepsilon_D^p}\right). \tag{111}$$

Considering the simple case of uniaxial (tensile) loading, Eq. (111) becomes:

$$(W_s)_T = (\sigma_U - \sigma_Y)\,\varepsilon_D^p\, ln2\,. \tag{112}$$

Considering the fact that the stored energy for damage initiation for the uniaxial and the multiaxial cases must be same. Therefore, the threshold for damage initiation is:

$$p_D = \varepsilon_D^p\left[exp\left(\frac{\sigma_U - \sigma_Y}{\sigma_{EQ}^{max} - \sigma_Y}\ln 2\right) - 1\right], \tag{113}$$

where ε_D^p is the damage threshold in pure tension.

3 Experiment

To collect the basic data for modeling of the creep-fatigue damage, the specimens were subjected to strain-controlled LCF without hold-times and with hold-times in tension and compression at temperatures 300 °C, 400 °C, 425 °C, 500 °C, 550 °C, 600 °C, and 625 °C respectively. At each temperature, experiments have been performed at the same strain rate but with different strain ranges.

3.1 Materials

The materials utilized for experiments are cast steel with German grade GX12CrMoVNbN9-1 and 30CrMoNiV5-11 respectively. Material properties, such as chemical composition, room temperature properties, and other structural information are taken from [39, 40]. GX12CrMoVNbN9-1 has a typical martensitic microstructure with ferritic sub-grains, whereas 30CrMoNiV5-11 has a ferritic-bainitic microstructure. These materials are identified in this report with the prefixes "BDD" and "BAP" respectively, in the testing program of the Institute of Materials Technology (MPA / IfW), Technische Universität Darmstadt. The provision of these materials are carried out by the industries, such as Siemens, Alstom and MAN & Turbo SE. Chemical composition and the material properties at room temperature of GX12CrMoVNbN9-1 (BDD) are shown in Tables 3 and 4.

Table 3: Chemical composition of GX12CrMoVNbN9-1 (BDD).

C	Cr	Mo	B	Ni	V	Nb	N
0.12	8.90	1.00	0.0004	0.26	0.20	0.061	0.049
Mn	Si	P	S	Cu	Ti	Al	Sn
0.48	0.36	0.011	0.002	0.05	0.014	0.012	0.007

Table 4: Room temperature mechanical properties of of GX12CrMoVNbN9-1 (BDD).

$R_{p0.2}$ (MPa)	R_m (MPa)	A (%)	Z (%)	Hardness (HV30)	A_v (ISO-V) (J)
523	678	20.9	59.6	219	82

Chemical composition and the material properties at room temperature of 30CrMoNiV5-11 (BAP) are shown in Tables 5 and 6.

Table 5: Chemical composition of 30CrMoNiV5-11 (BAP).

C	Si	Mn	P	S	Al	N	Cr	Cu
0.29	0.09	0.74	0.007	0.002	0.005	0.041	1.3	0.14
Mo	Nb	Ni	Ti	V	Sb	Sn	H_2	As
1.02	0.001	0.66	0.0002	0.292	0.0023	0.008	0.00011	0.0116

Table 6: Room temperature mechanical properties of 30CrMoNiV5-11 (BAP).

$R_{p0.2}$ (MPa)	R_m (MPa)	A (%)	Z (%)	Hardness (HV30)	A_v (ISO-V) (J)
604	736	20	69	237	-

Other information, such as heat treatment and the microstructure of the materials can be found in [39, 40].

3.2 Experimental Technique

In the experiments, round specimens are used for both the materials BDD and BAP respectively. Samples utilized for experiments can be seen in Fig. 24. Table 7 shows the geometry of the used sample types.

Table 7: Geometry and specimen type of the samples.

Specimen Type	Sample	Diamter (mm)	Length (mm)
Type-38a	BDD	7.9 ± 0.05	15.5 ± 0.05
Type-37a	BAP	10.00 ± 0.05	19.95 ± 0.05

The tests are carried out at the Institute of Materials Technology (MPA / IfW), Technische Universität Darmstadt. Infrared-radiation furnaces or Three-zone induction furnaces are used to achieve desired temperatures. Temperature measurement is carried out by utilizing high-quality PtRh-Pt-Thermocouples (Type S) according to DIN 43710. The thermocouples are calibrated by an in-house calibration system.

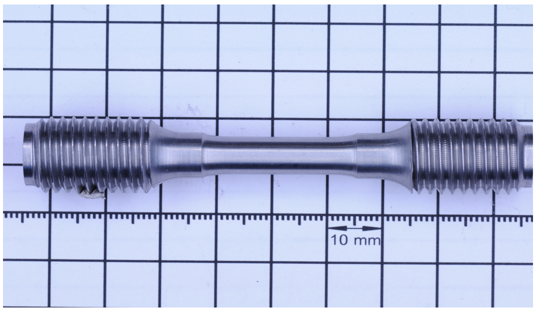

(a) BDD sample.

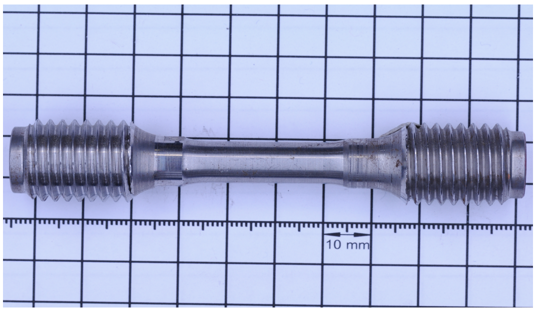

(b) BAP sample.

Figure 24: Samples utilized for LCF experiments.

LCF experiments are carried out according to ISO 12106 employing servo-hydraulic testing machines, which are either equipped with Infrared-radiation furnace or three-zone induction furnace. The straining of the samples is measured by an extensometer with ceramic based meauring rods on the cylindrical part of the sample. The strain rate $\dot{\varepsilon}$ for the experiments without hold-time is 6%/min. Also, for the experiments with hold-time the strain rate for the ramp-up is 6%/min. For the subsequent evolution of damage, the number of cycles to crack initiation N_A is evaluated by using 5% load-drop criterion. At each temperature, different strain ranges $\Delta\varepsilon$ are employed for both cycles types. A typical strain-controlled cycle without hold-time and with hold-time in tension and compression is shown in Fig. 25.

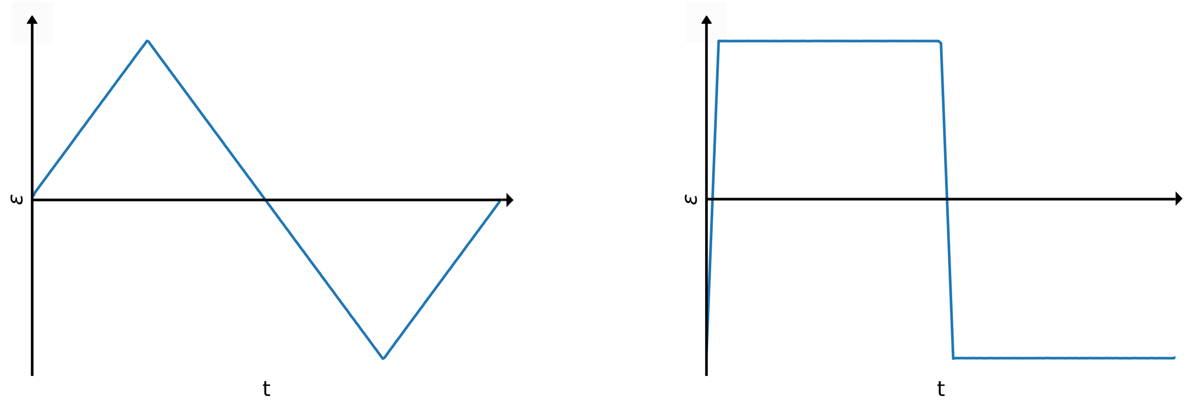

(a) Strain-controlled cycle without hold-time.

(b) Strain-controlled cycle with hold-time in tension and compression.

Figure 25: Cycle types used for default LCF experiments.

3.2.1 Determination of Young's Modulus

As cyclic data is acquired after the LCF experiments, Young's modulus is not acquired directly, which is essential for the evaluation of the damage and the strain energy release rate. A self-made approach is employed to determine Young's modulus as shown in Fig. 26. A tangent is drawn from the 97.5% of the maximum strain to the 87.5% of the maximum strain in tension of the hysteresis loop. Therefore, the slope of the tangent is determined, which is Young's modulus of the sample. This approach is used for all of the experiments and shows good results even for service-type cycles.

3.2.2 Damage Measurement

As mention in Sec. 2.6.2, the damage can be modeled as the variation of Young's Modulus, due to the reduction in stiffness with the development of damage. Young's Modulus for every loop is calculated by the approach mentioned in the previous section. Therefore, the damage is measured by using Eq. (51b). Fig. 27 depicts the measurement of damage.

The measured damage determined initially has an increase and is then constant nearly to the $N_{A5\%}$. As mentioned in Sec. 2.6.2, the initial decrease in Young's modulus or increase in the damage is not truly damage [18], which will be further discussed in the results section (Sec. 4.3). Therefore, a tangent is drawn from 30% of $N_{A5\%}$ to 85% of $N_{A5\%}$ and the difference between the damage and the tangent is calculated and re-plotted to get actual measured damage. D_{crit} is calculated by subtracting the value of damage on the fitted line (dotted black line) from the value of measured damage (blue line) on $N_{A5\%}$.

3.3 Computation

Computational analysis of the raw data has been performed, where the constitutive equations are solved to compute damage and accumulated plastic strain over time. It is the main part of the experimentation, which provided major results. Raw data is received from testing machines in either Comma Separated Value (CSV) files or Data (DAT) files, which is then converted to Extended Markup Language (XML) file through an in-house developed software called wiLDCAT.

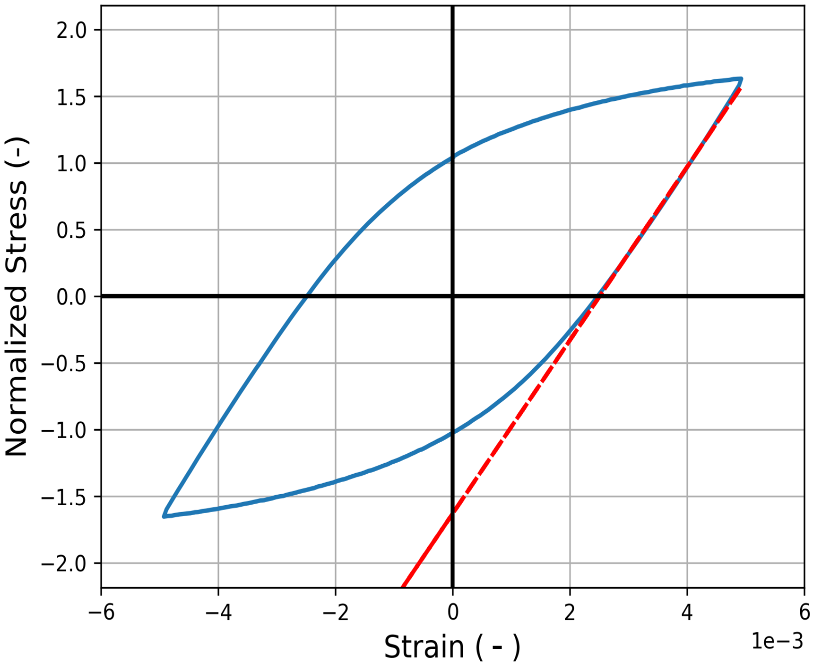

Figure 26: Young’s Modulus determination of sample BDD3d1.

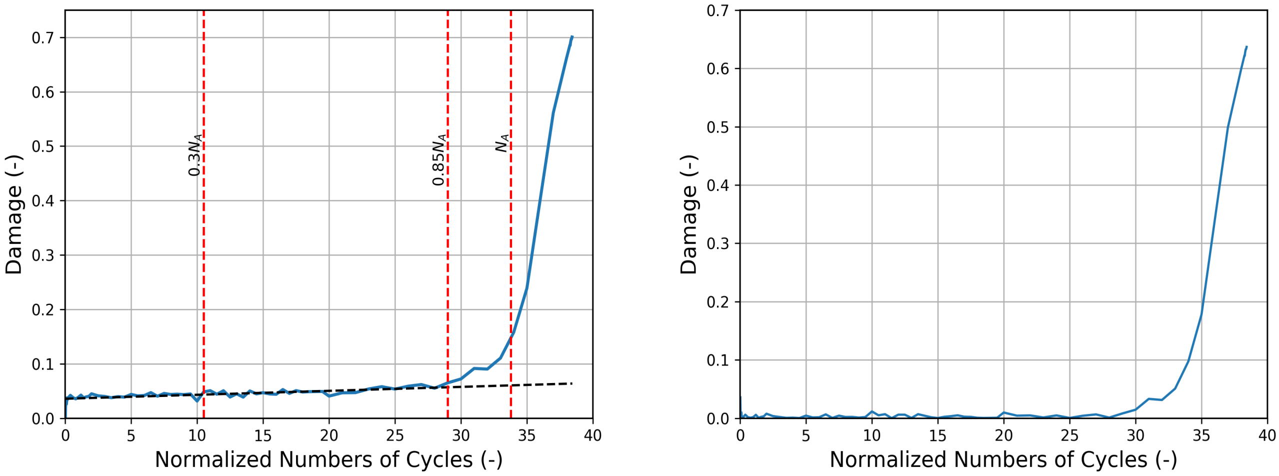

(a) Initial plot.

(b) Corrected Plot.

Figure 27: Determination of the damage.

As the data values are collected after an interval of 25 or 50 cycles and not every cycle, wiLDCAT also provides the ability to interpolate the missing cycles. Due to this interpolation, it is then possible to calculate the damage evolution for each cycle.

3.3.1 Optimization

Optimization (minimization) of the damage evolution Eq. (108) is performed by using the Nelder-Mead and the BFGS algorithm [14, 15]. This algorithm minimizes a provided function for several parameters and returns the value which yields a minimum value of a function. In our case, the distance between the critical damage value and the computed damage value $(D_{crit} - D_{comp})^2$ is minimized for the material parameters s and S respectively. The time required for the minimization depends on the amount of data from the experiment and step size used in the iteration for the solution of damage evolution equation. As the number of experiments and their data is high, for efficiency multiple jobs are submitted simultaneously on different cores of the private server of the Institute of Materials Technology (MPA / IfW), Technische Universität Darmstadt.

The optimization is carried out by using GNU Scientific Library[2] (GSL). SciPy[3] was first employed, but it was observed that some of the experiments containing huge amounts of experimental data were taking too long to be optimized. For instance, BDD3d1 is optimized in 2 seconds using GSL, while with SciPy the optimization took approximately 300 seconds which is around 15000% more.

3.3.2 Damage Evolution

The damage evolution equation is an Ordinary Differential Equation (ODE), which is solved by using the Runge-Kutta Method of fourth-order (RK4) [41] by using a step size of 0.5 seconds and setting the initial damage value to zero. Individual values of the material parameters s and S for respective samples are utilized for the damage evolution. Like the optimization, these computations are also carried out on the in-house server. For accurate calculation, the threshold value of accumulated plastic strain p_D is determined by plotting the measured damage using Eq. (51b) over the calculated accumulated plastic strain p through Eq. (98) using RK4. From the plot, p_D is determined and then the condition $p > p_D$ is included in the damage evolution computation. The strain energy release rate Y is calculated at every time point using Eq. (108). Equations for isotropic von Mises plasticity (Sec. 2.7.4) are used for the calculating the hydrostatic, deviatoric and equivalent stresses.

3.4 Computed Tomography

Computed Tomography (CT) is also performed in the laboratory of the Institute of Materials Technology (MPA / IfW), Technische Universität Darmstadt. CT uses a combination of X-ray measurements of a specimen from different angles to generate a virtual cross-sectional image, which enables one to examine a specimen internally without damaging or cutting. CT data can then directly be imported into analysis and 3D visualization software for examination.

The idea behind to use the CT scans in this work is to calculate the volume of the defects in specimen after LCF experiments and to determine damage. CT data is visualized by using VGSTUDIO MAX, which is then directly analyzed. The software is equipped with defect analysis tool to determine the area, volume and number of defects.

---

[2] `https://www.gnu.org/software/gsl/doc/html/index.html`

[3] `https://www.scipy.org/`

4 Results and Discussion

Let us elaborate the whole process in view of Fig. 28. Before the experimentation, the observation was that the damage depended on the state variables, even on the strain energy density [2–7]. The question arose that whether it is possible to have a damage definition which fulfills certain properties like in-dependency on stress, strain, and Temperature? Also, in-dependency of the damage threshold on the triaxiality of stress. The prediction was made under the concept of CDM for a definition that could fulfill these conditions. Detailed experimentation was performed as mentioned in the previous section. In this section, the results of the experimentation are discussed.

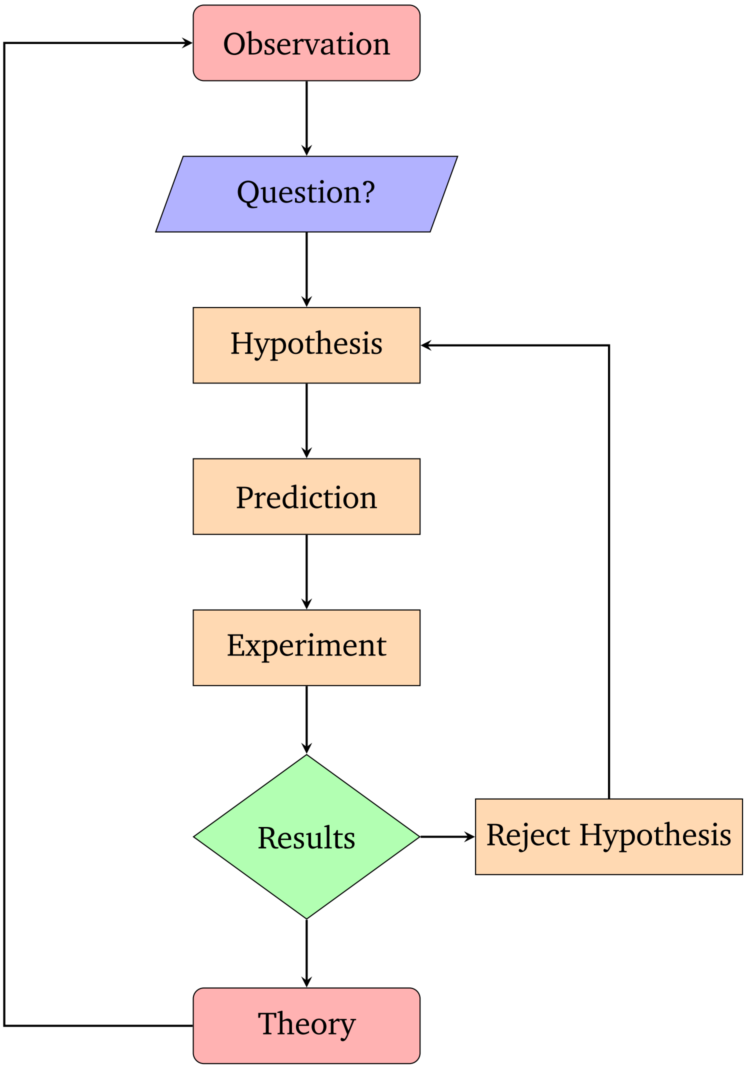

Figure 28: The flow chart of the scientific method.

4.1 Experimental Data

The test conditions for every sample is translated through wiLDCAT and further utilized for computation. Crack positions are observed through a light microscope, and the damage is measured as described previously. Tables 8, 9, and 10 show the test conditions and the results of BDD samples without and with hold-time respectively. Some D_{crit} values are missing in the tables because of missing value in the raw data due to some abnormality as discussed in Sec. 4.3.

Table 8: LCF experiment test conditions and results of BDD samples without hold-time.

Sample	T (°C)	$\dot{\varepsilon}$ (%/min)	$\Delta\varepsilon$ (%)	Crack position (-)	D_{crit} (-)
BDD3d1	300	6	1	inside	0.0871
BDD3d2	300	6	0.5	inside	0.0695
BDD3d3	300	6	0.35	inside	0.0636
BDD425d1	425	6	1	inside	0.0568
BDD425d2	425	6	0.55	inside	0.0511
BDD425d4	425	6	1	inside	-
BDD5d1	500	6	2	inside	0.0328
BDD5d2	500	6	1	inside	0.0342
BDD5d3	500	6	0.5	inside	0.0871
BDD5d4	500	6	0.35	inside	0.1186
BDD5d5	500	6	0.29	inside	0.0925
BDD5d6	500	6	1	inside	0.3489
BDD55d1	550	6	1.2	outside	-
BDD55d2	550	6	0.55	inside	0.0556
BDD55d3	550	6	0.35	inside	0.0139
BDD55d4	550	6	1	inside	0.0555
BDD6d1	600	6	2	inside	0.0172
BDD6d2	600	6	1	inside	0.0939
BDD6d3	600	6	0.55	inside	0.094
BDD6d4	600	6	0.35	inside	0.0979
BDD6d5	600	6	0.29	inside	0.0732
BDD6d6	600	6	0.55	inside	0.0756
BDD6d7	600	6	0.55	inside	0.0889
BDD6d10	600	6	0.55	inside	0.0919
BDD6d11	600	6	0.55	inside	0.0948
BDD6d12	600	6	0.55	inside	0.0584
BDD6d22	600	6	1	inside	0.0506
BDD625d1	625	6	1	inside	0.059
BDD625d2	625	6	0.55	inside	0.0504
BDD625d3	625	6	0.35	inside	0.1095
BDD625d4	625	6	1	inside	0.0789
BDD625d5	625	6	0.55	inside	0.0504

As described in Sec. 2.5.2.1 that $D = 1$ means the fracture of the material, but usually, this value is less than 1, which can also be observed in Table 8. This is due to the instability caused by the sudden decohesion of atoms [18, 24]. Damage progresses approximately smooth until it encounters the critical damage value D_{crit}. When the D_{crit} is reached, CDM is considered as not valid anymore. Fracture mechanics should be used after the crack is initiated. The crack position of the sample is discussed in relation to the variation of Young's modulus in one of the following chapters (Sec. 4.3).

Table 9: LCF experiment test conditions and results of BDD samples with hold-time

Sample	T (°C)	$\dot{\varepsilon}$ (%/min)	$\Delta\varepsilon$ (%)	t_{HZ}/t_{HD} (min)	Crack position (-)	D_{crit} (-)
BDD3dh1	300	6	1	3/3	inside	0.0605
BDD3dh2	300	6	0.55	3/3	inside	0.0137
BDD5dh1	500	6	1	3/3	inside	0.1146
BDD5dh2	500	6	0.55	3/3	inside	-
BDD5dh3	500	6	0.55	3/3	inside	-
BDD5dh4	500	6	0.55	3/3	inside	-
BDD5dh5	500	6	0.35	3/3	outside	0.0915
BDD5dh14	500	6	0.55	10/10	inside	0.0637
BDD6dh1	600	6	0.35	3/3	inside	0.0109
BDD6dh2	600	6	0.55	3/3	outside	-
BDD6dh3	600	6	0.55	3/3	inside	0.0302
BDD6dh4	600	6	0.55	10/10	inside	0.0595
BDD6dh5	600	6	1	10/10	inside	-
BDD6dh6	600	6	0.35	10/10	inside	0.057
BDD6dh7	600	6	0.55	10/10	inside	0.0694
BDD6dh10	600	6	1	3/3	inside	0.0556
BDD6dh11	600	6	1	3/3	inside	0.1172
BDD6dh12	600	6	0.35	3/3	outside	-
BDD6dh13	600	6	0.55	3/3	inside	0.1165
BDD6dh14	600	6	0.55	3/3	inside	0.0496
BDD6dh15	600	6	0.53	10/10	inside	-
BDD6dh19	600	6	1	4.5/8.5	inside	-
BDD6dh20	600	6	1	4.5/8.5	inside	0.0567
BDD625dh2	625	6	0.55	3/3	inside	0.141

Table 10: LCF experiment test conditions and results of BAP samples without hold-time.

Sample	T (°C)	$\dot{\varepsilon}$ (%/min)	$\Delta\varepsilon$ (%)	Crack position (-)	D_{crit} (-)
BAP5d1	500	6	1	inside	0.1917
BAP5d2	500	6	0.67	inside	-
BAP5d3	500	6	0.5	inside	0.0472
BAP5d4	500	6	0.41	inside	0.1379
BAP525d1	525	6	0.73	inside	-
BAP525d2	525	6	0.53	inside	0.0185
BAP525d3	525	6	0.47	inside	-
BAP525d4	525	6	0.4	inside	-

4.1.1 Critical Damage

As shown in Fig. 26, D_{crit} value is measured, firstly, by plotting the linear fit of the number of cycles from 35% to 85%, below which there exists no damage. Secondly, the damage value on the fitted line at $N_{A5\%}$ is subtracted from the measured damage value at $N_{A5\%}$. Thus, D_{crit} is acquired. This procedure is performed for all of the experiments. Fig. 29 shows the linear fit of the critical damage D_{crit} value of all BDD samples at different temperatures. The observed value of D_{crit} is 0.075, which is further utilized as a reference value for optimizing the material parameter S.

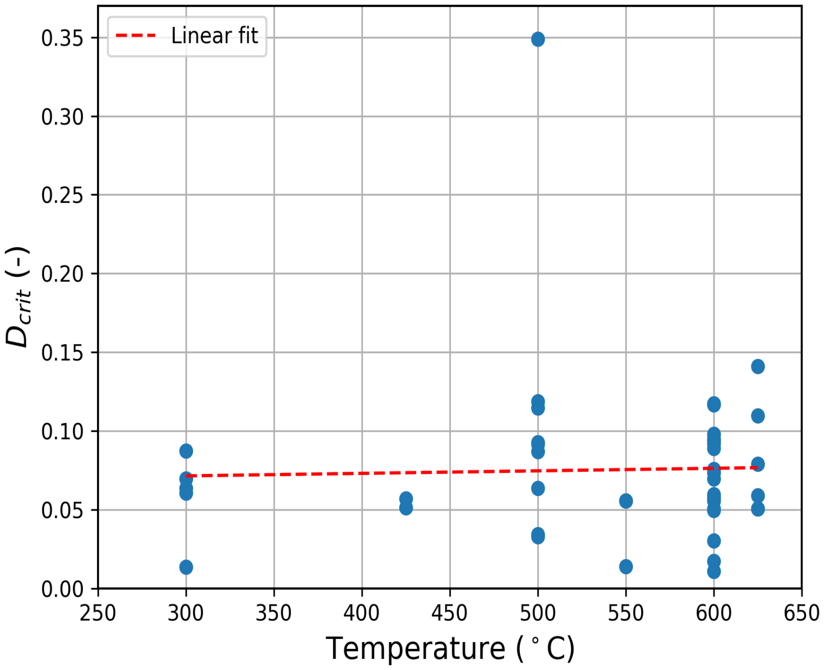

Figure 29: Linear fit of the critical damage of all BDD samples at different temperatures.

It can be observed from Fig 29 that D_{crit} is scattered over the plot. Therefore, a linear fit is drawn to show the average value of D_{crit} over different range of temperatures. The linear fit has almost a slope of zero and thus, we can say that the D_{crit} of BDD is almost same over different ranges of temperature. Also, only one value which seem to be very high compared to others (0.35 at 500 °C) is of BDD5d6, which is due to some irregularity in the sample's behavior which will be discussed in Section 4.3. Fig. 30 shows the D_{crit} value over different strain ranges.

Again, it can be seen from Fig. 30 that there is no trend observed in the value of D_{crit} with the strain range. Also, the linear fit shows minimal slope and the average value is 0.075. Therefore, it is claimed that D_{crit} is a material property, independent of temperature and stress-triaxiality.

4.2 LCF Behavior

4.2.1 Hysteresis Loop

Fig. 31 shows the comparison of the hysteresis loops of samples without and with hold-time at 300 °C and 600 °C. All of these samples have been deformed at a strain range $\Delta\varepsilon = 1\%$.

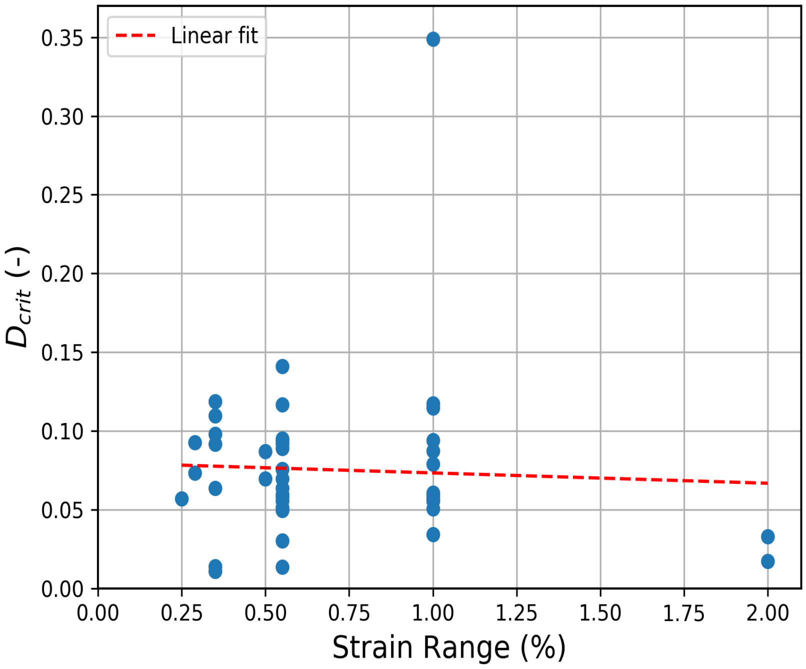

Figure 30: Linear fit of the critical damage of all BDD samples at different strain ranges.

The hysteresis behavior of BDD3d1 and BDD3dh1 is almost same apart from the hold-time. The stress and strain response is almost the same. Similar is the case for BDD6d2 and BDD6dh10. Considering BDD3d1 and BDD6d2 or BDD3dh1 and BDD6dh10, the difference is the amount of stress required to produce approximately similar strain. The stress required for samples at 600 °C is around 35% less, which can be due to the enhanced movement of dislocations at high temperatures [42] due to the thermal activation. Less stress, therefore, is needed for the movement of dislocations leading to decrease in the flow stress.

4.2.2 Load-Drop Curves

Fig. 32 shows the comparison of the load-drop curves (with normalized stress) of samples without and with hold-time at 300 °C and 600 °C. All of these samples have been deformed at a strain range $\Delta\varepsilon = 1\%$.

The number of cycles to crack initiation $N_{A5\%}$ at a load drop of 5% obtained for BDD3d1 and BDD3dh1 are different, with $N_{A5\%}$ of BDD3dh1 being lower. The reason is that BDD3d1 is deformed at a constant cycle whereas BDD3dh1 is deformed at a cycle with holds in tension and compression both, which clearly reduces the lifetime. In Cr-Mo steels, slight hardening followed by softening of the material is observed at moderate temperatures and low strain rates [43], which probably reduces the number of cycles to crack initiation and ultimately the number of cycles to failure.

On the other hand, $N_{A5\%}$ for BDD6d2 and BDD6dh10 has similar behavior to each other, but in comparison to BDD3d1 and BDD3dh2, $N_{A5\%}$ is reduced even more because of the high temperature. At high temperatures and low strain rates for Cr-Mo steels, continuous softening is observed [43], which is the reason for the sample breaking at less number of cycles.

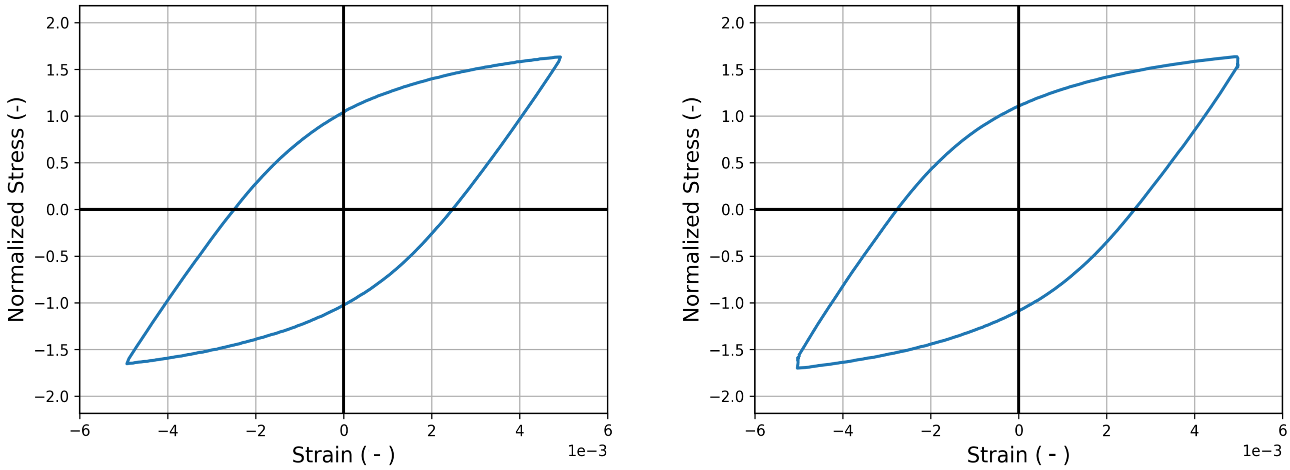

(a) BDD3d1 **(b)** BDD3dh1

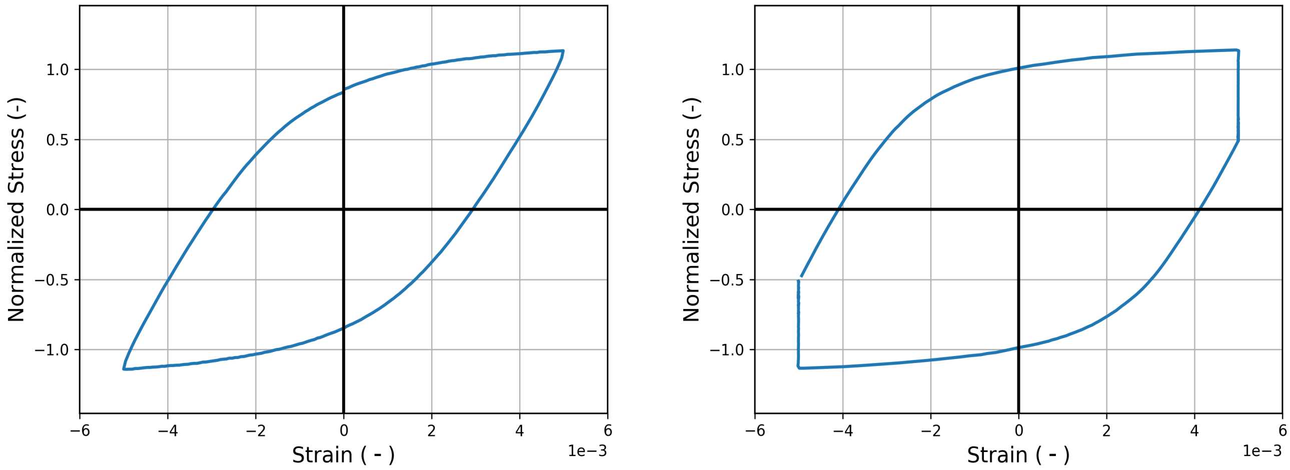

(c) BDD6d2 **(d)** BDD6dh10

Figure 31: Hysteresis loop of samples without and with hold-times at 300 °C and 600 °C.

4.2.3 Damage Threshold

The damage threshold p_D in the utilized damage model is criteria for damage to have a value or not. Therefore, its determination is necessary for implementing the model itself. The accumulated plastic strain p is calculated using Eq. (98). Fig. 33 shows the determination of damage threshold by plotting the measured damage over number of cycles.

Measured damage is calculated by using Eq. (51b) and is then interpolated over number of cycles and finally plotted against accumulated plastic strain p. It is clear from Fig. 33 that there is a sudden increment at about a value of $p = 13.5$ and afterwards it continues to shoot. So it can be easily concluded, that 13.5 is the value for the sample at which a crack continues to grow until fracture. Therefore, it is called the damage threshold. Tables A1, A2, and A3 show the value of p_D determined for BDD and BAP samples without hold-time and BDD samples with hold-time.

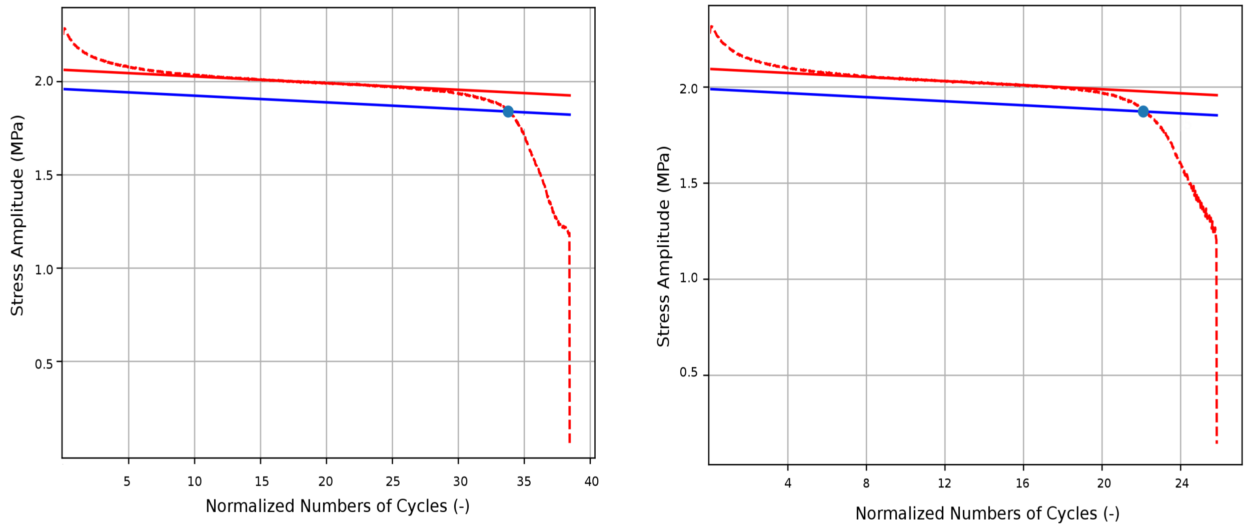

(a) BDD3d1

(b) BDD3dh1

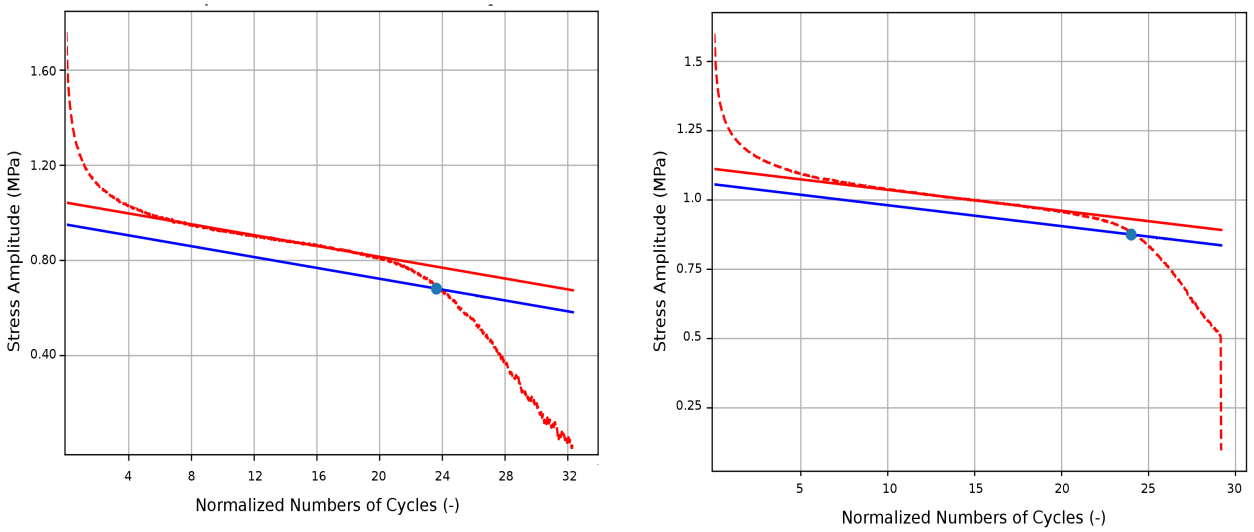

(c) BDD6d2

(d) BDD6dh10

Figure 32: Load-Drop curves (with normalized stress) of samples without and with hold-times at 300 °C and 600 °C.

Figure 34 shows the damage threshold values of BDD samples without hold-time at different temperatures. A clear dependence of p_D can be seen on the strain range $\Delta\varepsilon$. It can be seen that with increasing $\Delta\varepsilon$, the p_D value tends to decrease. The lowest being 3 for 2% $\Delta\varepsilon$ and the highest being 60 for 0.29% $\Delta\varepsilon$. However, for same $\Delta\varepsilon$, the p_D value for different temperatures does not vary greatly except for the 0.29% $\Delta\varepsilon$. There is no regular trend for values increasing with increasing temperature at the same $\Delta\varepsilon$.

Figure 35 shows the damage threshold values of BDD samples with hold-time at different temperatures. In this case also, the general trend shows decrease of p_D with increasing strain range. Also, the values of p_D are in the similar range for similar $\Delta\varepsilon$. Apart from the points at 1% $\Delta\varepsilon$, there seems a variation of points from 0.55% and 0.35% $\Delta\varepsilon$. Therefore, hold-times and temperature seem to have no or little effect on p_D, but $\Delta\varepsilon$ does have an effect.

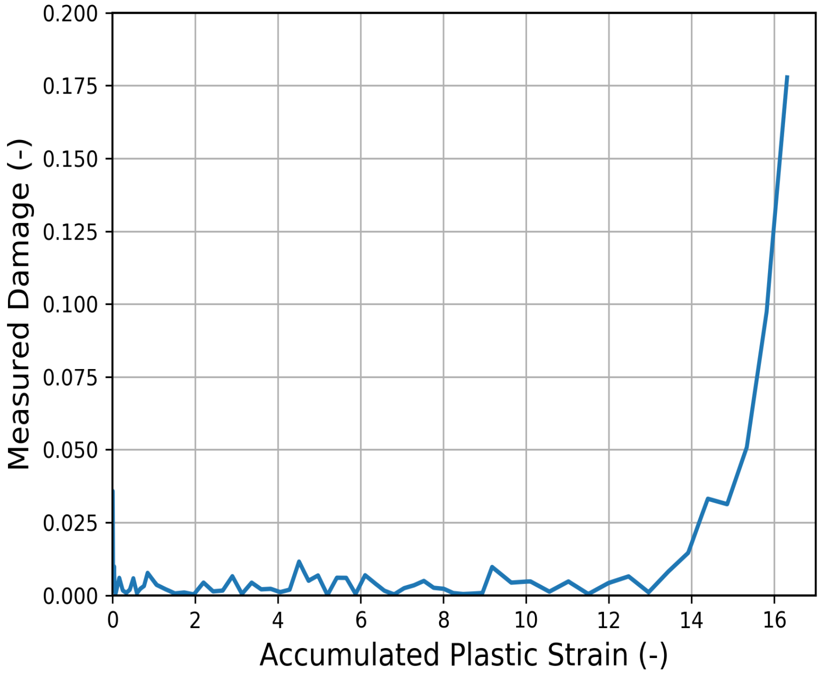

Figure 33: Determination of p_D for BDD3d1.

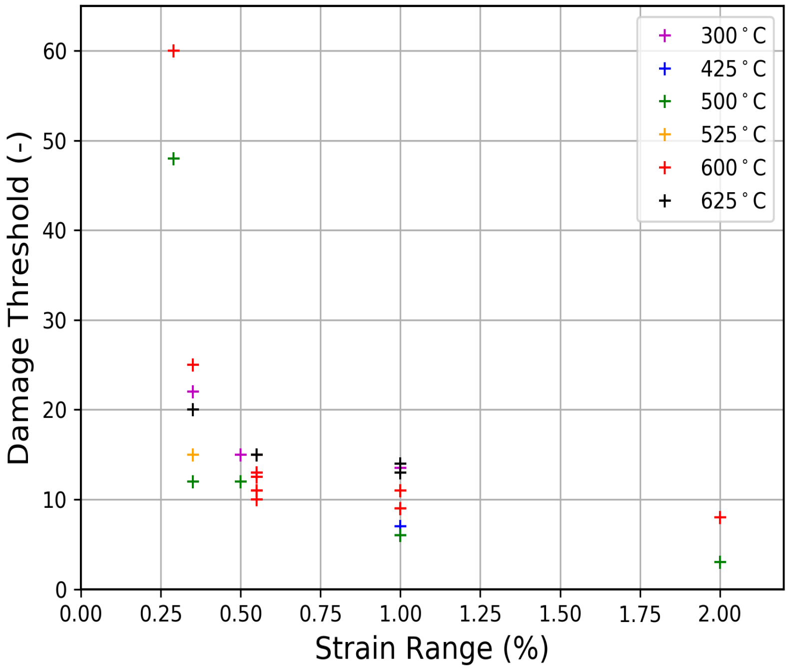

Figure 34: Damage threshold of BDD samples without hold-time for different temperatures.

4.2.4 Plastic Hysteresis Energy Density

Fig. 36 shows the comparison of the plastic hysteresis energy density of samples without and with hold-time at 300 °C and 600 °C. All of these samples have been deformed at a strain range $\Delta\varepsilon = 1\%$.

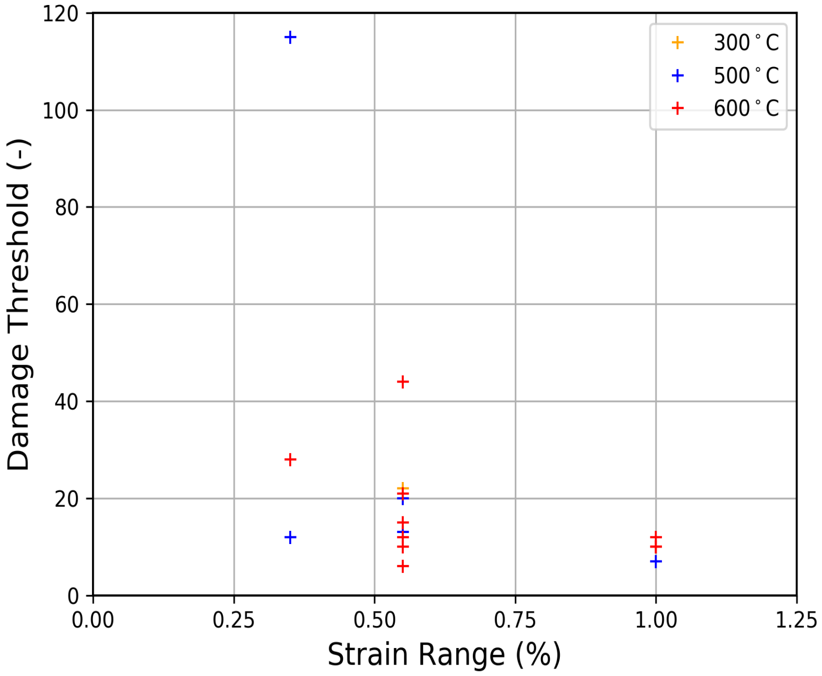

Figure 35: Damage threshold of BDD samples with hold-time for different temperatures.

The plastic hysteresis energy per cycle is the area of the hysteresis loop [44] and does not vary a great deal with cycles for strain-controlled tests. It can be observed from Fig. 36 that at the same temperature, more energy is stored in the samples with hold-time. It can also be verified from Fig. 31, that hysteresis loop of the samples with hold-time has a larger area than that of the samples without hold-time. However, for samples at the higher temperature, the energy density is lower compared to the samples at the lower temperature. Also, their overall accumulated density is lower than the samples at the lower temperature, which can be due to the lower value of stress required to deform the samples at the higher temperature. Moreover, samples at 600 °C, tends to deform at a rate slightly faster than at 300 °C. An initial drop can be observed in the samples at 600 °C, which is due to the reduction of stiffness (Fig. 38c and 38d). However, the sharp decrease in BDD3dh1 is due to an interpolation error.

4.2.5 Strain Energy Release Rate

Fig. 37 shows the comparison of the strain energy release rate Y of samples without and with hold-time at 300 °C and 600 °C. All of these samples have been deformed at a strain range $\Delta\varepsilon = 1\%$. For plotting, the strain is interpolated over time first and then plotted against Y.

Starting from the centre, the strain energy release rate Y increases in tension up to the maximum strain and starts to decrease with stress relaxation. It again increases in compression up to the minimum strain and the cycle goes on. It can be observed from Fig. 37 that Y is similar in behavior to the plastic hysteresis energy density. It is slightly higher in magnitude in tension and compression with hold-time than the samples without hold-time at both high and low temperatures. Again, it can be verified from the hysteresis loops in Fig. 31. Moreover, samples at a

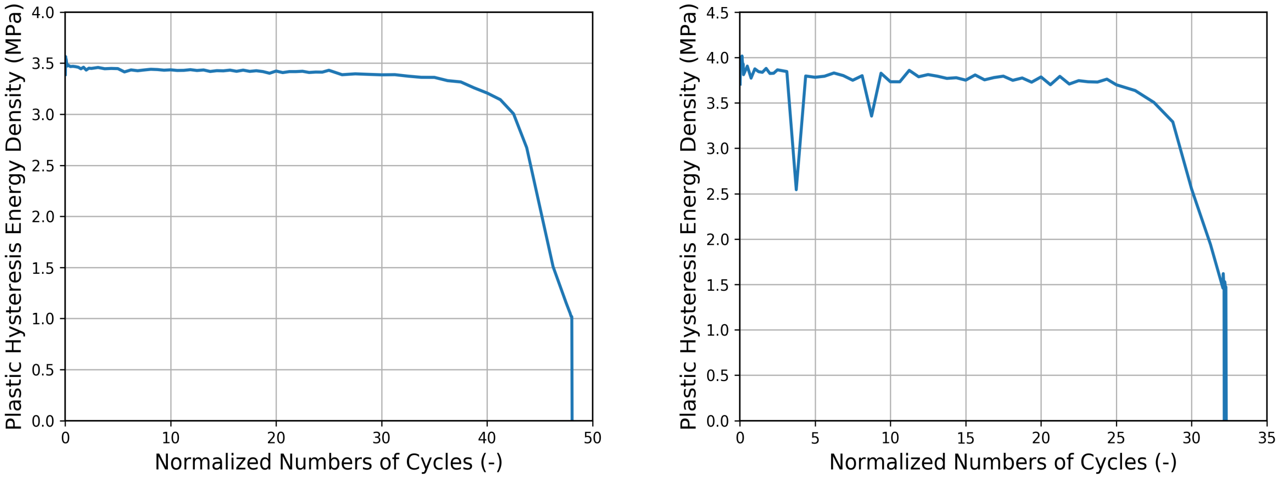

(a) BDD3d1

(b) BDD3dh1

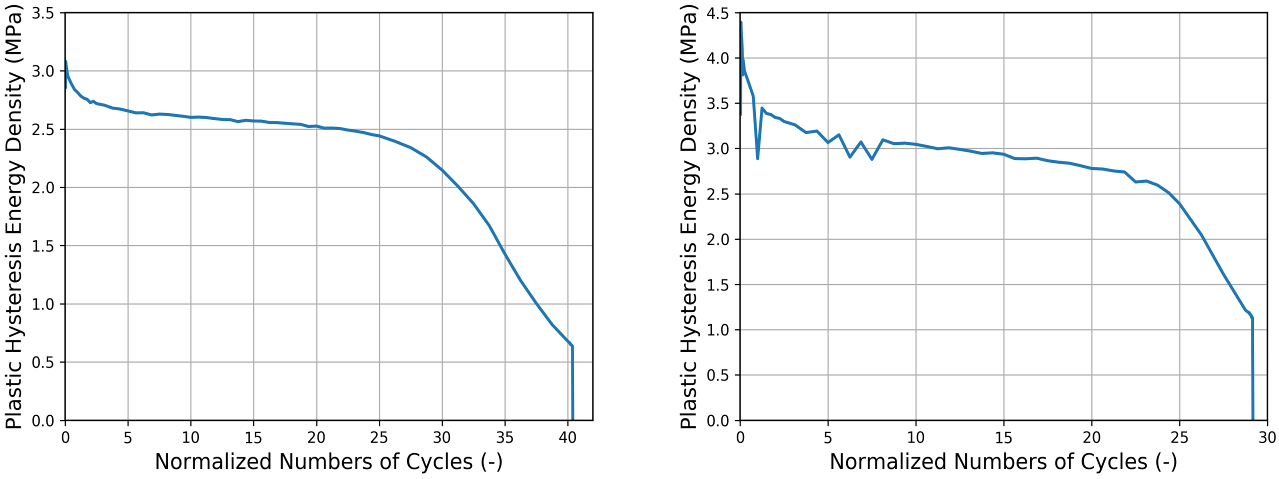

(c) BDD6d2

(d) BDD6dh10

Figure 36: Plastic hysteresis energy density of samples without and with hold-times.

higher temperature have a lower value of Y as compared to the samples at a lower temperature. Therefore, Y increases slightly with hold-time and decreases with increase in temperature.

4.3 Evaluation of Young's Modulus

Fig. 38 shows the comparison of the damage and Young's modulus of samples without and with hold-time at 300 °C and 600 °C. All of these samples have been deformed at a strain range $\Delta\varepsilon = 1\%$.

The damage has been measured by the technique described in Sec. 2.6.2. As shown in Fig. 38, Young's modulus decreases as the damage develops in the material in all four cases. Unlike the sample at the lower temperature, the samples at higher temperature show an initial decrease of Young's modulus and then normal slight decreasing behavior. According to Lemaitre [24], the initial decrease is due to the reversible movement of the dislocations and texture development. Therefore, it is not considered damage. Moreover, materials being deformed at elevated tem-

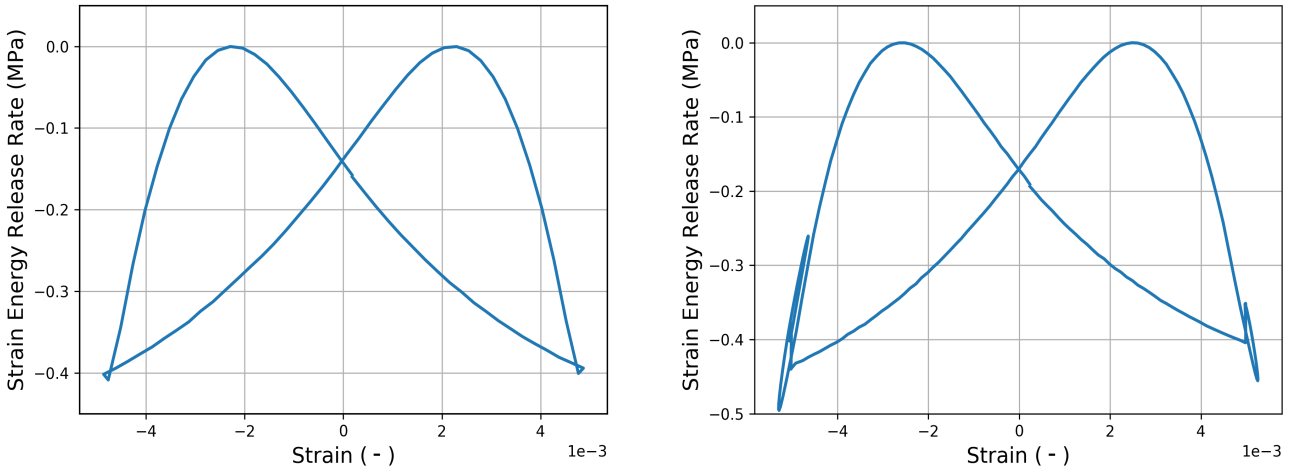

(a) BDD3d1 **(b)** BDD3dh1

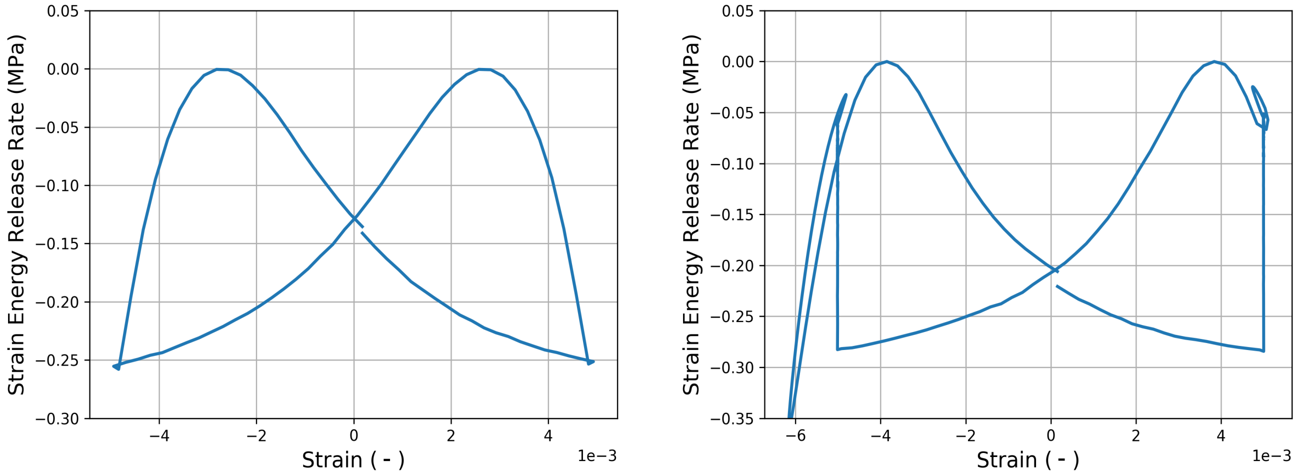

(c) BDD6d2 **(d)** BDD6dh10

Figure 37: Strain energy release rate of samples without and with hold-times.

peratures experience dynamic re-crystallization due to which they can experience an initial loss of strength [45]. Dynamic re-crystallization can also occur during creep. For BDD6dh10 (with hold-time), the initial drop of Young's modulus is larger than BDD6d2 (without hold-time). It could be possible due to dynamic re-crystallization during creep.

4.3.1 Crack Position

As mentioned in the previous section, Young's modulus decreases as the damage develops in subsequent cycles. However, some of the samples showed abnormal behavior that the Young's modulus increases and damage decreases over the number of cycles. Fig. 39 shows Young's modulus over number of cycles for BDD6dh12.

As shown in Fig. 39, the decrease in Young's modulus of the samples was observed. In the case of BDD6dh12 and BDD6dh14, Young's modulus started to increase from the beginning till the end of the cycles. For BDD625dh2 and BDD5dh1, there is a sudden increase of Young's

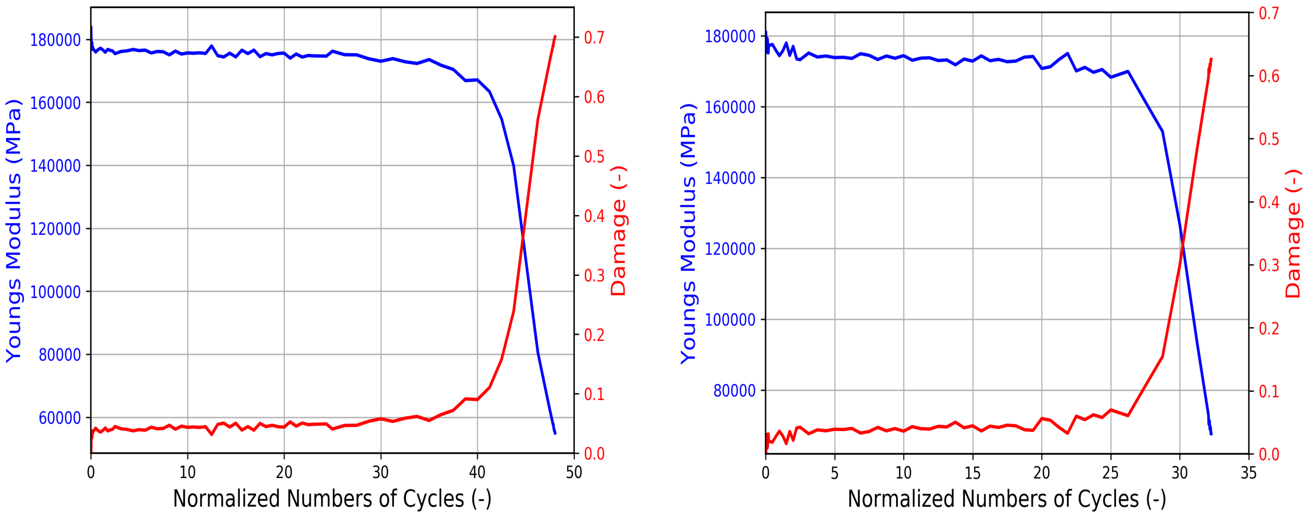

(a) BDD3d1 **(b)** BDD3dh1

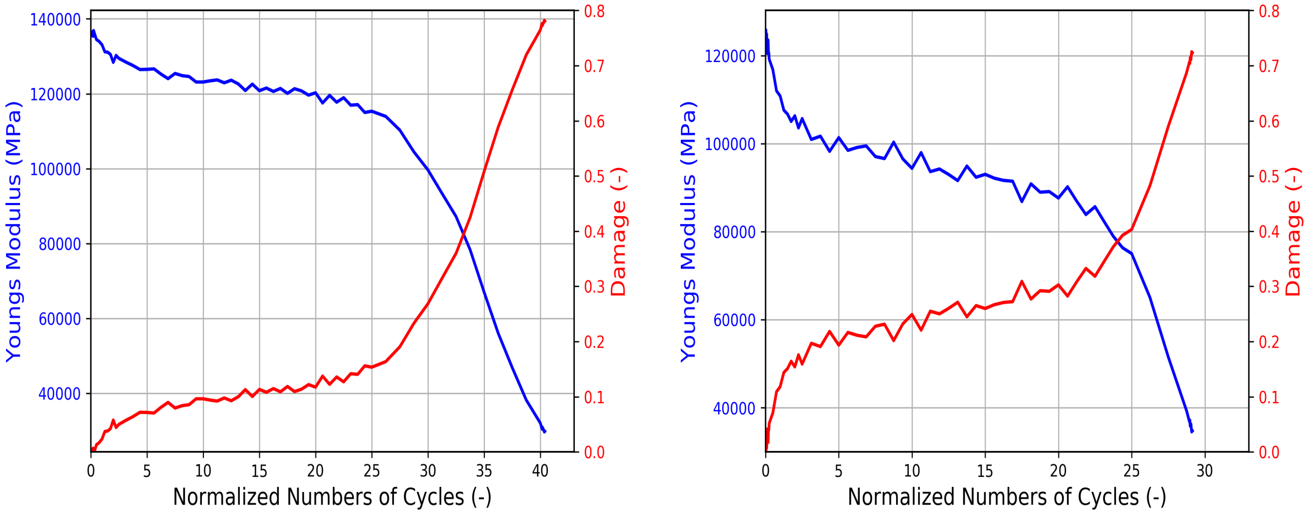

(c) BDD6d2 **(d)** BDD6dh10

Figure 38: Damage and Young's modulus of samples without and with hold-times.

modulus and a decrease of damage in the very beginning. When examined by the naked eye, it was revealed that the crack in these samples was initiated outside of the gauge marks of the extensometer or exactly on the gauge marks. Tables 8, 9, and 10 at the pages 48 and 49 list the crack position for samples. Figs. A1, A2, A3, and A4 show the crack position of the samples BDD6dh12, BDD6dh14, BDD625dh2, and BDD5dh1 respectively. For some samples, the cracks were found inside the gauge marks of the extensometer but shown some fluctuations of Young's modulus. One example, BDD5d6, is shown in Fig. 40.

It can be observed from Fig. 40 that Young's modulus after being regular for half of the cycles suddenly decreased sharply and increased at the end. The sudden decrease and then increase at the end could be due to some irregularity or defect on the microstructural level. It also could be possible due to some machine error, because when the raw data for BDD5d6 was examined, it was seen that the data recorded for the cycle (where Young's modulus increases suddenly) was wrong or missing.

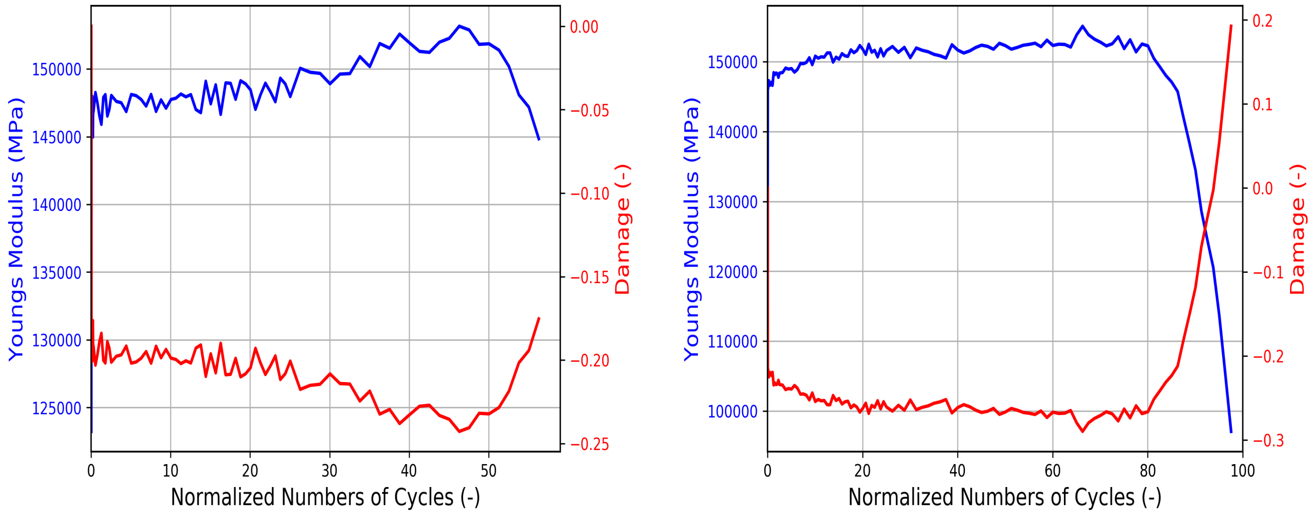

(a) BDD6dh12 **(b)** BDD6dh14

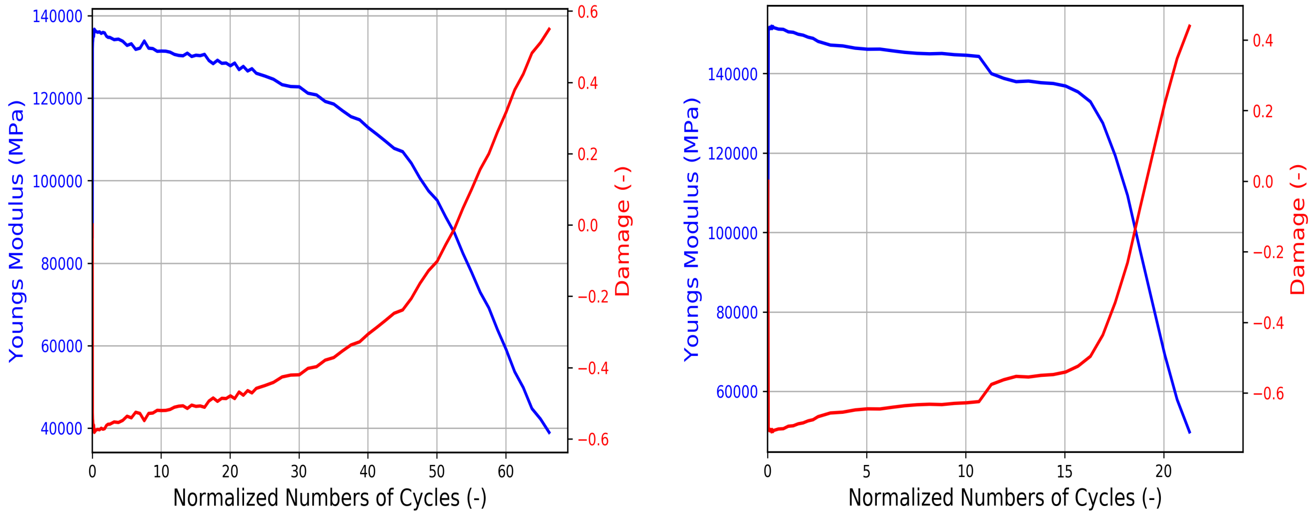

(c) BDD625dh2 **(d)** BDD5dh1

Figure 39: Irregular behavior of Young's modulus.

4.4 Optimization Results

Optimization of the material parameter S is carried out using the Nelder-Mead and the BFGS [15, 41] algorithm, and the results are shown in Tables A4, A5, and A6 respectively. Initial guess for the value of S is 2. Results, which are included in this report, are attained by using the Nelder-Mead algorithm. Initially, SciPy was used, but the computation took too long. To get rid of the long computation time, GSL was utilized, and only one parameter S was optimized. The other material parameter, s, was kept at a constant value of 2.1, taken as a reference from [13]. Tables A4, A5, and A6 also suggest that the S value in the employed model is almost same for experiments with hold-time and without hold-time at the same temperature. Therefore, the current model is only dependent on the p_D value, where S has no influence.

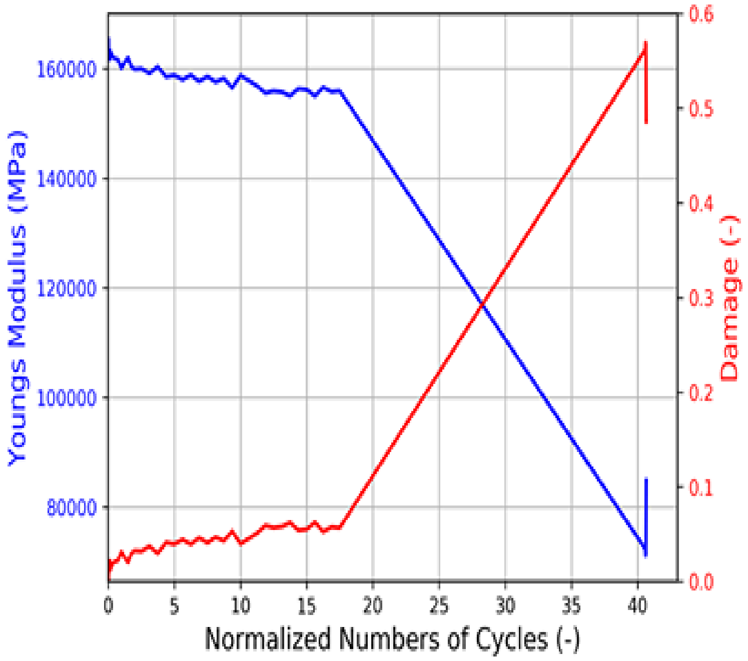

Figure 40: Irregular behavior of Young's Modulus of BDD5d6.

4.4.1 Temperature Dependence

Fig. 41 shows the optimized value of material parameter S, with $s = 2.1$ over different temperatures. It is clearly observable that S has a strong dependence on temperature with highest value of 2.85 at 300 °C and lowest value of 0.6 at 600 °C. S decreases with the increase in temperature.

Table 11 shows mean values of S and its standard deviation. For 300 °C, the standard deviation is not reasonable because of BDD3dh2. It has increasing Young's modulus behavior as mentioned in Sec. 4.3.1, but without its value, the standard deviation of 300 °C is below 20%. Other than that, overall standard deviation is less.

Table 11: Mean values and standard deviations of S over different temperatures.

Temperature (°C)	Mean of S (-)	Standard Deviation (%)
300	2.61	54
425	1.99	2.5
500	1.66	12
550	1.16	28
600	0.85	18
625	0.77	11

4.4.2 Strain Range Dependence

Fig. 42 shows the optimized value of material parameter S, with $s = 2.1$ over different strain ranges. It can be observed that there is no explicit dependence of S on the strain range. Samples at similar temperature, show approximately same value over different strain ranges and no

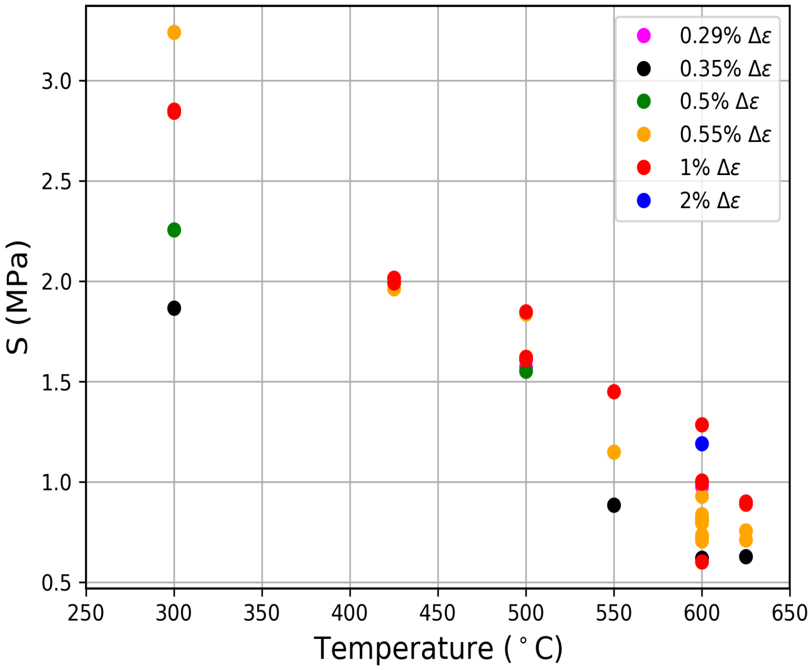

Figure 41: Optimized parameter S versus temperature.

increase or decrease in a trend is noticeable with increasing strain range. Again, for 300 °C, one value of S is high due to its increasing value of Young's modulus.

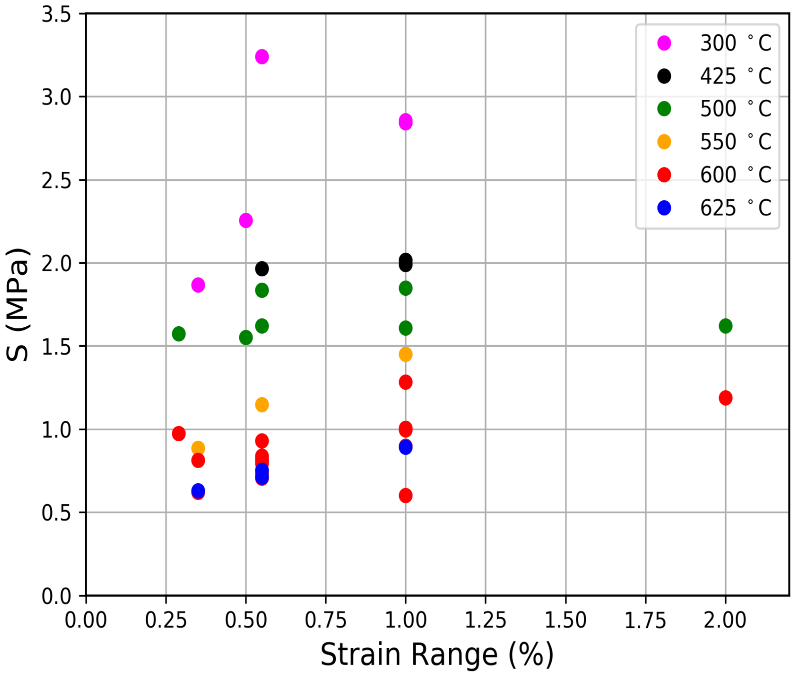

Figure 42: Optimized parameter S versus strain range.

4.4.3 Comparison of Measured and Computed Damage

Optimization of the material parameter S is carried out one more time when p_D is determined by inducing the condition $p > p_D$ in the damage evolution equation. Therefore, S is minimized again for the function $(D_{crit} - D_{comp})^2$.

After acquiring the parameters, the evolution equations are solved by using RK4 method [41]. Strains and stresses of all cycles are interpolated over time, and the accumulated plastic strain p and the damage D are computed over time. Fig. 43 shows p over time of BDD3d1 for first cycle, which increases continuously as the time increases.

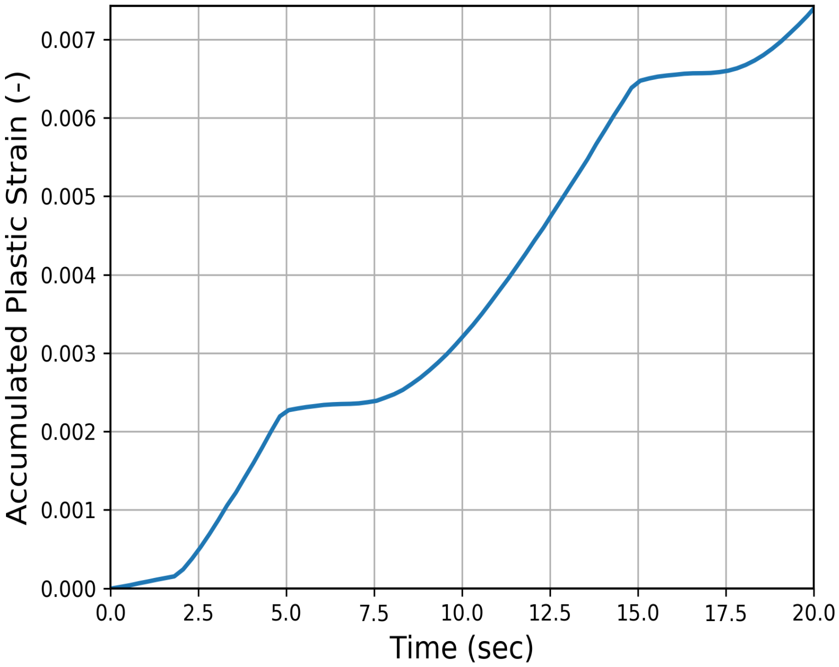

Figure 43: Accumulated plastic strain p over time of BDD3d1.

Fig. 44 shows the comparison of the computed damage of samples without and with hold-time at 300 °C and 600 °C. All of these samples have been deformed at a strain range $\Delta\varepsilon = 1\%$. Computed and measured damage shown in Fig. 44 is calculated till the $N_{A10\%}$.
As shown in Fig. 44, it can be seen that the applied damage model does not predict the final damage values accurately, but it is somewhat close to the measured damage. However, the relative error between the $N_{A5\%}$ is quite reasonable in comparison, which is shown in Table 12. $N_{A5\%}$ is calculated at D = 0.075.

The difference between the measured and predicted values is in the range of 4-10%. As discussed previously (Sec. 4.4), the current model provides approximately same values of S for experiment with and without hold-time for similar temperatures. At the same time, the predicted values of experiments with hold-time are as reasonable as for the experiments without hold-time. Therefore, it might be possible that the samples deformed with hold-time, contains minimal creep.

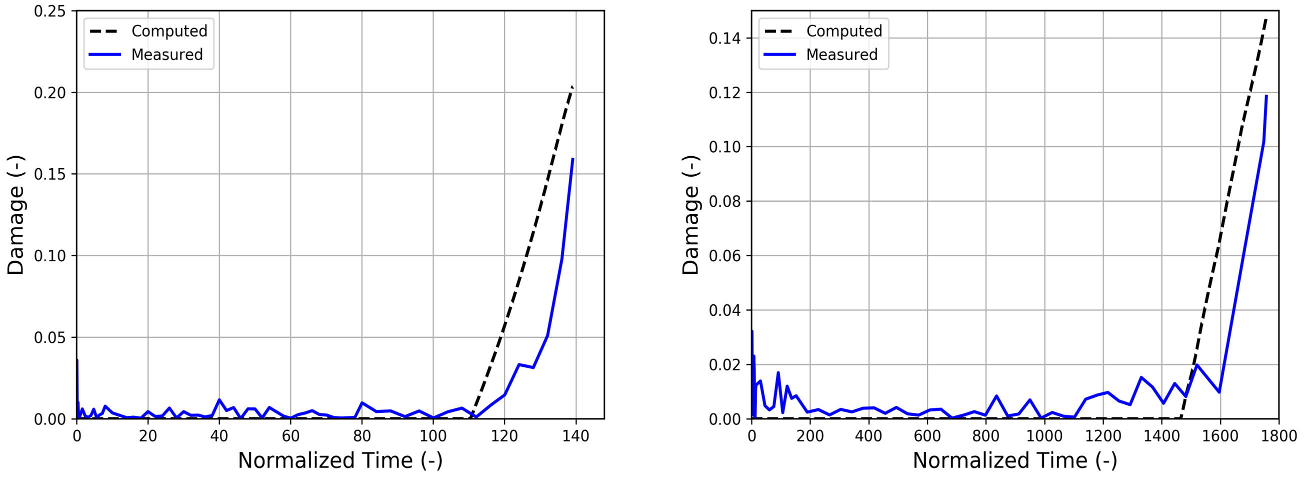

(a) BDD3d1 (S = 1.330 and p_D = 13.5). **(b)** BDD3dh1 (S = 1.382 and p_D = 11.5).

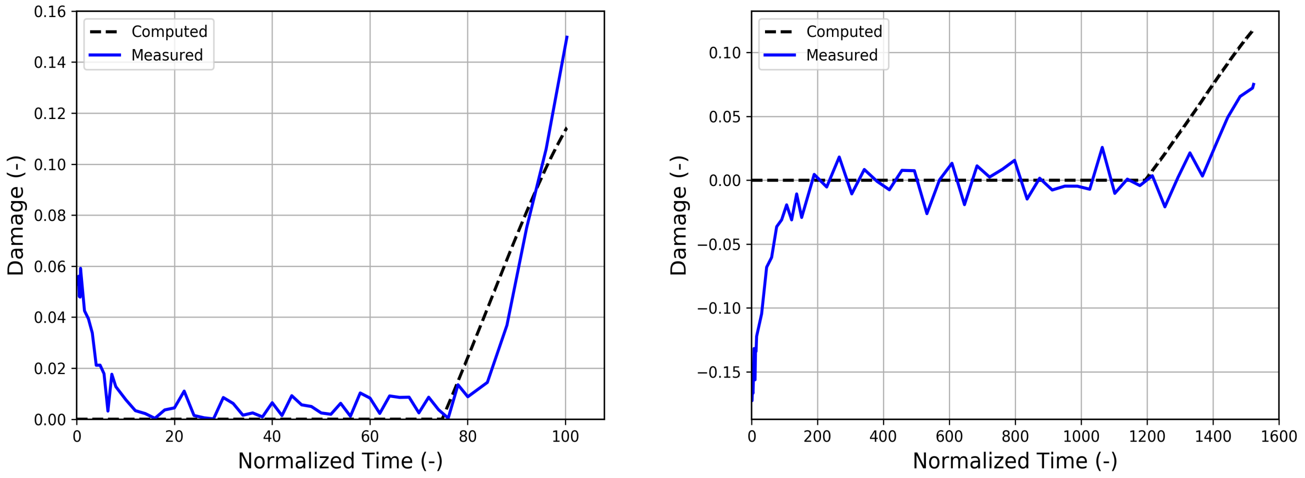

(c) BDD6d2 (S = 0.428 and p_D = 11). **(d)** BDD6dh10 (S = 0.399 and p_D = 13).

Figure 44: Computed and measured damage of samples without and with hold-times.

Table 12: Relative error between the measured and predicted values of $N_{A5\%}$.

Sample	Relative error (%)
BDD3d1	-9.17
BDD3dh1	-3.89
BDD6d2	-3.97
BDD6dh10	-4.06

To predict the lifetime of the components, S and p_D from experiments without hold-time are selected and used to compute the damage for experiments with hold-time. Therefore, $S = 1.211$ and $p_D = 12.5$ of BDD3d1 is used to evaluate the damage of BDD3dh1 and the $S = 0.428$ and $p_D = 11$ of BDD6d2 is used to evaluate the damage of BDD6dh10 respectively, as shown in Fig. 45.

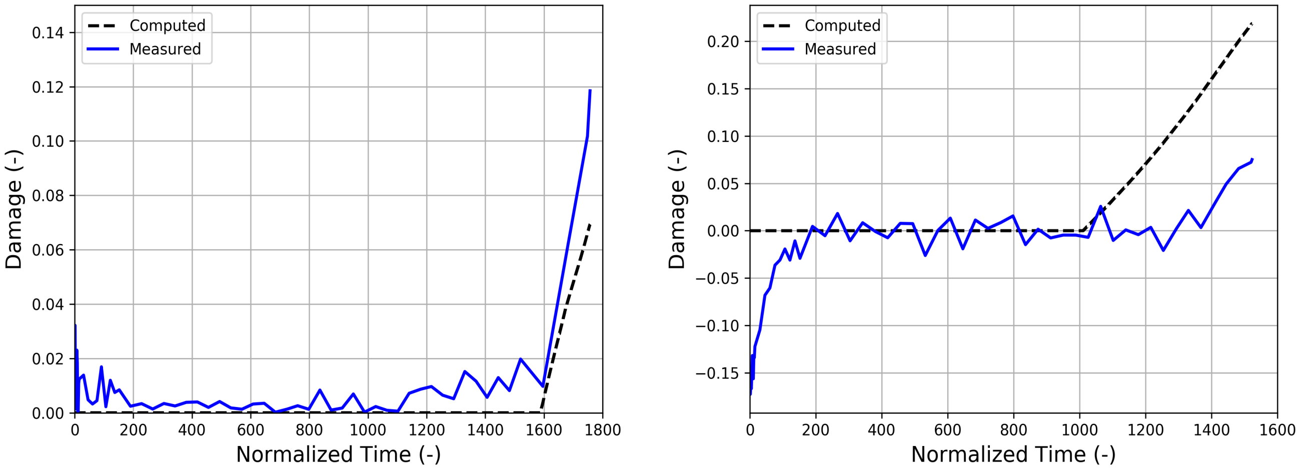

(a) BDD3dh1 ($S = 1.330$ and p_D = 13.5).

(b) BDD6dh10 ($S = 0.428$ and p_D = 11).

Figure 45: Lifetime prediction by using S value of experiment without hold-time.

It can be observed that for BDD3dh1, the predicted damage value is lower than the measured damage value, but for BDD6dh10 the damage value is larger than the measured damage. However, the predicted $N_{A5\%}$ for BDD3dh1 is quite reasonable than for BDD6dh10. It is clear from this result that the behavior of the predicted damage and the $N_{A5\%}$ value are totally dependept on p_D in this model. This also means that if the difference in real and used p_D is less, the prediction will be more accurate. Thus, if p_D is same so the predicted $N_{A5\%}$ will be almost similar as S is similar. Furthermore, it could be possible that the sample considered for damage evolution contains less amount of creep as the hold-time is just 3 minutes in tension and compression per cycle.

Data for one experiment with a service-type cycle, BDD6b1, were also received and the lifetime prediction for it is also performed using the S and p_D from BDD6d2. Resulting predicted value has an error of 15.9%. Table 13 shows the relative error between measured and predicted values.

Table 13: Relative error between the measured and predicted values of $N_{A5\%}$.

Sample	Relative error (%)
BDD3dh1	4.61
BDD6dh10	-16.66
BDD6b1	15.91

Fig. 46 shows the damage evolution of first cycle of BDD6d2 and BDD6dh10 without the condition of $p > p_D$.

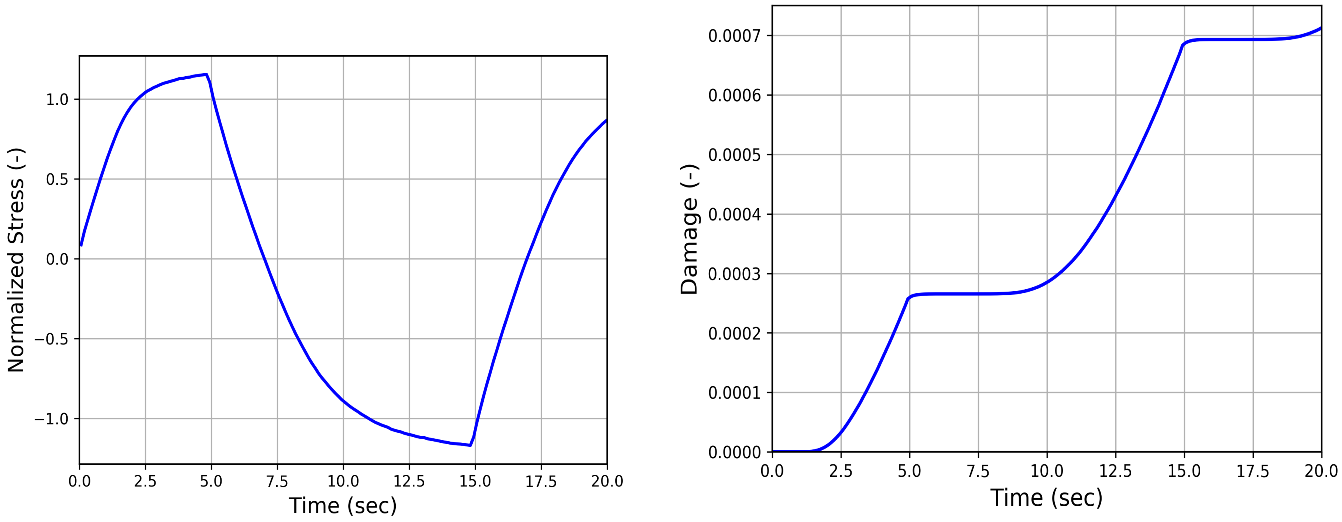

(a) BDD6d2 stress cycle.

(b) BDD6d2 damage evolution.

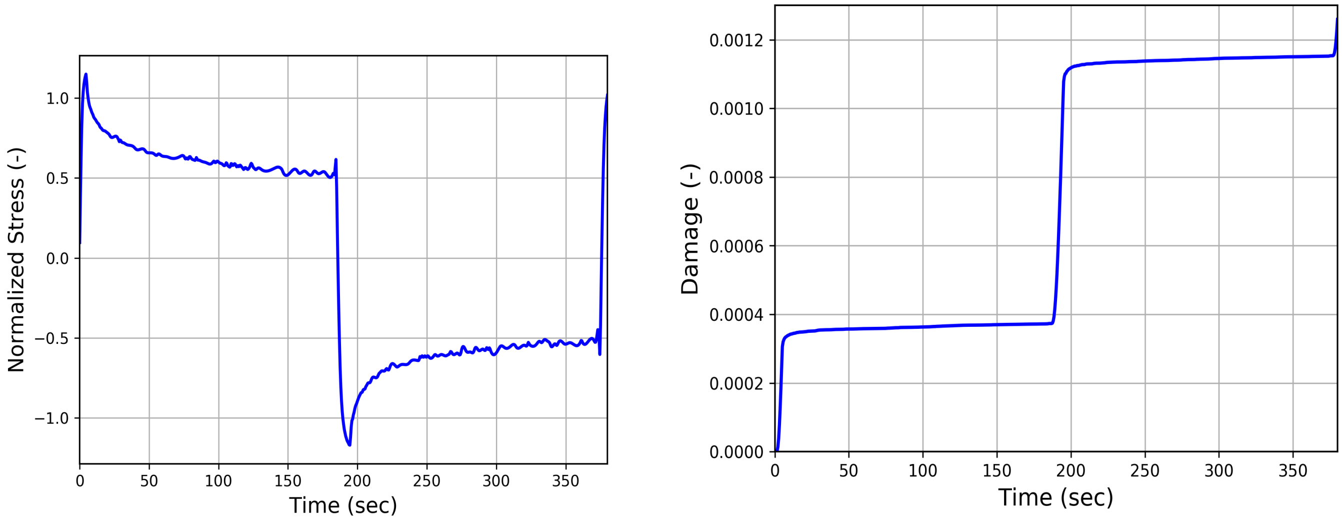

(c) BDD6dh10 stress cycle.

(d) BDD6dh10 damage evolution.

Figure 46: Stress over time and damage evolution of the first cycle.

For BDD6d2, it can be seen from Fig. 46a and 46b that the damage evolves smoothly with increasing stress cycle. Even-though when stress is decreasing, the rate of increase in damage is almost zero, but again starts to increase when the stress is maximum in compression.

For BDD6dh12, the situation is not the same. As shown in Fig. 46c and 46d, with increasing stress the damage increases exponentially and during the hold-time in tension, it increases very minimally. Afterwards, when stress increases in compression, then again a huge rise in damage can be seen. Again, during hold-time in compression, the damage increases slightly. Out of the two, BDD6dh10 acquired more damage than BDD6d2. Therefore, it can be concluded from the result that more damage is acquired in cycle with hold-time than without hold-time, which is the reason for early failure of BDD6dh10.

4.6 Computed Tomography Results

Computed tomography (CT) of two samples BDD625d2 and BDD6dh14 was performed. The CT scans were analyzed using the VGSTUDIO MAX analysis and visualization software to calculate the volume of defects and to measure damage by the use of its defect detection tool. The software is equipped with various algorithms, which were employed to detect defects. Figure 47 shows top view (planar-cut) of BDD625d2 sample .

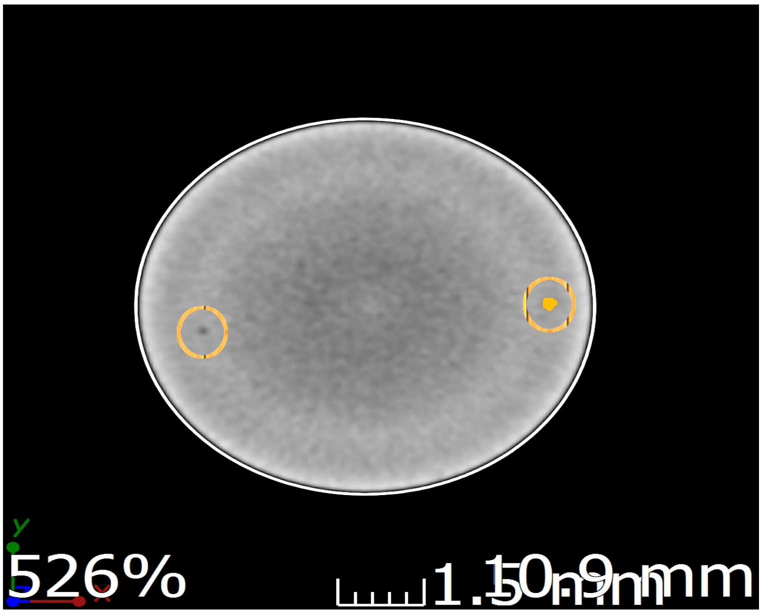

Figure 47: Top view of the planar cut of BDD625d2

It can be seen in Fig. 47 that using the defect analysis tool, the defect on the right side of the picture is detected, but at the same time a clear defect of the left side is undetected. The problem was seen in multiple pictures where the software was able to detect some defects but some not. Therefore, the approach is not suitable to calculate the volume of the defects.

Another approach, which could be beneficial, is to calculate the surface area and radius of defects by employing gray analysis. Gray analysis uses the concept of difference between the coloration of an area with its background. As cracks and voids are separation of the material, they are displayed dark and be easily differentiated. Our coworkers[4] are working on gray analysis which is shown in Fig. 48.

Fig. 48 shows gray analysis and its result. Both the defects in the scan below are detected effectively, and their size and radius are also shown. This is much better than the results obtained from defect detection tool of VGSTUDIO MAX. One limitation of this method is that cracks and voids are 3D, where volume is needed to be calculated and not the surface area. However, this technique could be extended to calculate volumes of defects.

4.7 Microstructural Evaluation

Microstructural analysis has been performed for the samples employed with service-type cycles. No microsctructures were available for BDD samples. Therefore, BDD6b1 with a service-type

---

[4] Institute of Materials Technology (MPA/IfW), Technische Universität Darmstadt

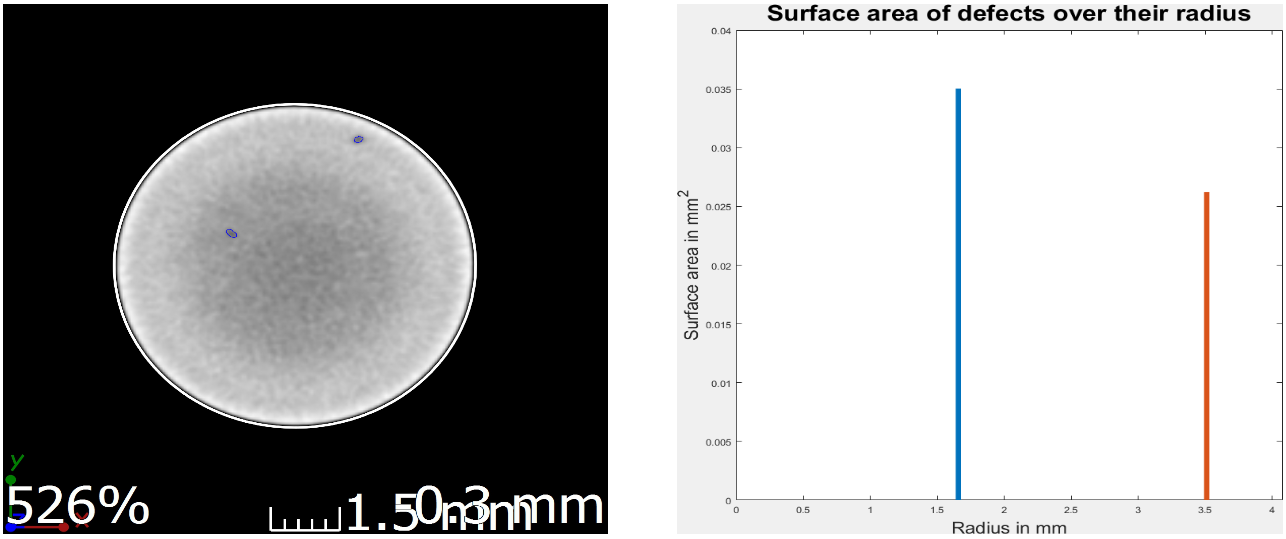

(a) Defect detection

(b) Surface area over radius of defects

Figure 48: Gray analysis of CT scan.

cycle at a strain range of 1% is used thereafter for analysis. Fig. 49 show the CT scan of the area where the cracks lie.

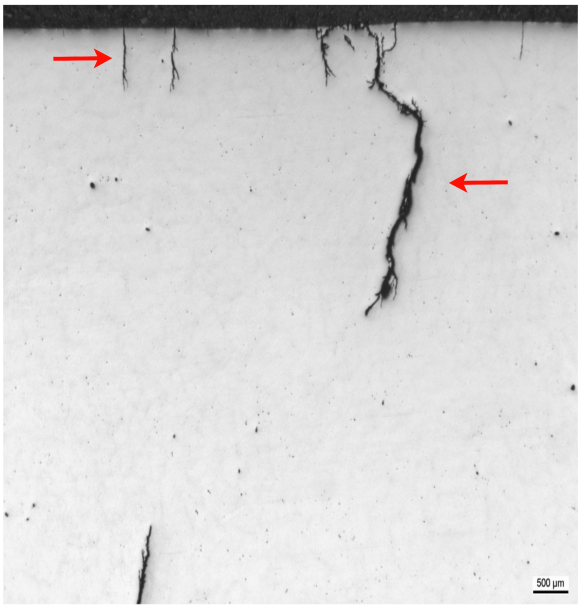

Figure 49: CT scan of BDD6b1 zoomed at the area where cracks lie.

As shown in Fig. 49, the two cracks on the top left-side look like fatigue cracks, as they grow transverse to the applied loading in a transgranular way [46]. Also, slight branches can be seen. On the left-hand side, a large crack can be seen which looks like to have been formed by the mechanism of creep involved with fatigue. As BDD6b1 is deformed at a service-type cycle, there exists high chance of time-dependent deformation. The presence of creep can change the path of a crack generated on the surface to be intergranular [46]. Also, branching of the crack can be seen at the tip. Thus, it can be understood as a creep-fatigue crack. It can also be compared to Fig. 8, where different modes of damage are shown, where creep initiates at grain boundaries and the fatigue cracks follows their direction. Microstructure of the large crack is shown in Fig. 50.

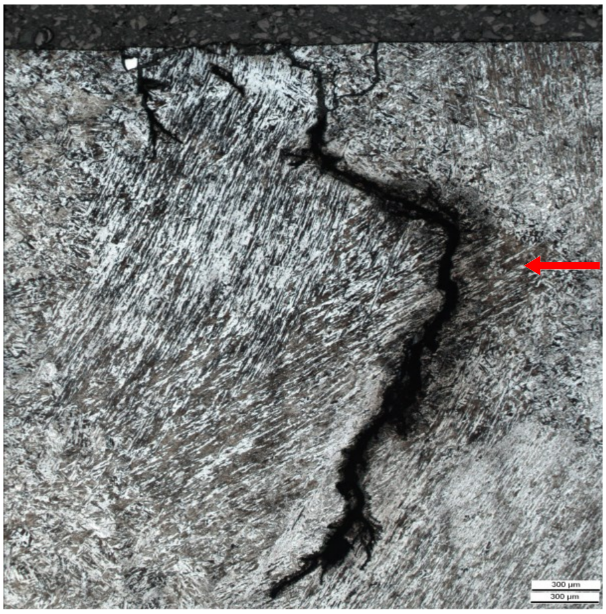

Figure 50: Microstructure of the longest crack in the sample.

Plastic deformation at high temperatures imposes the risk of oxidation at the material surface or even at the grains [47].The dark area along the crack shown by an arrow on the right side in Fig. 50 possibly indicates the oxidation of the grain boundaries, which is also a time-dependent phenomenon.

5 Conclusion

In conclusion, experimental data of strain-controlled LCF experiments without and with hold-time in tension and compression performed on high-chromium steels were received. A phenomenological damage definition is selected under the concept of CDM, which defines a damage threshold in terms of accumulated plastic strain for damage initiation. Furthermore, RK4 method [41] is employed for solving the damage evolution equations. Material parameter S of the damage evolution equation is minimized using the Nelder-Mead [14] and the BFGS algorithm [15]. Moreover, multiaxial fatigue damage evolution model [13] is utilized for evaluating damage, which is based on the strain energy equivalence hypothesis. Also, lifetime prediction is performed using the material parameter from experiments without hold-time for experiments with hold-time.

A method to determine critical value for damage initiation is shown, where D_{crit} for BDD samples is found out to be 0.075. It is also shown that D_{crit} is independent of temperature and stress-triaxiality. For BAP samples, the data is not enough to draw statistical conclusion. Moreover, a method to obtain true damage from measured damage (which according to literature [18] is not damage) is shown. Damage threshold p_D for damage initiation is calculated for every experiment. It is shown that p_D is dependent on strain range $\Delta\varepsilon$ and decreases with increasing $\Delta\varepsilon$. Also, p_D has no dependence on temperature. Furthermore, irregular behavior of Young's modulus is discussed regarding the crack position. It is shown that irregular behavior of Young's modulus is due to the initiation of crack outside the gauge marks of the extensometer.

Optimization of material parameter S is performed and it is shown that S depends on temperature where it decreases with increasing temperature. Also, it is independent of $\Delta\varepsilon$ and shows approximately similar values. Furthermore, lifetime prediction is performed using the the constants from experiments without hold-time for experiments with hold-time at 300 °C and 600 °C. The resulting predicted values are reasonable with an error as high as 16.6%, even for experiments with a service-type cycle, and it is plausible to say that p_D is the main parameter which controls the predicted value as damage is directly dependent to it.

Therefore, the main drawback of the used model [13] is the dependence of damage on p_D which is not satisfied according to our desired damage definition (Sec. 2.1). For coping up this dependence, a damage model based on total energy equivalence hypothesis as proposed by Saanouni et al. [30] should be employed as to avoid any dependence on the internal variable. Grammenoudis et al. [48, 49] have proposed damage models for isotropic and anisotropic material response employing the hypothesis of energy equivalence which can be utilized in future for the damage evolution.

Bibliography

[1] S. Murakami. *Continuum damage mechanics: a continuum mechanics approach to the analysis of damage and fracture*. Vol. 185. Springer Science & Business Media, 2012.

[2] Run-Zi Wang et al. *A modified strain energy density exhaustion model for creep–fatigue life prediction*. In: *International Journal of Fatigue* 90 (2016), pp. 12–22.

[3] W. M. Payten, D. W. Dean, and K. U. Snowden. *A strain energy density method for the prediction of creep–fatigue damage in high temperature components*. In: *Materials Science and Engineering: A* 527.7 (2010), pp. 1920–1925.

[4] R.P. Skelton. *The energy density exhaustion method for assessing the creep-fatigue lives of specimens and components*. In: *Materials at High Temperatures* 30.3 (2013), pp. 183–201.

[5] R.P. Skelton and D. Gandy. *Creep–fatigue damage accumulation and interaction diagram based on metallographic interpretation of mechanisms*. In: *Materials at High Temperatures* 25.1 (2008), pp. 27–54.

[6] Y. Takahashi, B. Dogan, and D. Gandy. *Systematic evaluation of creep-fatigue life prediction methods for various alloys*. In: *Journal of Pressure Vessel Technology* 135.6 (2013), p. 061204.

[7] M. A. Miner. *Cumulative damage in fatigue*. In: *J. appl. Mech.* 12.3 (1945), A159–A164.

[8] S. Murakami. *Notion of continuum damage mechanics and its application to anisotropic creep damage theory*. In: *ASME, Transactions, Journal of Engineering Materials and Technology* 105 (1983), pp. 99–105.

[9] D. K. Krajcinovic. *Introduction to continuum damage mechanics*. 1986. ISBN: 9024733197.

[10] J. L. Chaboche. *Anisotropic creep damage in the framework of continuum damage mechanics*. In: *Nuclear engineering and design* 79.3 (1984), pp. 309–319.

[11] L. M. Kachanov and D. Krajcinovic. *Introduction to continuum damage mechanics*. In: *Journal of Applied Mechanics* 54 (1987), p. 481.

[12] J. Lemaitre. *A continuous damage mechanics model for ductile fracture*. In: *Transactions of the ASME. Journal of Engineering Materials and Technology* 107.1 (1985), pp. 83–89.

[13] J. P. Sermage, J. Lemaitre, and R. Desmorat. *Multiaxial creep fatigue under anisothermal conditions*. In: (2001), pp. 125–130.

[14] J. A. Nelder and R. Mead. *A simplex method for function minimization*. In: *The computer journal* 7.4 (1965), pp. 308–313.

[15] C. Zhu et al. *Algorithm 778: L-BFGS-B: Fortran subroutines for large-scale bound-constrained optimization*. In: *ACM Transactions on Mathematical Software (TOMS)* 23.4 (1997), pp. 550–560.

[16] A Fatemi and L Yang. *Cumulative Fatigue Damage and Life Prediction Theories: A Survey of the State of the Art for Homogeneous Materials International Journal of Fatigue 20 (1998) 1*. In: *CrossRef| Web of Science® Times Cited* 359 ().

[17] B. Banerje (Wikipedia). *Fracture*. 2017. URL: `https://en.wikipedia.org/wiki/Fracture#/media/File:Ductile_fracture_upd.png`.

[18] J. Lemaitre. *A course on damage mechanics*. Springer Science & Business Media, 2012.

[19] L. K. Bhagi, P. Gupta, and V. Rastogi. *Fractographic investigations of the failure of L-1 low pressure steam turbine blade*. In: *case studies in Engineering Failure Analysis* 1.2 (2013), pp. 72–78.

[20] R. G. Budynas, J. Keith, et al. *Shigley's mechanical engineering design*. Vol. 8. McGraw-Hill New York, 2008.

[21] A. Saha, J. Jung, and G.B. Olson. *Prototype evaluation of transformation toughened blast resistant naval hull steels: Part II*. In: *Journal of Computer-Aided Materials Design* 14.2 (2007), pp. 201–233.

[22] J Dufailly and J Lemaitre. *Modeling very low cycle fatigue*. In: *International Journal of damage mechanics* 4.2 (1995), pp. 153–170.

[23] R. Hill. *Elastic properties of reinforced solids: some theoretical principles*. In: *Journal of the Mechanics and Physics of Solids* 11.5 (1963), pp. 357–372.

[24] J. Lemaitre and R. Desmorat. *Engineering damage mechanics: ductile, creep, fatigue and brittle failures*. Springer Science & Business Media, 2005.

[25] W. Zhang and Y. Cai. *Continuum Damage Mechanics And Numerical Applications*. In: (2010).

[26] A. Cauvin and R. B. Testa. *Damage mechanics: basic variables in continuum theories*. In: *International Journal of Solids and Structures* 36.5 (1999), pp. 747–761.

[27] L. M. Kachanov. *Rupture time under creep conditions*. In: *International journal of fracture* 97.1-4 (1958), pp. 11–18.

[28] Yu N. Rabotnov. *Creep rupture, 12 th Int. Congress of Applied mechanics*. In: (1968).

[29] J.P. Cordebois and F. Sidoroff. *Damage induced elastic anisotropy*. In: (1982), pp. 761–774.

[30] K. Saanouni, C. H. Forster, and F. Ben Hatira. *On the anelastic flow with damage*. In: *International Journal of Damage Mechanics* 3.2 (1994), pp. 140–169.

[31] F. P. E. Dunne and D. R. Hayhurst. *Continuum damage based constitutive equations for copper under high temperature creep and cyclic plasticity*. In: 437.1901 (1992), pp. 545–566.

[32] G. Rousselier. *Ductile fracture models and their potential in local approach of fracture*. In: *Nuclear engineering and design* 105.1 (1987), pp. 97–111.

[33] J. Kestin and J. R. Rice. *Paradoxes in the application of thermodynamics to strained solids*. In: *Critical Review on Thermodynamics. Mono Book Corp., Baltimore, USA* 275 (1970), pp. 275–298.

[34] L. E. Malvern. *Introduction to the mechanics of a continuous medium*. Englewood Cliffs, N.J. : Prentice-Hall, 1969. ISBN: 0134876032.

[35] K. G. Samuel. *Limitations of Hollomon and Ludwigson stress–strain relations in assessing the strain hardening parameters*. In: *Journal of Physics D: Applied Physics* 39.1 (2005), p. 203.

[36] J. R. Rice. *Inelastic constitutive relations for solids: an internal-variable theory and its application to metal plasticity*. In: *Journal of the Mechanics and Physics of Solids* 19.6 (1971), pp. 433–455.

[37] J. N. Reddy. *An introduction to continuum mechanics*. Cambridge university press, 2013.

[38] J. L. Chaboche. *Continuum damage mechanics: Part II—Damage growth, crack initiation, and crack growth*. In: *Journal of applied mechanics* 55.1 (1988), pp. 65–72.

[39] Radim Znajda. *Betriebsähnliches Langzeitdehnverhalten wichtiger Stahlsorten im Hochtemperturbereich*. PhD thesis. Technische Universität Darmstadt, 2007.

[40] R. Kong et al. *Zur Schädigungsentwicklung mehrachsig und anisotherm hochbeanspruchter dickwandiger Gehäuse moderner thermischer Maschinen und Anlagen*. Abchlussbericht des Forschungsprojektes. Technische Universität Darmstadt, 2015.

[41] P. J. Prince and J. R. Dormand. *High order embedded Runge-Kutta formulae*. In: *Journal of Computational and Applied Mathematics* 7.1 (1981), pp. 67–75.

[42] Jun-Shan Zhang. *High temperature deformation and fracture of materials*. Elsevier, 2010.

[43] J. Polák. *Cyclic plasticity and low cycle fatigue life of metals*. Materials science monographs. Elsevier, 1991.

[44] KM Golos. *A total strain energy density model of metal fatigue*. In: *Strength of materials* 27.1-2 (1995), pp. 32–41.

[45] Günter Gottstein. *Physical foundations of materials science*. Springer Science & Business Media, 2013.

[46] R. Hales. *A qauntitative metallographic assessment of structural degradation of type 316 stainless steel during creep-fatigue*. In: *Fatigue & Fracture of Engineering Materials & Structures* 3.4 (1980), pp. 339–356.

[47] Michael Auinger et al. *Grain boundary oxidation in iron-based alloys, investigated by 18O enriched water vapour–The effect of mixed oxides in binary and ternary Fe–{Al, Cr, Mn, Si} systems*. In: *Corrosion Science* 96 (2015), pp. 133–143.

[48] P Grammenoudis, D Reckwerth, and Ch Tsakmakis. *Continuum damage models based on energy equivalence: part I—isotropic material response*. In: *International Journal of Damage Mechanics* 18.1 (2009), pp. 31–63.

[49] P Grammenoudis, D Reckwerth, and Ch Tsakmakis. *Continuum damage models based on energy equivalence: part II—anisotropic material response*. In: *International Journal of Damage Mechanics* 18.1 (2009), pp. 65–91.

Appendix: Tables

Table A1: Damage threshold values of BDD samples without hold-time.

Sample	p_D (-)	$\Delta\varepsilon$ (%)	Temperature (°C)
BDD3d1	13.5	1	300
BDD3d2	15	0.5	300
BDD3d3	22	0.35	300
BDD425d1	6	1	425
BDD425d2	13	0.55	425
BDD425d4	7	1	425
BDD5d1	3	2	500
BDD5d2	9	1	500
BDD5d3	12	0.5	500
BDD5d4	12	0.35	500
BDD5d5	48	0.29	500
BDD5d6	6	1	500
BDD55d2	11	0.55	550
BDD55d3	15	0.35	550
BDD55d4	11	1	550
BDD6d1	8	2	600
BDD6d2	11	1	600
BDD6d3	11	0.55	600
BDD6d4	25	0.35	600
BDD6d5	60	0.29	600
BDD6d6	15	0.55	600
BDD6d7	12.5	0.55	600
BDD6d10	10	0.55	600
BDD6d11	13	0.55	600
BDD6d12	11	0.55	600
BDD6d22	9	1	600
BDD625d1	13	1	625
BDD625d2	15	0.55	625
BDD625d3	20	0.35	625
BDD625d4	14	1	625
BDD625d5	15	0.55	625

Table A2: Damage threshold values of BDD samples with hold-time.

Sample	p_D (-)	$\Delta\varepsilon$ (%)	Temperature (°C)
BDD3dh1	11.5	1	300
BDD3dh2	22	0.55	300
BDD5dh1	7	1	500
BDD5dh4	13	0.55	500
BDD5dh5	115	0.35	500
BDD5dh14	20	0.55	500
BDD6dh1	12	0.35	600
BDD625dh2	12	0.55	625
BDD6dh3	10	0.55	600
BDD6dh4	15	0.55	600
BDD6dh7	21	0.55	600
BDD6dh10	13	1	600
BDD6dh11	10	1	600
BDD6dh12	28	0.35	600
BDD6dh13	6	0.55	600
BDD6dh14	44	0.55	600
BDD6dh20	10	1	600

Table A3: Damage threshold values of BAP samples without hold-time.

Sample	p_D (-)	$\Delta\varepsilon$ (%)	Temperature (°C)
BAP5d1	8	1	500
BAP5d2	12	0.67	500
BAP5d3	13	0.5	500
BAP5d4	80	0.41	500
BAP525d2	12	0.53	525
BAP525d3	20	0.47	525
BAP525d4	40	0.4	525

Table A4: Optimization values of S for BDD samples without hold-time.

Sample	s (-)	S (-)	Iterations (-)	$\Delta\varepsilon$ (%)	T (°C)
BDD3d1	2.1	2.842674255	19	1	300
BDD3d2	2.1	2.256248474	20	0.5	300
BDD3d3	2.1	1.866687775	20	0.35	300
BDD425d1	2.1	1.991920471	20	1	425
BDD425d2	2.1	1.964761734	20	0.55	425
BDD425d4	2.1	2.01644516	20	1	425
BDD5d1	2.1	1.620910645	21	2	500
BDD5d2	2.1	1.848520279	21	1	500
BDD5d3	2.1	1.550920486	21	0.5	500
BDD5d4	2.1	1.121984482	21	0.35	500
BDD5d5	2.1	1.573701859	21	0.29	500
BDD5d6	2.1	1.608503342	21	1	500
BDD55d2	2.1	1.14834404	21	0.55	550
BDD55d3	2.1	0.8852519989	21	0.35	550
BDD55d4	2.1	1.450567245	21	1	550
BDD6d1	2.1	1.189390182	21	2	600
BDD6d2	2.1	0.9947891235	21	1	600
BDD6d3	2.1	0.7121143341	23	0.55	600
BDD6d4	2.1	0.8135757446	22	0.35	600
BDD6d5	2.1	0.9749450684	21	0.29	600
BDD6d6	2.1	0.9290122986	22	0.55	600
BDD6d7	2.1	0.8204860687	22	0.55	600
BDD6d10	2.1	0.7252540588	22	0.55	600
BDD6d11	2.1	0.7341117859	22	0.55	600
BDD6d12	2.1	0.7048568726	22	0.55	600
BDD6d22	2.1	0.6005783081	22	1	600
BDD625d1	2.1	0.89868927	22	1	625
BDD625d2	2.1	0.710603714	22	0.55	625
BDD625d3	2.1	0.628490448	22	0.35	625
BDD625d4	2.1	0.8905887604	22	1	625
BDD625d5	2.1	0.7544403076	22	0.55	625

Table A5: Optimization values of S for BDD samples with hold-time.

Sample	s	S	Iterations	Strain range	Temperature
BDD3dh1	2.1	2.855342865	20	1	300
BDD3dh2	2.1	3.241504669	19	0.55	300
BDD5dh1	2.1	5.969799042	26	1	500
BDD5dh4	2.1	1.621753693	21	0.55	500
BDD5dh5	2.1	11.86532974	30	0.35	500
BDD5dh14	2.1	1.837278366	21	0.55	500
BDD6dh1	2.1	0.6192741394	22	0.35	600
BDD6dh3	2.1	0.7953472137	22	0.55	600
BDD6dh4	2.1	0.8131904602	22	0.55	600
BDD6dh5	2.1	0.0843849182	26	1	600
BDD6dh7	2.1	0.8378105164	22	0.55	600
BDD6dh10	2.1	1.005462646	21	1	600
BDD6dh11	2.1	5.830366135	26	1	600
BDD6dh13	2.1	4.49552536	27	0.55	600
BDD6dh14	2.1	4.810113907	25	0.55	600
BDD6dh20	2.1	1.284843445	22	1	600
BDD625dh2	2.1	8.239284515	28	0.55	625

Table A6: Optimization values of S for BAP samples without hold-time.

Sample	s	S	Iterations	strainRange	Temperature
BAP525d1	2.1	0.0718841553	25	1	500
BAP525d2	2.1	1.626523972	21	0.67	500
BAP525d3	2.1	2.037824631	20	0.5	500
BAP525d4	2.1	2.377592087	19	0.41	500
BAP55d1	2.1	1.511554718	21	0.67	550
BAP55d4	2.1	1.52466774	21	0.4	550
BAP5d1	2.1	2.394842148	19	0.73	525
BAP5d2	2.1	2.127727509	20	0.53	525
BAP5d3	2.1	2.043897629	20	0.47	525
BAP5d4	2.1	3.456260681	19	0.4	525

Appendix: Figures

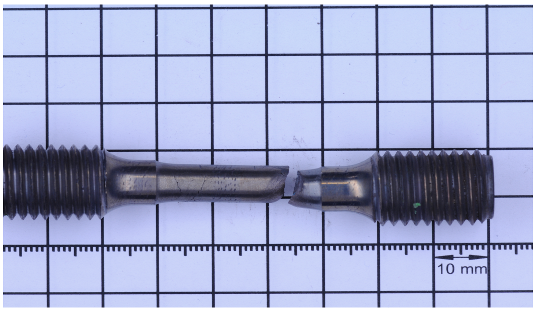

Figure A1: Crack position of BDD6dh12.

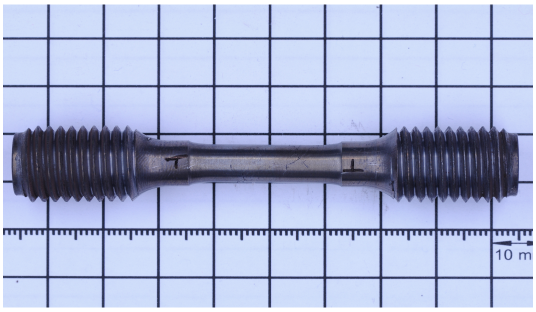

(a) Front.

(b) Back.

Figure A2: Gauge marks and crack position of BDD6dh14.

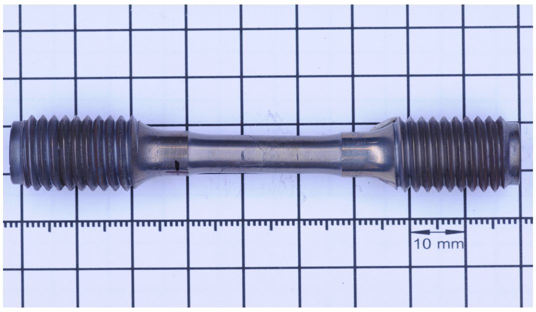

(a) Front.

(b) Back.

Figure A3: Gauge marks and crack position of BDD625dh2.

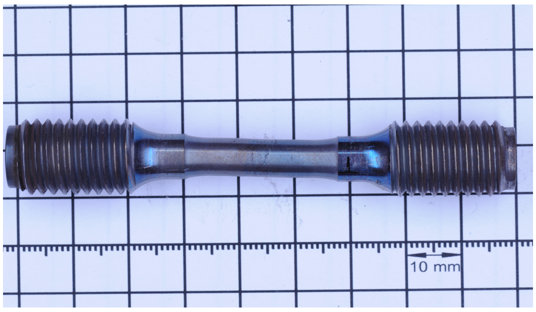

(a) Front.

(b) Back.

Figure A4: Gauge marks and crack position of BDD5dh1.